Persistent oscillations in the Aplysia bag cell network

by

Keegan Keplinger

A thesis
presented to the University of Waterloo
in fulfillment of the
thesis requirement for the degree of
Doctor of Philosophy
in
Applied Mathematics

Waterloo, Ontario, Canada, 2017

Examining Committee Membership

The following served on the Examining Committee for this thesis. The decision of the Examining Committee is by majority vote.

External Examiner

ROBERT J. BUTERA JR.	Associate Professor and Associate Dean for Research and Innovation, College of Engineering, Georgia Tech

Supervisor

SUE ANN CAMPBELL	Professor of Applied Mathematics, University of Waterloo

Internal Members

MAREK STASTNA	Professor of Applied Mathematics, University of Waterloo
BRIAN INGALLS	Associate Professor and Associate Dean of Applied Mathematics, University of Waterloo

Internal-external Member

DAVID SPAFFORD	Associate Professor of Biology, University of Waterloo

Other Member

NEIL MAGOSKI	Professor of Biomedical and Molecular Science, Queens University

I hereby declare that I am the sole author of this thesis. This is a true copy of the thesis, including any required final revisions, as accepted by my examiners.

I understand that my thesis may be made electronically available to the public.

Abstract

Persistence is a phenomena by which a resting neuron enters a state of persistent behavior following a brief stimulus. Persistent neural systems can exhibit long-term responses that remain after the stimulus is removed, switching from excitable, steady-state dynamics to a period of tonic spiking or bursting. In *Aplysia*, such behavior, known as the afterdischarge, is exhibited by the bag cell neuron and regulated by second messenger calcium dynamics. In this thesis, we construct a model for the electrical activity of the *Aplysia* bag cell neuron is constructed based on experimental data. The model includes many features of the bag cell, including use-dependence, non-selective cation channels, a persistent calcium current, and the afterdischarge. Each of these features contributes to the onset of afterdischarge. Several methods are used to fit experimental data and construct the model, including hand tuning, parameter forcing, genetic algorithms for optimization, and continuation analysis. These methods help to address common modeling issues such as degeneracy and sensitivity.

Use-dependence in the calcium channels of *Aplysia* is thought to depend on calcium. The model developed in this thesis verifies calcium as a viable driver for use-dependence. The literature often emphasizes two potassium channels in the context of bag cell afterdischarge, but we show that afterdischarge behavior is produced with only a single potassium channel in simulations. Experimental evidence suggests that nonselective cation channels are a primary driver of afterdischarge behavior. In the model developed here, the nonselective current is required for *in silica* afterdischarge to take place. Continuation analysis is used to determine and tune the location and stability of fixed points in the model.

For exploratory analysis, an electrically-coupled network model is constructed to simulate the observed dynamics in bag cell clusters *in vivo*. A simple two-neuron network reproduces some experimental results. Larger networks are considered. Little is known about the topology of Aplysia bag cell cluster. The final chapter of this thesis explores different topologies in a 100-neuron network, including a ring topology, a cluster ring topology, and a randomly-connected scatter network, exploring how the coupling constant, topology, and size of the network affect the ability of the network to synchronize.

Acknowledgements

Thanks be to Cthulhu. Ph'nglui mglw'nafh Cthulhu R'lyeh wgah'nagl fhtagn. And my wife, Aimee Fogler, without whom this path may have never been taken. Much thanks to my father, Mark Keplinger, and my uncle, Mitch Keplinger, for their support throughout my education.

Thanks to Neil Magoski and his team, whose elaborate experimental coverage of the *Aplysia* bag cell neuron sourced much of this theoretical work. Thanks to my advisor, Sue Ann Campbell for mathematical guidance and helping bridge the knowledge gap between experiment and theory. Thanks to my former advisor, Renate Wackerbauer, for showing me the joys of nonlinear dynamics. Thanks to my friend and informal advisor, Micheal Harris, for independent collaborations that allowed me to develop autonomy, and thanks to Marek Stastna for reminding me to maintain that autonomy and to start simple in modeling. Thanks to David Spafford for a broad perspective of the state of experimental neuroscience, and to Brian Ingalls for his guidance in mass action kinetics and the other, finer points of second-messenger systems. Thanks to Matt Scott for his patient and compassionate approach to teaching. And finally, thanks to my daughters, Vera Lynn and Darwin Linnae, for teaching me the patience to deal with adults.

Thanks to many more people, whom I may have forgotten while lost in my studies.

Dedication

This is dedicated to the unsung scientists of history whose prestige society would not propagate. And to a handful of dead white guys.

Table of Contents

List of Tables

List of Figures

Chapter 1

Introduction

The sea slug *Aplysia* belongs to the Phylum Mollusca, a member of the animal kingdom. It is snail-like in shape and slug-like in texture, taking habitat in many oceans and seas around the world. Molecular timescale analysis of invertebrates and vertebrates suggest that *Aplysia* and humans share a common ancestor approximately 1000 million years ago [43]. Despite this seemingly large temporal gap in our molecular evolution, invertebrate research continues to have a positive impact on the state of vertebrate research [7] as convergent and parallel aspects of evolution tie the molecular functions of seemingly disparate species together [62][118]. A common example of this is *gap junctions*[5]. Gap junctions, which facilitate electrical coupling between neurons, are emergent morphological structures. In vertebrates, they tend to be formed of a class of protein called *connexins*. Fruit flies and nematodes, which don't have genes associated with connexin, achieve the same result with *innexins*. Because these distinct species evolved gap junctions independent of another, gap junctions are said to be a convergent trait. Another examples of convergent evolution that is of interest to the present study is *persistent dynamics* in neurons, in which the membrane potential of the neuron oscillates for an extended period of time following a brief stimulus current of sufficient strength. Across nervous systems in nature, persistence serves a broad range of functions, including working memory in humans, motor function in turtles, and escape responses in lamprey [73], as well as lactation and birth in mammals [92]. Because mathematical models can help quantify and inform the details of nervous system behavior, it is of interest to develop neuron models representing distinct neuron traits, such as persistence. Experimental observations of neuron behavior rely heavily on recordings of the membrane potential. Neuron models that explicitly quantify other contributing factors can help give insight into their functional relationships.

In *Aplysia*, the bag cell neuron's persistent behavior, the *afterdischarge*, initiates reproduction. The afterdischarge occurs when a short-term burst of current to a single bag cell neuron initiates a prolonged oscillatory behavior period in membrane potential. In the animal, the entire network of bag cell neurons exhibits afterdischarge behavior simultaneously, with the osccillations occuring synchronously. During this time, bag cell neurons release peptides to the blood stream, initiating egg-laying in the animal for periods as long as a half hour. Upon cessation of the afterdischarge, the bag cell neurons enter a *refractory* period, where they can no longer exhibit afterdischarge behavior in response to

the appropriate pulse stimulus. The refractory period lasts around 18 hrs, at which point the bag cell neuron returns to the *rest state* where the afterdischarge can, once again, be initiated.

One of the key results of this thesis is the development of a mathematical model of the afterdischarge behaviour of the Aplysia bag cell neuron. The model is constructed using the biophysical formalism first introduced by Hodgkin and Huxley [46]. The model is capable of describing the rich dynamics of the afterdischarge and making predictions about how second-messenger mechanisms might contribute to the afterdischarge.

Another novel aspect is the use of numerical continuation and bifurcation analysis on the constructed *Aplysia* bag cell model to give some insight into the roles individual modeling parameters play in excitability dynamics. This helps to tune the model closer to experimental results and provides insight for future corrections and modifications to the model. Finally, the resulting model is extended to an electrically-coupled neuron network. The results of some preliminary exploration of how connection topology affects network behavior are interpreted in light of the limited experimental evidence on biological bag cell clusters.

In the remainder of Chapter One, we cover background topics including dynamical systems, neurobiology, and fundamental concepts in theoretical neuroscience. A methodology section is included at the end of Chapter One. In Chapter Two, we give more details on the methodology of model construction pursued over the course of research. This includes fitting of data from collaborators for individual ion currents, hypothesizing models based on qualitative evidence, and modeling and synthesis of currents into a single bag cell neuron. We consider calcium, potassium, and nonselective channels, as well as their associated calcium-dependent kinetics. This chapter includes many methodological approaches to complex neuron model construction. In Chapter Three, we provide an analysis of the sensitivity of the system through continuation analysis. In Chapter Four, the model is extended to a network by electrically-coupling several instances of the *Aplysia* bag cell model together, with some reproduction-by-simulation of biological experiments on electrically-coupled bag cell neurons. We conclude with Chapter Five, highlighting interpretations presented by the research and suggestions on the next steps to advance the *Aplysia* bag cell model.

1.1 Background

1.1.1 Dynamical systems

Modeling approaches in neuroscience draw heavily on the concepts and language of dynamical systems. There is often overlap in the language between the field of dynamical systems and the language in the fields their models describe. For instance, in biology diffusion often describes molecular transport in a media, but in dynamical systems, diffusion processes are any spatially extended difference process. To add to the confusion, physicists will often call discretized version of diffusion-reaction systems, such as electrically-coupled

neurons, "diffusively-coupled". The author has taken as much care as possible to avoid ambiguities like this, but should one come up, it is safe to assume a physics or mathematics definition lies behind the word.

The discipline of dynamical systems is ultimately the study of how things change in time. In a deterministic system, in which each state in time only has one possible future state, the values over time, or *trajectories*, of the system can do one of four things as time increases:

1. approach a single point
2. begin to oscillate periodically
3. enter more complex behavior such as oscillations with multiple frequencies or chaotic behavior
4. take off to infinity

When a system's solutions approach a single point, it can be said to be approaching the *steady state*, a type of *fixed point* in the system. The steady state is an *attractor* because it attracts trajectories towards it. Attractors may be other objects as well. Oscillations in a dynamical system are associated with a *limit cycle* which describes the oscillations in (at least) two non-temporal dimensions. For instance, for a ball swinging on a string in a frictionless environment, the limit cycle would be traced out by the position, x, and the velocity, v, of the ball. Plotting x vs. v would give a *phase plot* of the system. There also exist *chaotic attractors* that can lead to complex , unpredictable trajectories. Trajectories that approach a fixed point will never quite reach it, and are said to be approaching the fixed point *asymptotically*. The same is true for trajectories approaching a limit cycle or other attractor. Lastly, if the trajectory blows up to infinity, it is likely because of a *repeller*, a fixed-point, limit cycle, or other object in the system that repels trajectories. Only the first two cases will be considered here.

While phase plots are made up of the *variables* of the system, the *parameters*, such as constants in the mathematical model, can be plotted against the fixed-points of the variables in a *continuation curve*. Sometimes changing parameters affects qualitative changes in the dynamics of the system, in which case *continuation curves* becomes *bifurcation diagrams* with *bifurcation points* that govern where such changes (the *bifurcations* themselves) occur. The only bifurcation discussed here is the *Hopf bifurcation*, for which examples will be provided.

Analysis of bifurcation points involve a local measure of how variables relate to each other, known as the *Jacobian*. Information can be extracted from the Jacobian, called *eigenvalues* and *eigenvectors*, giving information about the stability and variable dependencies, respectively, at the point where they are measured.

1.1.2 Biological neuron models

Neurons are unique cells that can transmit electrical signals to each other. The distribution of both positively and negatively charged ions within and around the neuron can generate a voltage potential across the membrane, known as the *membrane potential*, whose value is typically denoted V. Experimental work from the middle of the 20th century eventually led to the development of an approach for mathematical modeling of the electrical activity of the neuron. The canonical experiments and subsequent mathematical development of the original model were carried out by Alan Hodgkin and Andrew Huxley [46][47][48]. In the following, we will describe this approach in the context of ion channels, although these were unknown to Hodgkin and Huxley.

The membrane potential in a neuron is governed largely by populations of *ion channels* embedded in the membrane that selectively allow different currents through at different times, resulting in a change in the membrane potential. The state of the channels themselves are, in turn, affected by the membrane potential, creating a feedback loop. Most channels are *selective*, only allowing a certain species of ion through, but some ion channels are *nonselective*, letting many different species of ion through.

The variables describing the state of the population of a given class of channels are known as *gating variables*. Gating variables that determine the state of the channel populations are represented by a number varying between 0.0 and 1.0. They come in two types: activation variables and inactivation variables. When activation variables are 0.0, the relevant gate for the entire population of channels associated with them are closed, whereas the relevant gate for the entire population is open when the activation variable is 1.0. Values in between 0.0 and 1.0 represent the fraction of channel gates that are open at a given moment. Inactivation and activation gates both follow this convention. Currents typically have both activating and inactivation gating variables. Gating variables are governed by differential equations the form

$$\dot{m} = \frac{m_{ss}(V) - m}{\tau_m(V)} \tag{1.1}$$

The function $m_{ss}(V)$ is called the steady state activation or inactivation, depending on whether m is an activation or inactivation variable and $\tau_m(V)$ is the *time-constant*. The terms "steady state" and "time constant" refer to the roles of these functions in the equation when the voltage is fixed. The author recognizes that "time constant" is a confusing term to use for a voltage-dependent function, but this is the convention in neuron models.

A trace of the membrane potential of a neuron, being the most readily observed quantity in the lab, can give insight into the *electrophysiological activity* of the neuron which relates to how the principles of electrochemistry produce the action potential. In the *voltage clamp* experiment, experimenters fix the membrane potential at a constant value, then observe how membrane currents behave as the membrane potential is changed to a different fixed value. It can help extract the voltage-dependent functions that represent the kinetics of the relevant population of channels. Alternatively, the experimenter may deliver current

to the neuron and measure the response of the membrane potential, often referred to as *current clamp*. Experimentalists can use certain molecules to block some of the channels involved, isolating currents of selected types of channels.

Mathematically, the voltage clamp is derived from the steady solution of the gating variables in Equation 1.1. For a constant voltage, the solution is

$$m(t) = m_{ss}(V_c) - (m_{ss}(V_c) - m_{ss}(V_p))e^{-t/\tau_m(V_c)}. \tag{1.2}$$

The experimental current, I_x can be fit using these equations to determine value of the steady state functions (e.g., h_{ss}) and time-constant functions (e.g., τ_h) for a given clamp potential, V_c, and preclamp potential, V_p. The current, I_x, has the form

$$I_x(t) = \bar{g}_x m(t)^p h(t)(V_c - V_x), \tag{1.3}$$

where I_x is the time-dependent current of channel x, $\bar{g}_x$ is its maximal conductance, m is the activation variable, h is the inactivation variable, p is a power used to shape the curvature of activation, V_c is the clamp potential determined by the experimentalist, and V_x is the reversal potential of current x. A typical curve for a given V_c is shown in Figure 1.1

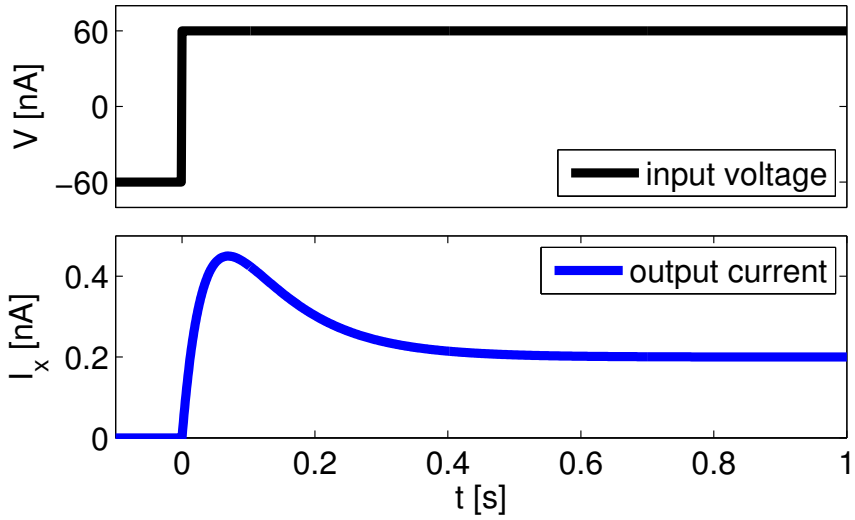

Figure 1.1: A trace of a current from a simulation a typical voltage clamp experiment. Constructed from Eq. 1.3 with $\bar{g}_x = 0.02$ nA, $m_{ss}(V_c) = 1.0$, $m_{ss}(V_p) = 0.0$, $h_{ss}(V_c) = 0.2$, $h_{ss}(V_p) = 1.0$, $\tau_m = 0.05$ s, $\tau_h = 0.1$ s, $V_c = 60$ mV, $V_p = -60$ mV, and $V_x = 10$ mV

Neurophysiologists typically take the resulting set of fits from the voltage clamp experiment and use the points generated to fit to the steady-state and time-constant functions

of a particular gating variable, extracting parameters such as the *half-activation*, the *activation slope*, and the *time constant maximum*(see Figure 3.1). The functions have the form

$$m_{ss} = \frac{1}{2}\left(1 \pm \tanh\frac{V - V_1}{V_2}\right) \tag{1.4}$$

$$\tau_m = \tau_{m0}\left(\operatorname{sech}\frac{V - V_3}{2V_4}\right), \tag{1.5}$$

where V_1 and V_3 are *voltage shifts* that determine the horizontal placement of the function along the V-axis, V_2 and V_4 determine the *width* or *slope* of a function, and τ_{m0} is the *maximum time constant* of the time-constant function. The sign in Equation 1.4 determined whether the gating variable is activating (+) or inactivating (-). The equivalent Boltzmann form is often used rather than the hyperbolic tangets we use here. The Boltzmann form is $\frac{1}{1+e^{(V-V_{q1})/(2V_{q2})}}$.

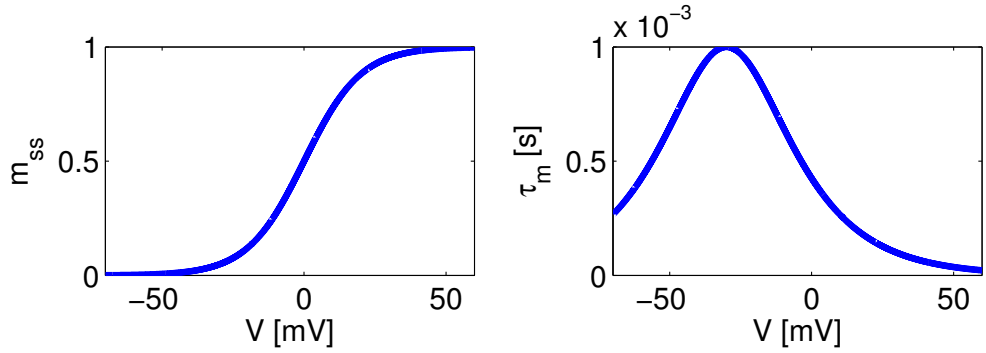

Figure 1.2: Left: steady-state function with *half-activation* or *voltage shift*, $V_1 = 0$ mV and *activation slope* or *width*, $V_2 = 20$ mV. Right: Time-constant function with *maximum time constant*, $t_{m0} = 1 \times 10^{-3}$ s, *voltage shift*, $V_3 = -30$ mV, and *slope*, $V_4 = 10$ mV.

There are different concentrations of ions inside and outside neurons. This difference in concentration determines the *reversal potential* or *Nernst potential*. The reversal potential can be described by

$$V_r = \frac{RT}{zF}\ln\frac{X_o}{X_i}, \tag{1.6}$$

where R is Boltzmann's universal gas constant, T is the temperature, z is the valence of the ion, F is Faraday's constant, X_o is the ion concentration outside the cell, and X_i is the ion concentration inside the cell. Together, Boltzmann's constant and the temperature determine how temperature affects the reversal potential. With higher temperatures, less work (energy) is required to move ions against the diffusion gradient . The resulting reversal potential for that ion would be V_r. The reversal potential defines at which membrane

potential the currents involved in that channel switch from influx to efflux. Note, however, that this simple model applies only to the ideal situation of a single ion species. In a real neuron, where several species are present, the more complicated Goldman-Hodgkin-Katz equation is often employed for detailed channel modeling [45]. The research here depends largely on experimentally-derived empirical values for reversal potentials.

The reversal potentials, determine the driving force for a given current, given a particular membrane potential, via

$$F_x = V(t) - V_x. \tag{1.7}$$

Along with the gating variables the and the maximum conductance, the driving force helps describe the time-dependent current,

$$I_x = g_x m(t) h(t)(V(t) - V_x). \tag{1.8}$$

The current describes the behavior of a particular population (e.g. x) of channels in the membrane. The population may be homogeneous or heterogeneous. A homogeneous population consists of a single type of channel with very similar *subunits* (the component proteins of channels), while a heterogeneous population may contain a lot of variety within it. These nuances don't directly effect the present mathematical formulations, which derive kinetic parameters empirically from experimental results.

A complete neuron model typically requires putting populations of channels into a membrane. The membrane introduces a capacitance as well as a leak current to represent passive currents through the membrane. A simple example lies in the biologically-derived Morris-Lecar model [79]. The Morris-Lecar model is derived from experiments on the barnacle muscle fiber. It can be formulated

$$\begin{aligned} \dot{V} &= \frac{1}{C}(I - g_{Ca} m_{ss}(V(t) - V_{Ca} - g_K n(t)(V(t) - V_K) \\ \dot{n} &= \frac{n_{ss} - n}{\tau_n}, \end{aligned} \tag{1.9}$$

where C is the membrane's capacitance. The steady-state and time-constant functions (m_{ss}, n_{ss}, and τ_n) have the same form as Equations 1.4 and 1.22. Note that the neither the calcium current (Ca) or the potassium current (K) have inactivation gating variables. The time course of potassium activation is determined by the for $\dot{n}$, whereas the calcium current is directly dependent on the steady-state function m_{ss}. The calcium channel reacts to a changing membrane potential much faster than the potassium channel, thus calcium is assumed to have reached its steady-state value by the time potassium dynamics become important. This assumption allows the Morris-Lecar model to perform efficiently in terms of computer resource consumption and simulation times. The first equation of the Morris-Lecar model (Equation 1.9) represents the membrane properties, equating the capacitave

current, $C\dot{V}$, to the ion currents flowing across the membrane. An equivalent formulation of the Hodgkin Huxley model is given by

$$\frac{dV}{dt} = \frac{1}{C}\left[I - I_{Na} - I_K - I_L\right] \tag{1.10}$$

$$\frac{dm}{dt} = \frac{m_{ss}(V) - m}{\tau_m(V)} \tag{1.11}$$

$$\frac{dh}{dt} = \frac{h_{ss}(V) - h}{\tau_h(V)} \tag{1.12}$$

$$\frac{dn}{dt} = \frac{n_{ss}(V) - n}{\tau_n(V)}, \tag{1.13}$$

where m, h are the activation and inactivation gating variables for the sodium current and n is the activation variable for the potassium current.

Most channels implemented in models are voltage-gated, but ion channels can also be ligand-gated, meaning they are activated by molecular interactions. In synapses, channels that rely on ligand activation are defined as *ionotropic*, as their activation allows ions through a pore in the neuron, altering its electrical state. Another class of receptors, called *metabotropic* receptors, act indirectly on ion channels through signal transduction, often modulating the properties of ion channels. Molecules that are involved in this process are known as second-messengers and can often include the ion species themselves. Other ion channels can also be modulated by second messengers. One example of this modulation on ion-channels is thought to underlie *use-dependence* in which Ca^{2+} acts as a second-messenger on Ca^{2+} ion channels through repeated firing of the cell. The repeated firing of the cell causes a gradual increase in the inactivation of the ion channel on a timescale longer than the period of the action potential. Thus the inactivation associated calcium channel is said to be use-dependent.

The action potential is the primary signaling mechanism in neurons, marked by a sharp rise and fall in the membrane potential of the neuron (Figure 1.3). Channels in the neuron membrane maintain multiple feedback relationships between the membrane potential and their conductance state that leads to the threshold behavior neurons are known for. When a sufficient depolarization is introduced to the cell, it activates channels that allow positive ions into the neuron, raising the membrane potential. After some delay, another set of channels opens, letting positive ions flow out and returning the membrane potential back to its rest value.

1.1.3 Behavior of neuron models

Conductance based models like the Hodgkin Huxley model can display a wide variety of behaviors. The three well-known functional classes of neuronal spiking behavior are excitable, oscillatory, and bursting. The most well known class of neuron, an *excitable* neuron, will remain at resting potential until acted on by an external current. This causes the neuron

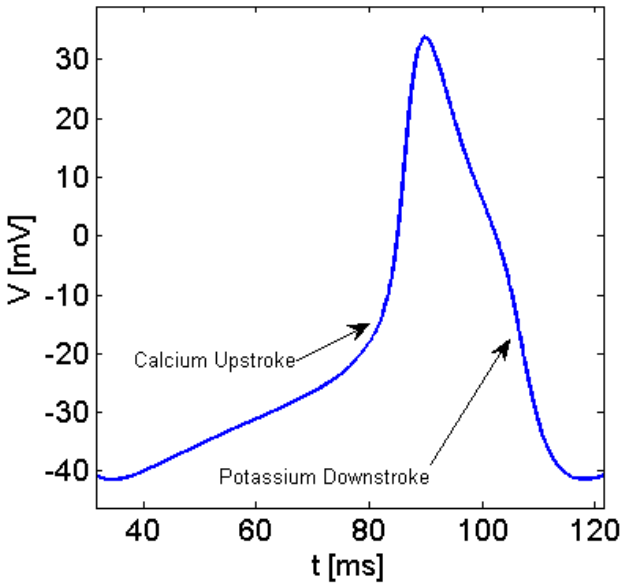

Figure 1.3: The shape of the action potential shows the rise and fall in membrane potential as channels within the membrane open and close. The upstrokes and downstrokes of the action potential result from currents that operate over a similar voltage range. However, the time constant associated with the downstroke is longer than that of the upstroke, resulting in the spike shape of the action potential. In mammals, the upstroke is often generated by a sodium current, rather than a calcium current as shown here.

to enter a transient excitation cycle before returning to the resting potential where it will remain again until perturbed (Figure 1.4, left). Neurons that spike consistently in the absence of an external current are considered *oscillatory*, as they exist on a limit cycle (Figure 1.4, right). One such example is heart muscle cells, referred to as *pacemakers* in neurobiology literature; their constant spiking activity keeps their excitable neighbors synchronized. Both of these classes can be represented by a single two-dimensional conductance-based model, such as the Morris-Lecar model [79]. The third class of neurons, *bursting* neurons, requires a dynamic process on a slow time scale that allows the neuron to enter a short-term oscillatory-like behavior before returning temporarily to a pseudo rest state (Figure 1.5). A canonical example is the Chay-Cook model [90][8].

Bag cell neurons introduce a fourth functional class of neurons, in which a short duration of stimulus leads a nominally excitable cell into a persistent oscillatory fit, followed by a refractory period. The behavior exhibited by such neurons is often called afterdischarge, a behavior typically associated with the pathology of epilepsy [9]. In *Aplysia*, the afterdischarge behavior is not pathological, but physiological, acting as a master switch that initiates the mollusk's reproductive behaviors. Following a short (usually 5-10 seconds) 5 Hz stimulus, a single bag cell neuron will erupt into a fit of oscillatory behavior, lasting approximately 30 minutes, before entering a refractory period, where it returns to normal excitable behavior typical of most neurons. Only during the afterdischarge do ELH levels increase to sufficient level to initiate egg-laying [55]. It is of interest to study the mechanism

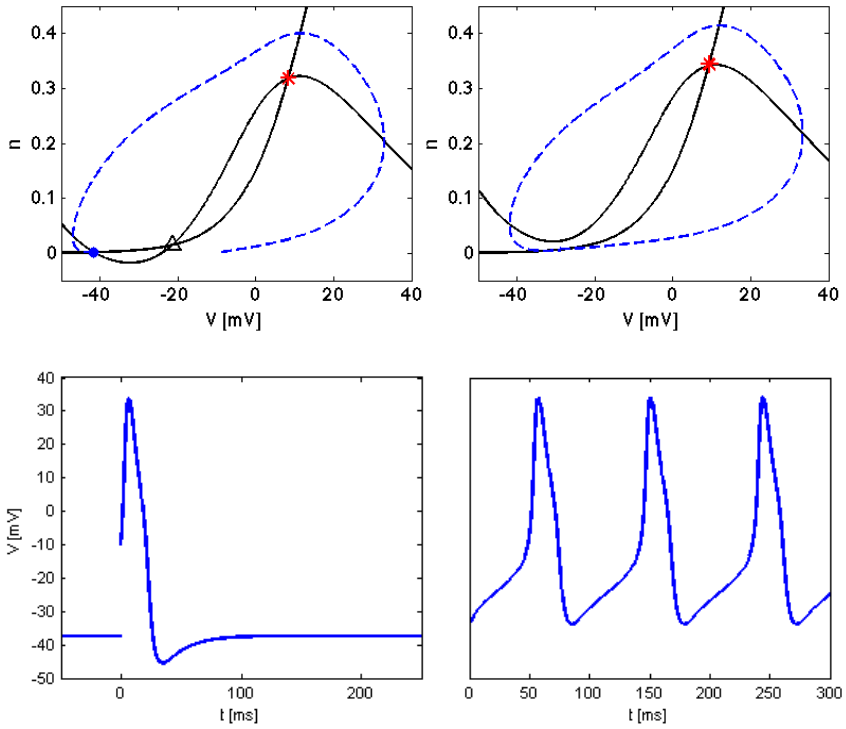

Figure 1.4: Excitatory (top left) and oscillatory (top right) spiking behavior in the two-dimensional phase space of Morris-Lecar neuron model. The phase space of the Morris-Lecar model [79] represents the membrane potential, V, and the potassium channel population's open state, n.

of the afterdischarge for insights into the versatility of neurons as examples of dynamical systems in nature.

Excitable systems of are interest to physicists and mathematicians because excitability dynamics plays a role in many natural phenomena [83][2][84][23][88]. Of particular interest is the behavior of networks of diffusively-coupled ensembles of such excitable elements, which allow for wave propagation. In the case of a neuron network model,, the diffusion is *discretized* (that is to say, the wave propagates from cell to cell rather than through continuous space). The biological literature refers to this arrangement as *electrical coupling*. In nature, the coupling is facilitated by the previously mentioned gap junctions.

1.1.4 Genetic algorithms

The *genetic algorithm* is an optimization method that draws on evolutionary processes to search the parameter space of a model. Like other optimization algorithms, the genetic algorithm tries several different parameter regimes for the model and measures the success of each by comparing it to experimental data. What sets genetic algorithms apart from other optimization algorithms is the way it groups parameters in functionally meaningful ways and generates new parameter regimes from a combination of the traits of successful

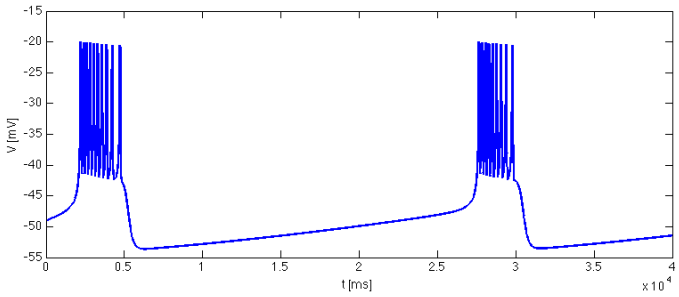

Figure 1.5: Bursting in Bertram's version of the Chay-Cook model [8]. Reproduced with Matlab.

parameter regimes. It then mutates some traits randomly. This final mutation step ensures that the model doesn't get stuck in local minimums (i.e. good fits) and can eventually find the global minimum (i.e. best fit) of the system.

1.1.5 *Aplysia* Biology

Aplysia are a model organism in neurobiology [78], best known for their contributions to a molecular understanding of learning and memory [75][19][6] that resulted from experiments conducted on the gill and siphon withdrawal reflex [20][18][17]. More recent work on *Aplysia* has focused on another pervasive aspect of nervous system function in animals: the electrophysiological regulation of neuropeptides. The bag cell neurons in *Aplysia* releases neuropeptides, called *egg-laying hormone* (ELH), into the bloodstream to initiate egg laying.

Neuropeptides are the largest class of chemical messenger in the nervous system, allowing for the intercellular communication that facilitates important animal behaviors [36][13]. Neuropeptides are produced in neurons and act on the metabotropic receptors of other neurons, facilitating communication between functionally distinct neural populations. Their actions can affect gene expression, regulate blood flow, and modulate synaptic and glial cell morphology of downstream neural populations, leading to emergent behaviors in the organism. In *Aplysia*, the bag cell neuron acts as switch for peptide release in egg-laying processes [76][81][25].

Aplysia have a relatively simple macroscopic architecture to their nervous system. The central nervous system (CNS) of *Aplysia* consists of nine ganglia [63]. At the tail end of the CNS is the abdominal ganglion, which houses the bag cell neurons in addition to the well-studied R15 neuron [3][4][14][16][15][87][110]. Bag cells are found in the abdominal, cerebral, and pleural ganglia of Aplysia and display descending activation in the CNS [42]. They are coupled strongly to their neighbors through electrical synapses, known as gap junctions [55]. In the abdominal ganglia, bag cells exist in two lateral clusters, each containing approximately 200 neurons.

The electrophysiological activity of the bag cell neuron is made up of several ion currents regulated by second-messenger interactions that result in use-dependence, refractoriness,

and the afterdischarge itself. One class of calcium and two classes of potassium channels underlie the action potential of the bag cell [50][98], while non-selective cation channels appear to be responsible for the afterdischarge [50][69]. Additional potassium currents contribute to the refractory period and secondary effects (such as inter-spike timing) [89][70].

Aplysia action potential

In the bag cell, the calcium current is responsible for the upstroke of the action potential. Experimental measurements of bag cell calcium channel kinetics give a reversal potential about 60 mV, a half-activation potential around -6 mV, an activation slope near 5.6 mV, while the inactivation (following a prolonged holding potential of -60mV) has a half-activation around -13.7 mV and an inactivation slope near 10.1 mV [99]. When a sequence of input pulses with duration 50-150 ms is delivered to the bag cell neuron, the calcium channels display use-dependent inactivation [50]. Shorter pulses (10-25 ms) failed to produce a significant use dependence. Calcium channels in the *Aplysia* abdominal ganglion demonstrate a similar use-dependence, thought to be calcium-dependent [22][12][41]. Use-dependence will play a significant role in the dynamics of the bag cell neuron, so it must be carefully considered in the calcium channel model.

The potassium current associated with the fall of the action potential can be separated into two components with distinct kinetics, suggesting two distinct types of channel make up the potassium current [98]. In experiments by Strong, the slower potassium channel, I_{K1} did not demonstrate an appreciable inactivation and was diminished by application of forskolin and theophylline [98]. These chemicals are used by experimentalists to raise cAMP in the cell, a 2nd-messenger known to attenuate potassium currents. The ratio between the two currents varied from cell to cell, ranging from 0.33 to 2.0. Some experimental research has partially isolated I_{K1} by inactivation of I_{K2} via a holding potential of -40 mV, but no kinetics were measured [82]. Expression of the *Aplysia shab* gene in frog oocytes (unfertilized eggs) resulted in a channel with kinetics similar to that of the faster component, I_{K2} [89], supporting Strong's assumption that there are two main components to basal potassium currents. However, it should be noted that Strong's measurements were made by analyzing the tail currents of repolarization in an experiment involving different lengths of voltage steps, not the activation time constant proper. The kinetics of the expressed *shab* channel properties were fit and modeled as two inactivated states and a single activated state, resulting in a complicated electrophysiological description. In concert with a calcium current model of unknown origin, the modeled potassium channels were able to reproduce action potentials similar to those of the *Aplysia* bag cell neuron [89].

The afterdischarge

A train of 150 ms 1.5 nA pulses at 5 Hz with a 10 s duration under sharp-electrode current clamp or a treatment of acetylcholine [104] is usually sufficient to initiate afterdischarge. The stimulus leads to an increase in the amplitude of the membrane potential of the neuron

as well as an increase in the maximum of action potentials. in sharp-electrode experiments, the membrane potential of the bag cell neuron continues to oscillate for approximately 20 minutes [28], during which the frequency of spiking begins to decrease, sometimes with longer delays between bursts. Upon cessation of the oscillatory behavior, the bag cell enters a refractory period, during which stimulus can still excite the bag cell to elicit action potentials, but afterdischarge behavior cannot be evoked for another 18 hours or so. The long-term spiking of the afterdischarge evokes peptide release from bag cell neurons. *Peptides* are chemical messengers that can modulate and activate downstream neurons. In the case of *Aplysia*, the peptides facilitate egg-laying by acting on downstream populations.

Experimental neuroscience literature provides a picture of the mechanisms underlying the afterdischarge. It is suggested that *voltage-independent non-selective cation channels* play a role [99] [50]. The activation of these channels results in a prolonged depolarization current, raising the excitability of the bag cell neuron and bringing an increased calcium influx. The increase in internal calcium concentration levels could lead to the activation of *voltage-dependent non-selective cation channels* [69], allowing a large current through the membrane, which may account for the persistent activation of basal calcium and potassium channels that characterizes the afterdischarge. It has been observed that the increase of inositol triphosphate (IP_3) and protein kinase C (PKC) concentrations near the inside of the membrane leads to a right shift in the calcium dependence of the cation channel, giving PKC a more prominent role in cation channel activity and resulting in a in a lower spiking frequency [37]. The channel is inactivated by protein kinase A (PKA) [69].

Refractory period

After a (roughly half-hour) period of afterdischarge behavior, the bag cell neuron enters a refractory period in which afterdischarge can not occur for around 18 hours. This ensures that downstream egg-laying processes can finish and eggs have sufficient time to mature.

The ability of the bag cell neuron to enter the afterdischarge state is modulated in part by a calcium-activated potassium channel that carries the so-called BK (big potassium) current. Increases in bag cell potassium currents have been observed over three hours after afterdischarge [115], a comparable order of magnitude to the duration of the refractory period. The mechanism behind this persistent behavior has been attributed to several second-messengers, including calcium, PKC, and PKA. The BK current can be upregulated by PKC, increasing the overall potassium current, resulting in decreased excitability in the bag cell neuron. Interestingly, inhibition of PKC by H-7 attenuates the duration of the afterdischarge, but this effect is diminished during the breeding season, when afterdischarge is relevant to reproductive function [102].

PKA also demonstrates regulatory control over the BK current, particularly in adult Aplysia, where increases in PKA activity correlate with a decrease in BK channel activity [113]. Effects of PKA on ELH secretion do appear seasonal, positively correlating with the breeding season in spring, but it's not clear whether PKA's effect on afterdischarge behavior has a seasonal variance [115].

Some experimentalists discuss two types of refractoriness [56], type I referring to the propensity for an excitation on the bag cell process to invade the soma and elicit an action potential, type II referring to the tendency for a bag cell to exhibit afterdischarge. Type I seems to have no correlation with type II.

Bag cell clusters

Bag cells are multipolar neurons with numerous processes extending radially from the soma to the connective tissue [55]. Some of these processes connect to neighboring bag cells. Both types of bag cell processes contain numerous gap junctions. Similar observations were made in culture, where it has further been observed that the strength of the connection corresponded to the proximity of two bag cells. Considerations of spatial distance will not be made here, as this paper encompasses a first attempt at a matured *Aplysia* bag cell model. The point model derived here serves as a natural first step to spatial extensions.

Additional considerations

Outward potassium transient currents, also known as A-currents, provide a small (less than 0.5 nA) current near resting potential, where activation occurs [97]. A-currents are distinct from the fast K_2 potassium current that participates in basal bag cell excitation [98]. A hyperpolarizing pulse to -95 mV will cause the A-current to reach amplitudes over 10 nA, but these holding potentials should be irrelevant to the typical bag cell function. The A current is further diminished by the 2nd-messenger, cAMP [58], which is elevated during afterdischarge [97]. Thus, the A-current will be neglected in the model presented in this research.

Much of the literature covered so far includes various discussion cAMP and its association with the afterdischarge [56][28]. Particularly, cAMP can initiate afterdischarge in bag cell neuron and increase spiking frequency during afterdischarge [58]. This is thought to be due to cAMP's effect on potassium conductance . A complete model may, therefore, require considerations of the modulator effect of cAMP on potassium currents.

1.2 Methods

We use a conductance-based model, similar to the Hodgkin Huxley model. Of 55 parameters used in the final single bag cell model (laid out in Appendix A), only about 25 had data available for fitting. Most of this data pertains to the following parameter sets: calcium activation, potassium activation, all reversal potentials, and much of the voltage-dependent non-selective cation parameters. All available data was provided by the Magoski lab. Conductances, use-dependence, inactivation, and many parameters of the nonselective cation channels were tuned such that they produce the correct behavior in their given contexts, including properties like spike shape, excitability, and propensity for afterdischarge. Some currents observed in *Aplysia* were excluded.

1.2.1 Fitting methods

Data was fit using MATLAB's optimiation tool box. For fitting, functions were chosen that mathematically express current (such as in Equation 1.3) and experimental data provided by the Magoski Lab was used as the input. For whole cell spiking, a least squares fit of the membrane potential was used to quantify deviation of the model from the experimental data.

Kinetics

Fitting of the steady-state functions of the gating variables, and their associated time-constant functions, are performed in two steps, defined here as *Phase I* and *Phase II*. In Phase I, the values of the voltage-dependent steady state function and the voltage-dependent time constant function are determined for each clamp potential, V_c. In Phase II, the steady-state and time constant functions themselves are fit from the points (y_{ss}, V) and (τ_y, V) that result from Phase I fitting.

Phase I fitting

The solution to the activation portion of Hodgkin Huxley model (Eq. 1.11) is

$$m(t) = m_0 - [(m_0 - m_\infty)(1 - e^{-t/\tau_m})]. \tag{1.14}$$

For activation, in which we assume $m_0 = 0$, this reduces to

$$m(t) = m_\infty(1 - e^{-t/\tau_m}). \tag{1.15}$$

For inactivation, in which we assume $h_0 = 1$, the solution becomes

$$h(t) = e^{-t/\tau_h} + h_\infty(1 - e^{-t/\tau_h}). \tag{1.16}$$

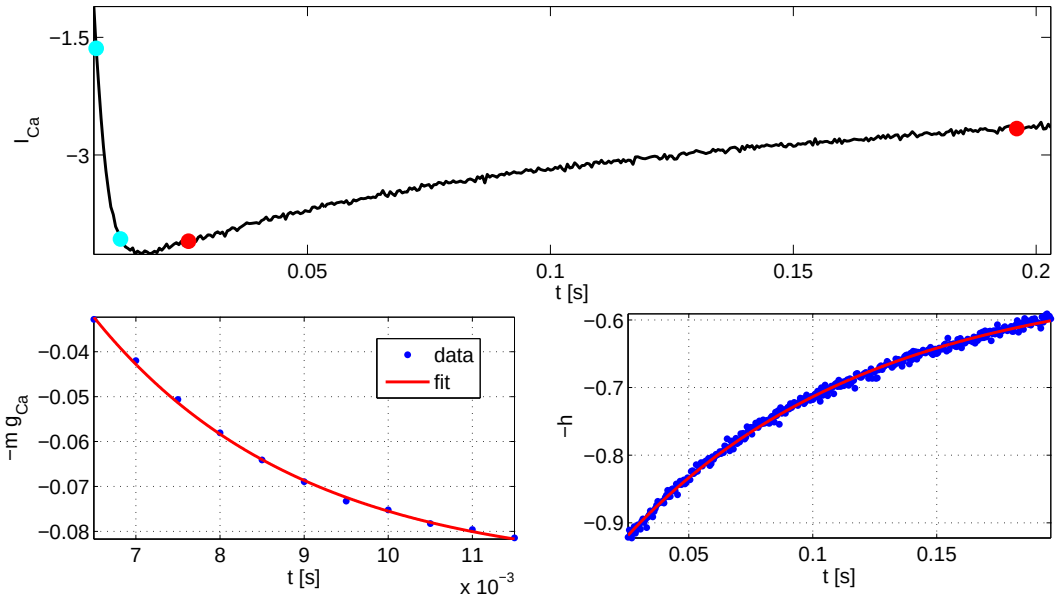

Figure 1.6: The calcium current under voltage clamp experiment discussed in Section 1.1.2 (see Figure 1.1, top). Experimental data provided by Magoskki lab (top) relies on user-selected point for activation (cyan points) and inactivation (red points). Points are selected such that no inactivation is taking place in the activation phase (cyan points) and the activation has reached it steady state value in the inactivation phase (red points). The corresponding mathematical fit is compared directly to the experimental result for activation (bottom left) and inactivation (bottom right).

In Phase I fitting, if we assume a general current, I_x with activation $x(t, V)$ and inactivation $y(t, V)$, a time dependent equation can be fit to the data from voltage-clamp experiments (Figure 1.6, bottom left), using the form

$$x_g = x_{ss}(1 + Be^{-\frac{t}{\tau_x}}), \tag{1.17}$$

where the parameters of interests are the steady state function, x_{ss}, and its associated time constant, τ_x. The parameter, B, allows for a time shift in case $t = 0$ isn't well defined for the experiment. When fitting activation, the quantity x_g is the combined maximal conductance and the activation function for the current, $I_x = g_x x(t)y(t)(V - V_r)$. When fitting activation, we assume that the inactivation, $y_{ss} = 1$, thus

$$x_g = \frac{I_x}{V - V_r}, \tag{1.18}$$

where V is the membrane potential and V_r is the reversal potential of ion x. The resulting x_g can then be used to determine the inactivation, in a similar fit. From the data, I_x, one wants the form

$$y_g = \frac{I_x}{x_g(V - V_r)}, \tag{1.19}$$

as in (Figure 1.6, bottom right) where

$$y_g = A + y_{ss}(1 + Be^{-\frac{t}{\tau_y}}), \tag{1.20}$$

where A is a stand in for the isolated e^{-t/τ_h} term in Eq. 1.16

Typically, experiments will provide data from both activation and inactivation experiments, to better separate the two. In activation experiments, the membrane potential is held at some pre-clamp potential, V_p, then raised to the clamp potential , V_c, which changes with each experiment. In inactivation currents, V_p is typically higher than V_c and it is V_p that varies with each trace while the clamp potential, V_c, remains the same.

Due to the complicated nature of the channels involved, no reliable activation data is available. In the case of the *Aplysia* Ca^{2+} channel, inactivation becomes use-dependent, presumably due to Ca^{2+}-dependence, so a typical inactivation experiment (in which the assumptions is that the current is considered solely voltage dependent) fails to model the mechanics of inactivation. In the case of the *Aplysia* two potassium channels, their inseparability poses numerous fitting problems that have yet to be successfully addressed.

Therefore, all Phase I fitting is done on activation experiments, using the in-step activation. This requires some manual adjustments to inactivation parameters in the ODE model after fitting is completed. Because of the complexity of the bag cell and the variability in some channel properties, adjustment of parameters will ultimately be necessary in the final model and optimization methods will need to be developed.

To assist in comprehensive feedback when fitting channels, a GUI was constructed in MATLAB's GUIDE and implemented for Ca^{2+} fitting (Figure 1.7). The GUI allowed its user to quickly change fitting bounds and select the appropriate points to extract parameters from. This helped visually avoid regions where activation and inactivation overlapped. It also helped with technical details (such as variability in command current onset between experiments). Additionally, it provides a way to visually verify the curve fitting tool is behaving appropriately when variability from different cells is introduced.

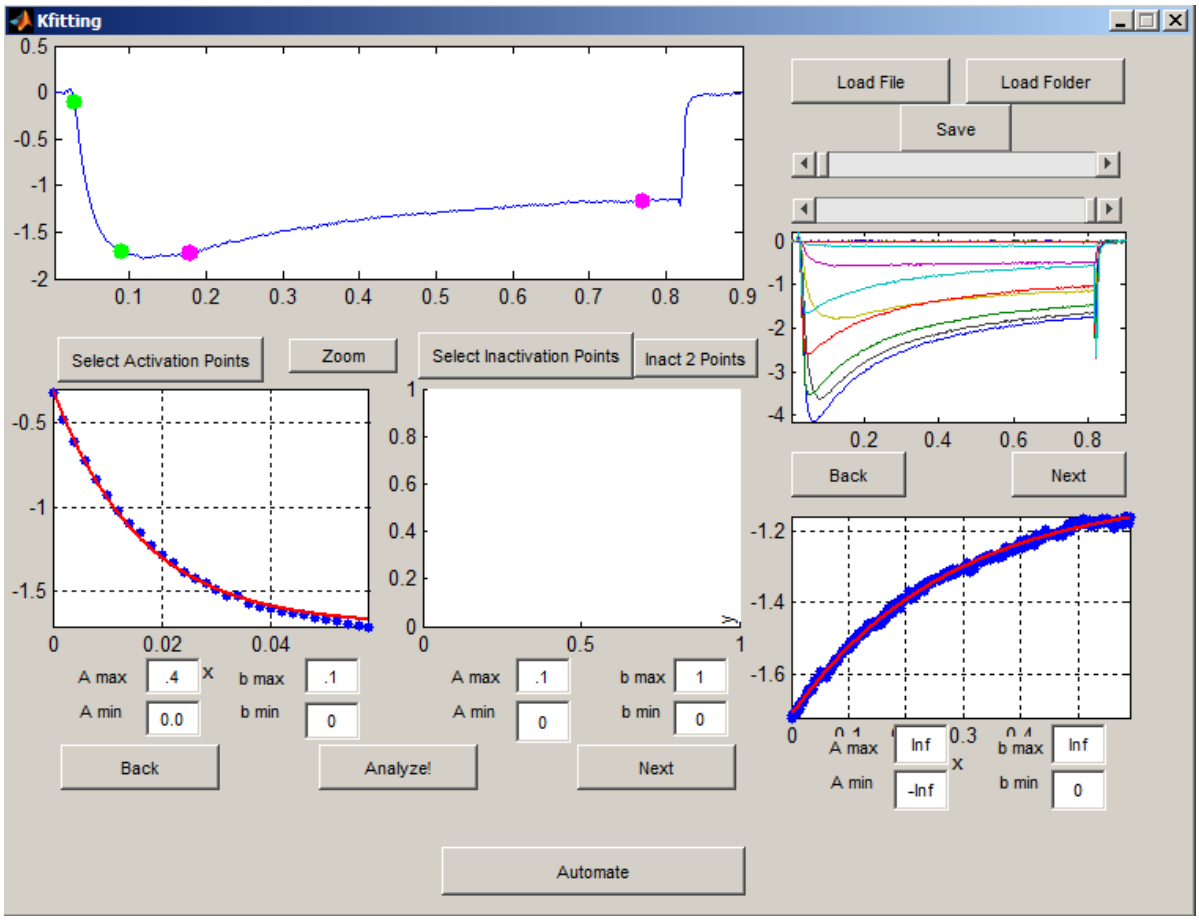

Figure 1.7: A GUI designed in MATLAB for performing Phase I fitting on the Ca^{2+} current. In the top right, a trace is selected for a given clamp potential. Output of fit compared to data is shown in the bototm left and bottom right windows.

Phase II fitting

In Phase II fitting, accuracy and robustness suffer as each of the fits in Phase I has no interdependency on any other fit, so Phase I fitting is blind to Phase II expectations. For simple currents, this can easily be fixed with hand tuning (such as throwing out bad data points or restricting the bounds of the Phase I fit) but for more complicated currents, some innovation is required. This will be discussed more in the potassium fitting section.

Once the data has been collected for each voltage clamp experiment, a collection of points for x_{ss} and τ_x are generated by the Phase I fitting for activation, while a similar collection of points, y_{ss} and τ_y, are generated by Phase I inactivation fitting.

Phase II fitting consists of fitting those points to functions of the form

$$x_{ss} = \frac{1}{2}\left(1 + \tanh\frac{V - V_1}{V2}\right) \tag{1.21}$$

$$\tau_x = \tau_0 \operatorname{sech}\frac{V - V3}{2V4}. \tag{1.22}$$

Examples of the above are given in Figures 1.8 and 1.9 for potassium. Additional fitting procedures are described as needed in the potassium section.

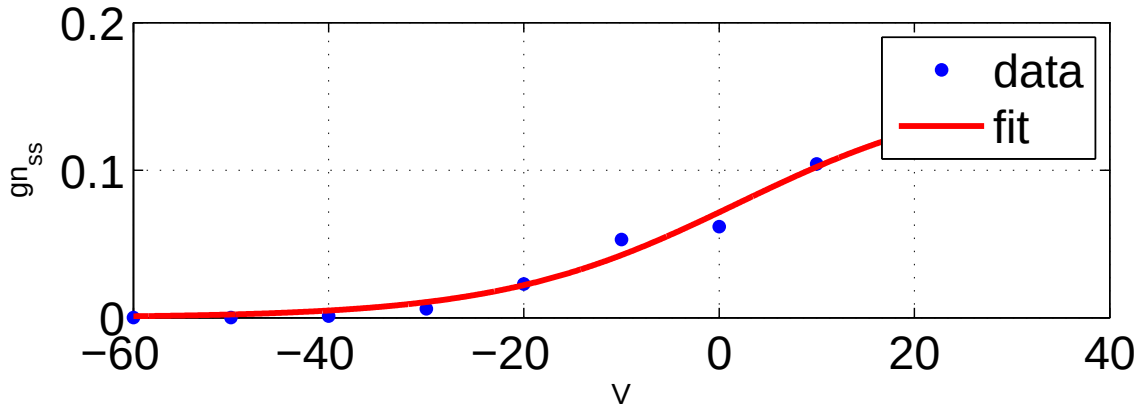

Figure 1.8: Fitting smooth functions (red) to the points retrieved from Phase I fitting (blue) for the K^+ activation function. Data provided by Magoski lab.

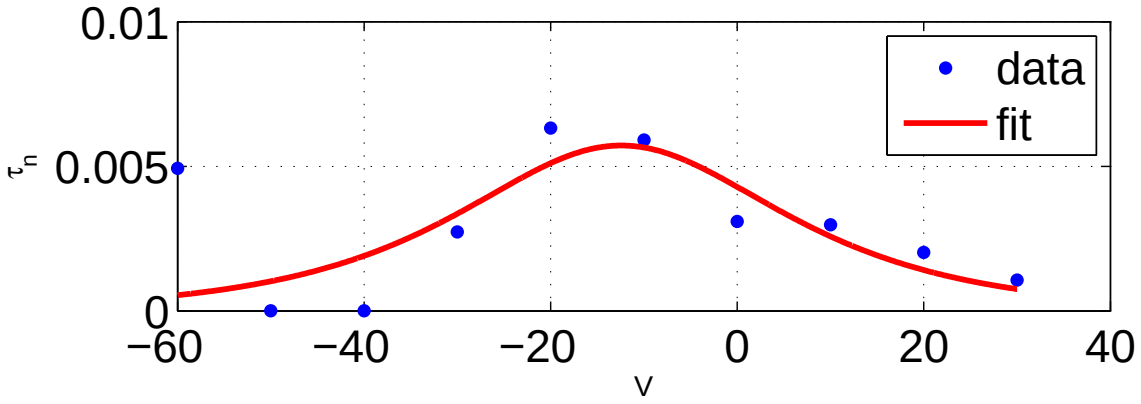

Figure 1.9: Fitting smooth functions (red) to the points retrieved from Phase I fitting (blue) for the K^+ time constant function. Data provided by Magoski lab.

Isolated currents

When current data was available, and once the kinetics of a channel have been determined through fitting, they were verified in simulation, as initial conditions can introduce a layer

of complexity, as is the case with activation and inactivation variables. For them, any error in assumption (such as $h_0 = 1$ or $m_0 = 0$) or calibration of initial conditions during fitting can significantly affect trajectories. To verify the model, an ODE is written for the system with the membrane potential, V, used as a parameter. For each simple current with no modulations, the system is a simple pair of independent ODE's with a voltage-dependent steady state and a voltage-dependent time-constant (Equations 1.11-1.12). Once the gating variables been simulated, the current can be reconstructed as

$$I_x = g_x m(t) h(t)(V_c - V_x), \tag{1.23}$$

where x is the current or ion species being modeled, g_x is its maximum conductance, m is the activation function, h is the inactivation function, V_c is the clamp potential. The resulting curve (t, I_x) is compared to experiment as demonstrated later (Figure 2.7). Note that, unlike the Hodgkin-Huxley formulation, the activation variable, m, in the current equation is simply m, not m^4, as Ca^{2+} activation slopes tend not to have as pronounced of a sigmoid shape as sodium channels (Figure 1.8).

1.2.2 Voltage-independent nonselective cation current

No direct kinetic data is available for voltage-independent nonselective cation channels, but some observations of its relationship to calcium concentration have been quantified [50]. In this paper, it is modeled with activation and inactivation functions, analogous to the voltage-dependent activation functions described above. Unlike calcium and potassium currents, the time-constant was chosen as a true constant, and not a function. Lacking explicit measurements of the time-constants, they are chosen to be large enough that the depolarization preceding the onset of afterdischarge occurs after cessation of the external applied current.

1.2.3 Voltage-dependent nonselective cation current

Unnormalized data was provided by experimental collaborators (normalized data published in Lupinsky, 2006 [69]) and a fit was performed on two voltage-dependent curves with varying calcium concentration to determine how calcium concentration altered the voltage-dependent parameters (i.e. the half-activation and the activation slope). The calcium current's maximum time constant for activation, τ_{m0}, was chosen as the time-constant for the voltage-dependent cation current,

1.2.4 Afterdischarge simulations

To elicit afterdischarge in the model, a train of pulses at 5 Hz with a 10 s duration was used. The amplitude was 1.4 nA and the pulse width was 150 ms, corresponding to an on-rate of 75% in the 200 ms duration of the cycle (Figure 1.10). In the present model,

the long-term calcium delay, r, acts like an integrator on this *command current*. That is, the area under the curve of the command current determines the influx of calcium in the model. Channels dependent on this calcium influx were tuned such that a 5 Hz, 10s, 250 ms duration command current would provide sufficient calcium concentration to evoke afterdischarge. Alterations to the command current can, therefore, lead to more excitability (evoking afterdischarge quicker) or less excitability, leading to little or no spikes before returning to the depolarizes resting potential.

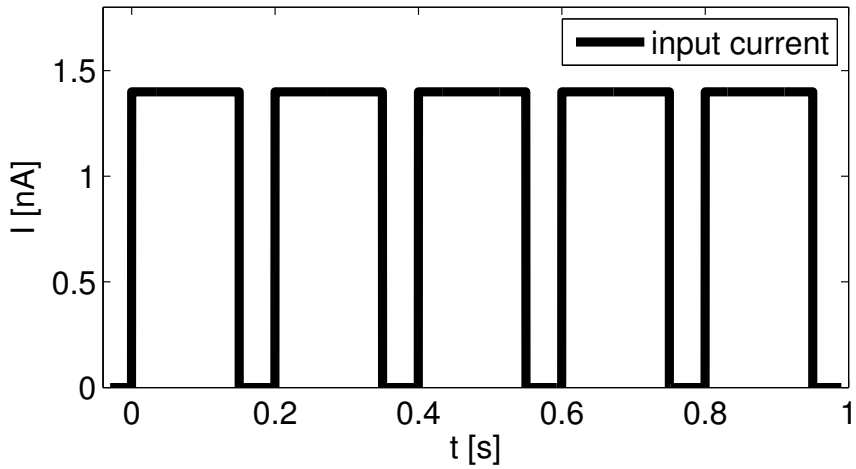

Figure 1.10: The command current. A 5 Hz pulse with a 150 ms width and 1.5 nA amplitude. The command current is typically delivered for 10 s, only 1.0 s shown here.

With limited experimental data on nonselective cation channels, many of its parameters were tuned manually such that they would reproduce afterdischarge.

1.2.5 Whole cell optimization

Because of the inherent nonlinearities that restrict analytical solutions, the Jacobian of the system can also be difficult to compute, since analytical solutions are often not available. The Jacobian must be analyzed numerically and cannot be given in a functional form that would be of advantage to common optimization methods. This makes the genetic algorithm a natural choice for model construction and parameter tuning [91][38][53]. Genetic algorithms (Figure 1.11) consist of a series of steps in which parameter points are tested and ranked, and successful parameter points (those which produce neuron-like spiking) exchange some parameter values with other successful parameter points (Crossover or Mating). After exchanging parameters sets, individual parameters are randomly selected for mutation and the process begins again with the new set of parameter points (dubbed "offspring" of the original parameter points). In genetic algorithm nomenclature, the parameter sets are *chromosomes*, while each parameter in a parameter point is a *locus*.

In the present study, two different genetic algorithms are implemented. One was engineered from scratch in MATLAB, while the other is MATLAB's onboard *ga.m* from the

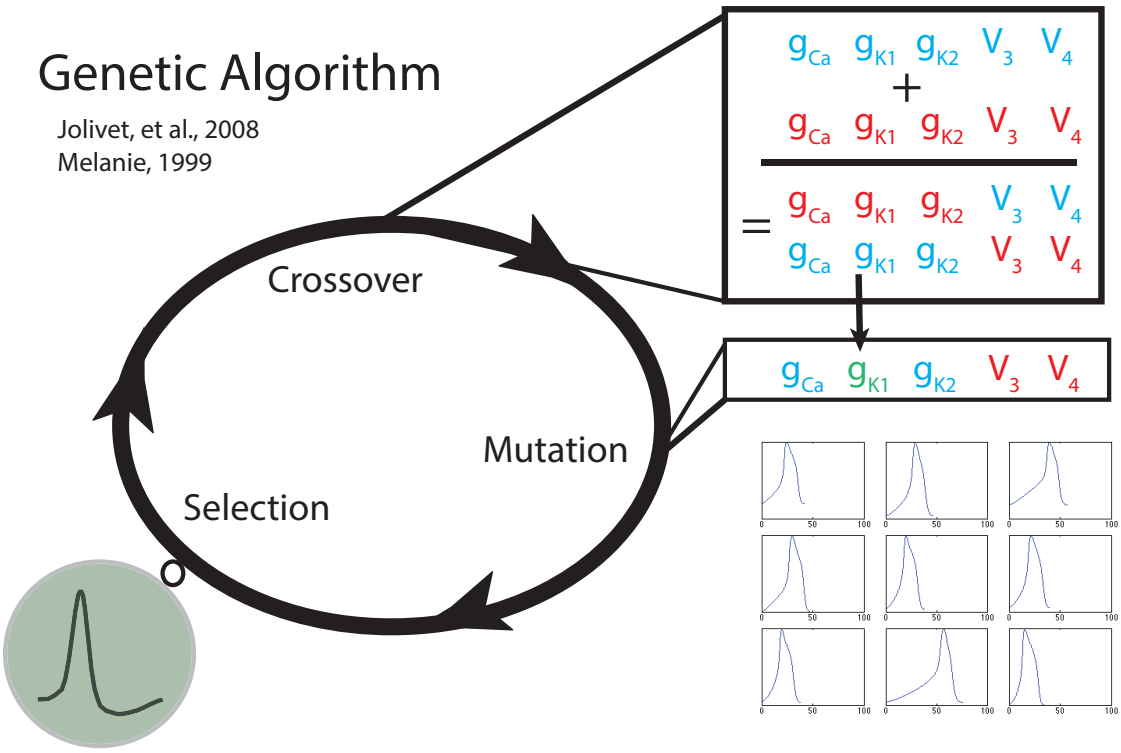

Figure 1.11: Selection: The genetic algorithm considers a population of parameter points and tests them against experimental data. Crossover: parameter points that score well on the tests swap some parameter values with other successful parameter points (as in top, right box). Mutation: Some parameter values are randomly selected and altered slightly. The new crossed, mutated parameter sets are tested and the cycle repeats. Lower-right inset: examples of results from successful parameter points.

Optimization Tool Box. The homemade genetic algorithm was implemented as a proof-of-concept and used to quickly find a parameter regime in the Morris-Lecar cell with added Ca^{2+} kinetics that could reproduce the trajectory of the membrane potential observed in experiments. Initial parameter points are generated as a small distribution around the nominal parameter values of the Morris-Lecar neuron. Then, a least-squares-fit between experiment and simulation results was used to rank the parameter points. After several generations of ranking, crossover, and mutation, a good fit of the Morris-Lecar neuron to the *Aplysia* bag cell neuron results (Figure 1.12).

Following this exercise, MATLAB's onboard genetic algorithm was implemented for the full bag cell model, as discussed in the Synthesis chapter.

1.2.6 Continuation Analysis

Continuation analysis is performed using Matcont, a MATLAB package. The user provides an input file defining the system of ODEs to be studied. The equilibria of the model depend on a given control parameter. In our case, the external applied current is used as the control

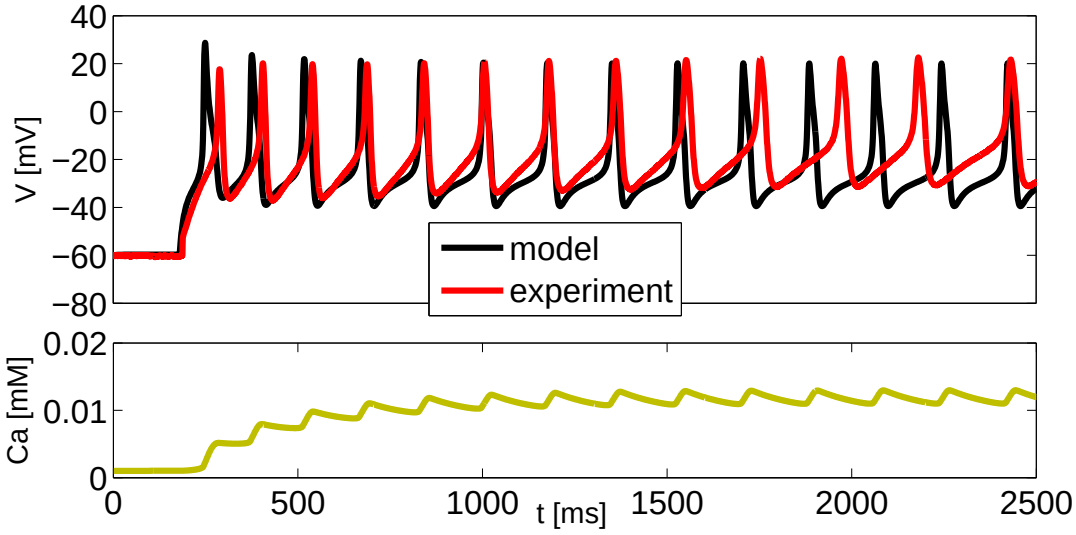

Figure 1.12: Replicating aplysia bag cell spiking behavior (red) with a 2D Morris-Lecar model (black) the model uses a floating Nernst-like reversal potential, dependent on the Ca^{2+} concentrations of an internal domain (yellow).

parameter. Thus continuation curves show how points and stability change as the applied current varies. Matcont also provides limit cycle continuation, which is implemented on Hopf points in the present thesis, to show where periodic behavior might exist in the system.

1.2.7 Network

A range of coupling constants for network simulations were chosen through trial and error to produce a network that propagated excitation. The numerical values of this range varied for different network topologies. Coupling constants at the lower end of the range are defined as *weak*, while constants at the higher end of the range are considered *strong*.

Network topologies were chosen first, for simple analysis (as in the ring network) of wave propagation. Once basic network nuances were determined in this simple case, cluster and scatter topologies were implemented.

Chapter 2

Model Construction

We are interested in a theoretical validation of what experiments seem to suggest: that calcium plays a critical 2nd-messenger role in onset of the afterdischarge. Model construction is, therefore, guided largely by experimental data pertaining to this question.

In order to answer the question of the mechanisms driving afterdischarge, we wish to construct a biologically accurate model of the bag cell neuron that includes appropriate channel mechanics. This allows components of the model to be related to experimental observations and can make model results informative by reproducing biology experiments *in silica*. Since the afterdischarge pertains to action potentials of the bag cell neuron, the primary currents of the bag cell action potential must be modeled

For the typical ion conductance model, a neuron is reduced to a point model: a unit area of membrane with channels and their associated second-messenger systems embedded within. This point model can be generalized for most cases [1]. A great deal of model construction consists of modeling the kinetics of the channel, especially when kinetic design is guided by experimental evidence. When such data is available and model assumption are valid, channel design hinges on accurate fitting of the data to the appropriate equations. There are many distinct phases of fitting, each with their own caveats. Some accuracy is lost at each stage of the fitting, depending on how well-behaved fits are. In Phase I fitting, the results of voltage clamp experiments for various values of membrane potential, V, are fit as a function of time to extract the time constant and steady state values for each value of the membrane potential. In Phase II fitting, a fit of the these values as a function of the membrane potential is produced to be implemented directly in the differential equation. The methodology of this process is available in Methods (Subsection 1.2.1).

After channel models have been constructed and implemented through Phase I and II fitting, any associated second-messenger systems are then added to the existing channels and some manipulations will often be required to get the fit result matching the experiment again. In the case of the *Aplysia* bag cell, the Ca^{2+} channels exhibit a use-dependence that appears to be moderated by a second messenger system involving, Ca^{2+} binding with calmodulin.

Once models for all the major contributing ion channels and their second messengers have been constructed, a synthesis protocol is required to bring them together into a single,

comprehensive model of the *Aplysia* bag cell membrane potential. In the synthesis stage, the relative conductance of each channel is manipulated, along with the capacitance and applied current of the membrane. Further, a leak channel is added to represent unmodelled currents and to set the resting potential of the cell.. This can be a difficult and tedious task when guided by intuition alone, making optimization software necessary. Because the gradient of such complex systems can't readily be computed, genetic algorithms often make an efficient choice for testing the parameter space. During this phase, kinetics should not be altered unless they have to be, as the kinetics are informed by experiment, but relative conductance can vary greatly depending on patch size and animal channel distribution variation.

Once a region of parameter space is found that produces classic neural behavior with the main contributors to current, secondary channels and additional second-messenger kinetics can be applied that serve modulatory purposes. In the case of *Aplysia*, the secondary channels are nonselective cation channels, which are presumed to be responsible for the onset and duration of the afterdischarge.

Analytical solutions to the whole cell model are seldom available, thus computationally-expensive numerical solutions are required. The effect of parameter changes in the system must be measured by simulating its trajectory through phase space, and comparing the observable variable (membrane potential) to experimental results. Further, adjustments to the system are often unintuitive and can lead to losses in other aspects of model accuracy. It is therefore beneficial to use a genetic algorithm to optimize the selection of parameter points. In this way, many different parameter points can be simulated and only those matching the successful condition are manually verified.

2.1 Ion current models

2.1.1 Calcium current

Calcium data for the *Aplysia* bag cell was provided by the Magoski lab, including both published [50][99] and unpublished data. Experiments resulting from several different bag cells provided consistent results when it came to fitting the activation and its associated time constant.

A first attempt at fitting calcium compared the disjoint method (Figure 1.6), in which activation is treated separately from inactivation, to the full trace method [105]. The full trace method involves fitting the complete current equation, rather than independently fitting activation and activation. Constants of the equation

$$I_{Ca} = m_{ss}(1 - e^{-(t-t_0)/\tau_m})(h_{ss} + (1 - h_{ss})e^{-(t-t_0)/\tau_h})(V - 60) \tag{2.1}$$

are fit directly to experimental data.

The full trace method fits both activation and inactivation simultaneously, using data from both activation and inactivation experiments. As stated previously, calcium inactivation data does not fit the assumptions of a purely voltage-dependent channel, so the in-step inactivation was used to represent inactivation data for the full trace method.

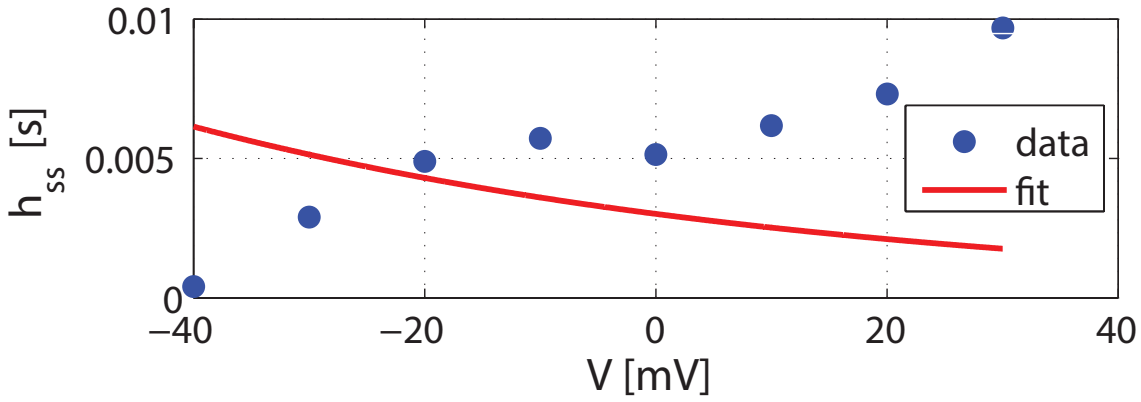

Figure 2.1: An attempted fit (red) of Ca^{2+} using the full trace method (Equation 2.1), fitted to data (blue) from experimental collaborators [50].

However, a difficulty arises with the full trace method in fitting. Because the activation and inactivation steady state values are being fitted simultaneously and each voltage clamp fit is independent of other voltage clamp fits, there is no unique combination, $m_{ss}h_{ss}$ and the resulting values are noisy and arbitrary. This often resulted in meaningless results for Phase II fitting (Figure 2.1). Eventually, the disjoint method (Eq. (1.17-1.20) and Figure 1.6) was used in place of the full trace method, yielding a more biologically consistent result (Figures 2.2 and 2.3).

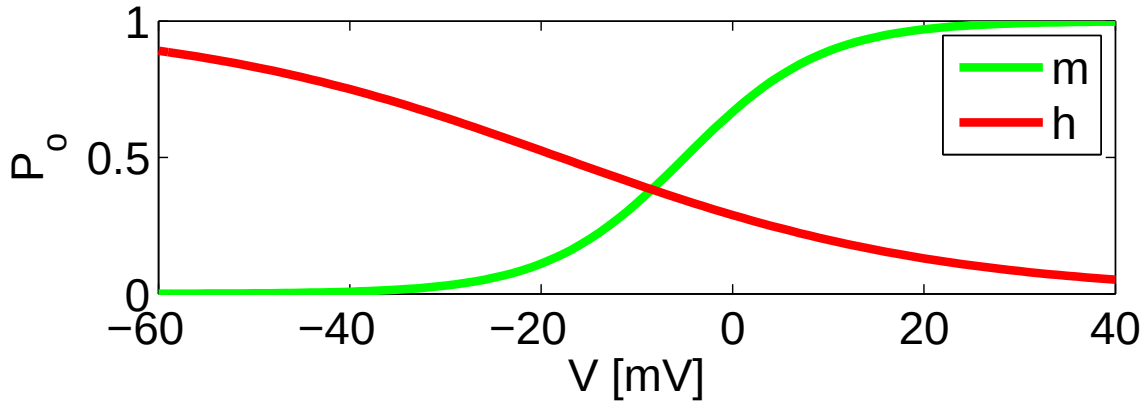

Figure 2.2: The activation function, m (green), and inactivation function, h (red) for Ca^{2+} using the disjoint method for fitting (Subsection 1.2.1). Data provided by experimental collaborators [50].

In total, data from eight different cells were used, implementing the disjoint method on data provided by the Magoski Lab, kinetic parameters were extracted with the Phase I and

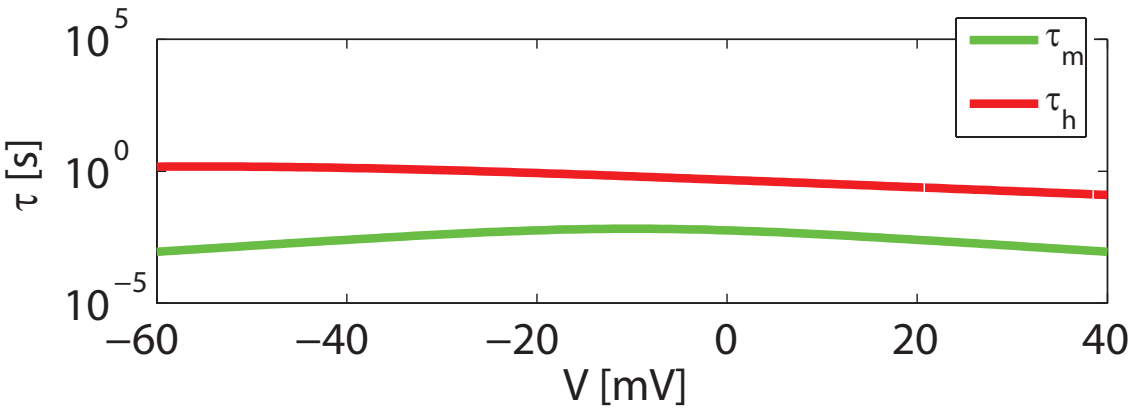

Figure 2.3: Time constants functions for the activation, τ_m (green), and inactivation, τ_h (red) for Ca^{2+} using the disjoint method for fitting (Subsection 1.2.1). Data provided by experimental collaborators.

Phase II fitting methods described previously. Results for calcium channels show robust kinetics (Figure 2.4). Values are provided (Table 2.1) along with a correlation table that shows interdependency between parameters (Table 2.2). Knowledge of the correlations between parameters helps when manually tuning the model or when devising rules for optimization. Changes in one parameter often require adjustments in other parameters to maintain desired model behavior. This is often the case for highly correlated parameters. Using the correlation table, when necessary parameter adjustments produce undesired results, additional modifications can be attempted on parameters that correlate well with the changed parameter. The correlations were computed using MATLAB's *corr.m*, which computes the pairwise correlation coefficient via the Pearson method. Examples of both highly correlated (-0.96) and poorly correlated (4.6×10^{-3}) parameters resulted (Figure 2.5). It's not surprising that V_5 and V_6 are correlated, as they are parameters in the same steady-state activation function; the shift and the slop, respectively. This negative correlation implies that an increase in one requires an decrease in the other to compensate and maintain a consistent calcium response. This assertion relies on the assumption that experimentalists are providing data of what they consider to be in the range of typical calcium response for an active cell.

Aplysia bag cells display use-dependence in their calcium channels which is thought to be Ca^{2+}-dependent [50]. With repeated firing, calcium channels become more and more inactivated. A first attempt at modeling use-dependence assumed that changes in the internal calcium domain would lead to changes in the reversal potential, V_{Ca} of calcium channels [109]. This, in turn, would reduce the driving force $(V - V_{Ca})$. A preliminary model was able to reproduce use-dependence experiments. However, it did so with the compromise of changing the kinetics fit from activation experiments. No parameter regime was found in the system which reproduced both activation experiment and use-dependence experiments simultaneously.

The present author later discovered a calcium-based use-dependence model that had already been established for *Aplysia* abdominal ganglia [21] in which Ca^{2+} binds to a protein

	0002a	0006a	0008a	2002	4000	4004	1004	Tam
V_1 [mV]	-7.23	-6.80	-4.47	-4.13	2.29	-17.28	-1.17	-6.30
V_2 [mV]	12.73	10.60	12.60	11.61	11.49	11.37	12.30	11.20
V_3 [mV]	-24.63	-21.43	-18.75	-	-	-	-	-13.70
V_4 [mV]	19.56	21.20	21.38	-	-	-	-	20.20
V_5 [mV]	-17.03	-11.60	-23.57	-14.21	-45.03	-42.58	-10.54	-10.54
V_6 [mV]	11.68	9.79	11.56	10.15	15.77	17.52	8.72	8.72
V_7 [mV]	-100.00	-9.18	-28.83	-12.75	1.94	-100.00	-100.00	-100.00
V_8 [mV]	42.89	20.11	32.87	17.44	24.02	27.23	23.24	23.24
τ_{m0} [ms]	0.02	0.01	0.01	0.02	0.03	0.01	0.02	0.02
τ_{h0} [ms]	0.42	0.26	0.34	0.27	0.30	0.92	1.31	1.31
g_{Ca} [mV]	0.08	0.05	0.06	0.10	0.13	0.03	0.07	0.07
V_{Ca} [mV]	-	-	-	57.35	52.58	40.10	54.38	54.38

Table 2.1: Fitted parameter values resulting from the disjoint method (Section 1.2.1) for their given File ID and the Tam paper results [99].

	V_1	V_2	V_3	V_4	V_5	V_6	V_7	V_8	τ_{m0}	τ_{h0}	g_{Ca}
V_1 [mV]	1.00	0.11	-	-	0.07	-0.31	0.77	-0.17	0.63	-0.86	0.84
V_2 [mV]	0.11	1.00	-	-	0.07	-0.07	-0.41	0.81	-0.01	-0.03	0.14
V_3 [mV]	-	-	-	-	-	-	-	-	-	-	-
V_4 [mV]	-	-	-	-	-	-	-	-	-	-	-
V_5 [mV]	0.07	0.07	-	-	1.00	-0.96	0.13	-0.00	-0.29	-0.55	-0.14
V_6 [mV]	-0.31	-0.07	-	-	-0.96	1.00	-0.37	0.09	0.19	0.75	-0.02
V_7 [mV]	0.77	-0.41	-	-	0.13	-0.37	1.00	-0.69	0.29	-0.77	0.48
V_8 [mV]	-0.17	0.81	-	-	-0.00	0.09	-0.69	1.00	-0.13	0.22	-0.12
τ_{m0} [ms]	0.63	-0.01	-	-	-0.29	0.19	0.29	-0.13	1.00	-0.32	0.93
τ_{h0} [ms]	-0.86	-0.03	-	-	-0.55	0.75	-0.77	0.22	-0.32	1.00	-0.57
g_{Ca} [μS]	0.84	0.14	-	-	-0.14	-0.02	0.48	-0.12	0.93	-0.57	1.00

Table 2.2: Correlation of fitted parameter values, n=8, computed by taking the cross-correlation between fitted parameter results.

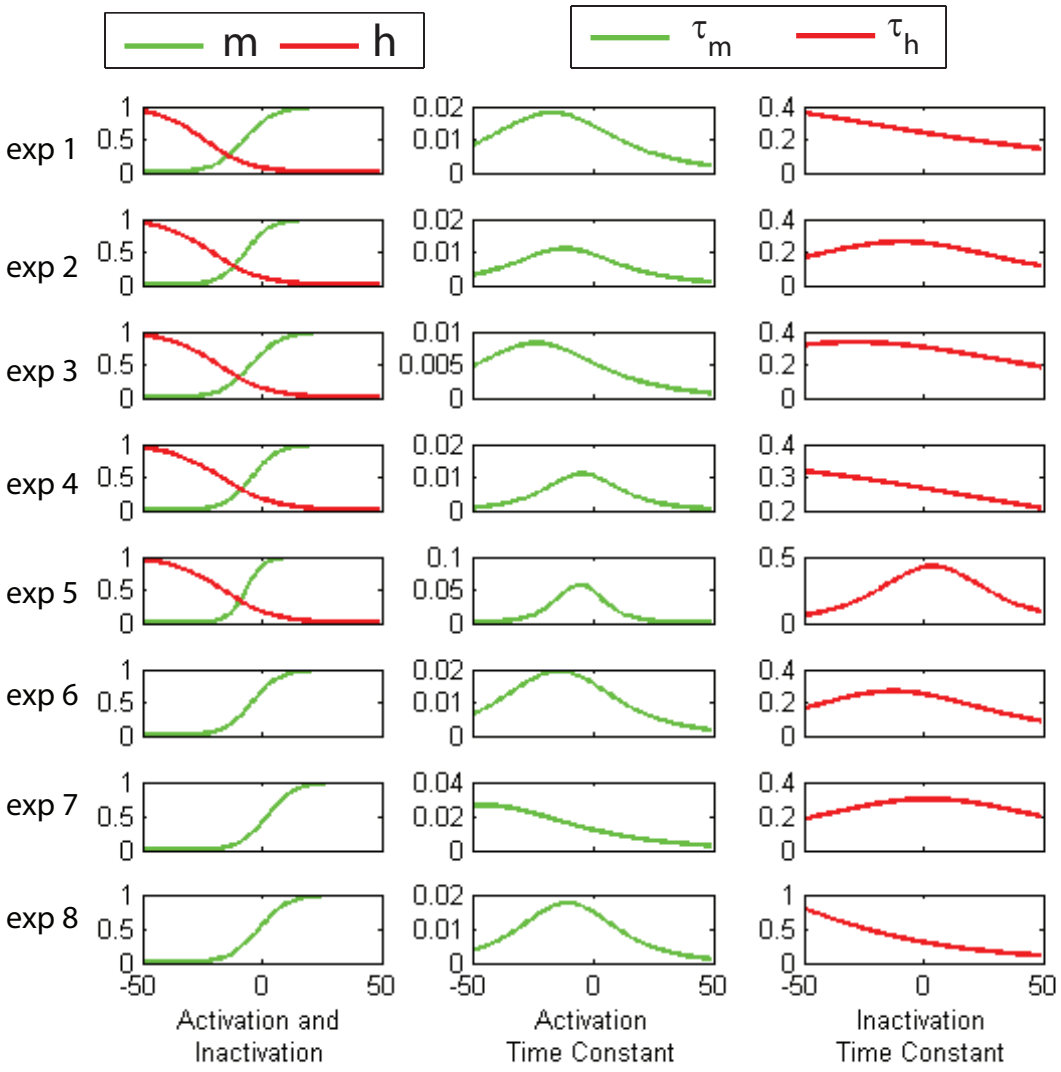

Figure 2.4: Results of fitting from multiple calcium channel voltage clamp experiments. Data provided by experimental collaborators. No inactivation experiments were performed on exp 6-8

(presumably Calmodulin) through which it can modulate channel dynamics. Building from the original model, a voltage-dependent inactivation is added. The full calcium channel model is described by

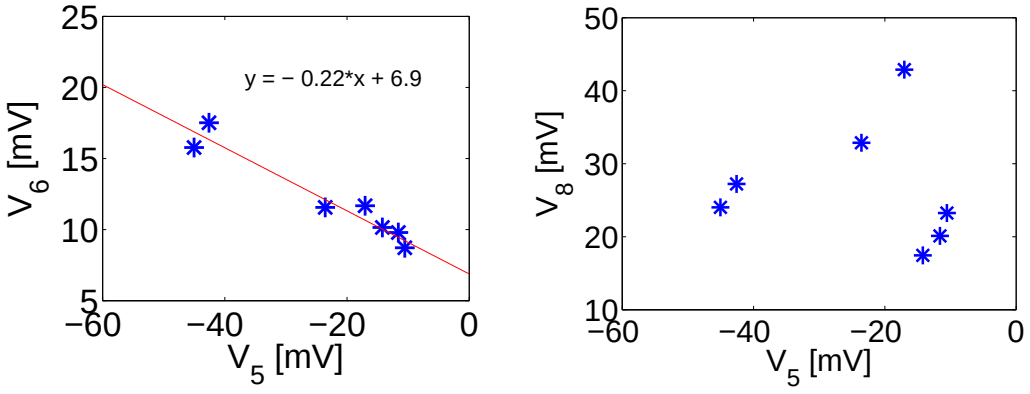

Figure 2.5: Examples of highly correlated (left) and poorly correlated (right) parameters as fitted from experimental data.

$$\dot{m} = \frac{(m_{ss} - m)}{\tau_m} \tag{2.2}$$

$$\dot{h} = \frac{(h_{ss} - m)}{\tau_h} \tag{2.3}$$

$$\dot{s} = \frac{(1 - P_b) I_{Ca}}{-2Fv} - D(s - s_0), \tag{2.4}$$

where m and h are the usual Hodgkin Huxley gating variables and s is the calcium concentration. In Eq [2.4], P_b is the probability of a single Ca^{2+} ion binding to buffer, F is Faraday's constant, and v is the volume defining a microdomain near the channel inside the membrane. Calcium leaves the microdomain with the rate of diffusion, D, until the uniform internal calcium concentration, s_0 is reached.

The calcium-dependent inactivation is implemented on the calcium current via

$$I_{Ca} = \frac{g_{Ca} m h (V - V_{Ca})}{1 + Ks} \tag{2.5}$$

where K describes the channel's inactivation sensitivity to Ca^{2+}. Note that the calcium concentration has units of M. This choice of units is arbitrary; as long as any changes in the units of calcium are reflected in K and, later, calcium dependent activation functions, then no numerical values need to be changed and the resulting simulation will have the same outcome. To make the conversion, one would simply change all units of M to (for instance) μM.

In the present study, this model is adapted to the calcium channel and acts similarly to voltage-dependent inactivation (Figure 2.6). The calcium-dependent inactivation does not replace voltage-dependent inactivation in the calcium channel, but supplements it. No explicit fitting took place. Rather, through trial and error, the channel is simulated and

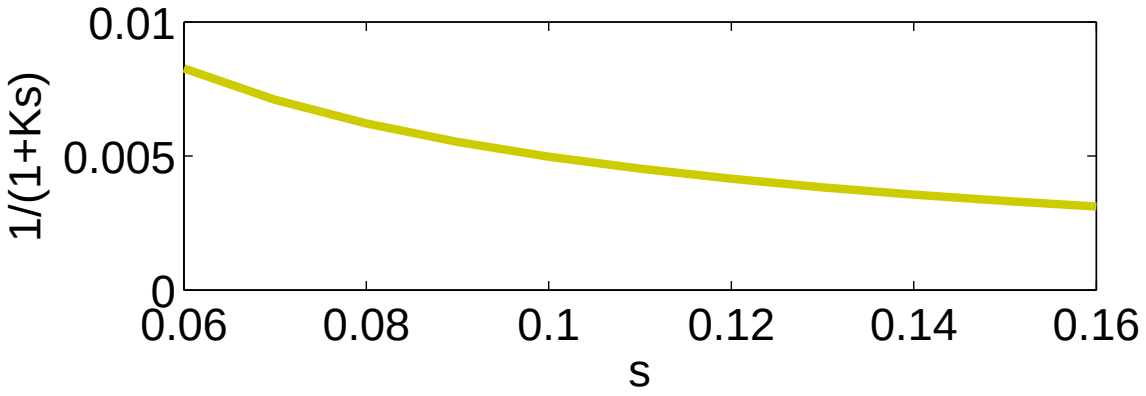

Figure 2.6: Calcium-dependent inactivation of the calcium current as a function of Ca^{2+} concentration, s, using a model derived from observations in neurons L2 through L6 in the *Aplysia* abdominal ganglia [21].

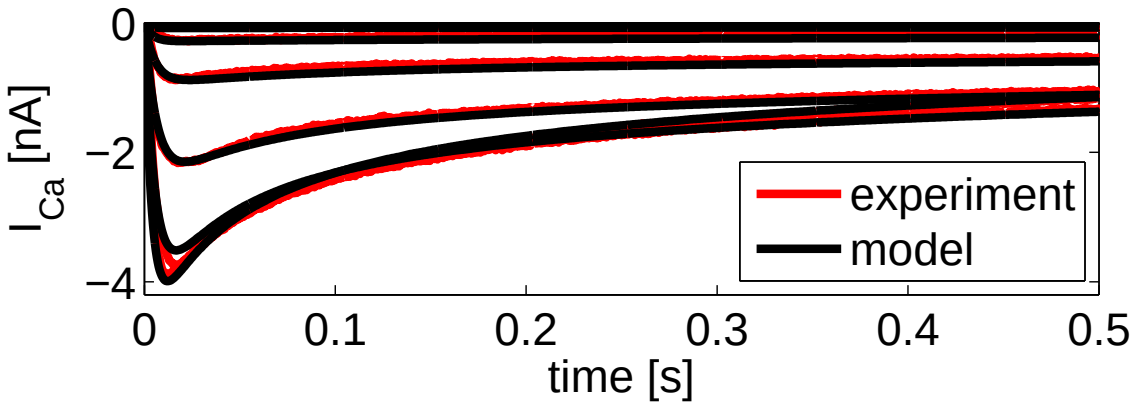

Figure 2.7: A simulation of the calcium channel model (black) under voltage clamp compared to the experimental voltage clamp (red). Data provided by experimental collaborators.

compared to the associated activation experiment (Figure 2.7). Additionally, a simulation replicating experimental conditions [50] is run (Figure 2.8). These results validate the calcium channel model.

As a final step, calcium-dependent *enhancement* is added to the calcium current model. Previous research has observed that enhancement is mediated via protein kinase C (PKC) and acts to recruit calcium channels, augmenting the calcium current [31]. Here, we model it as a direct dependency on calcium,

$$\bar{G} = g_{Ca}(1 + m\frac{1}{2}(1 + \tanh\frac{Ca_i - Ca_1}{Ca_2})), \tag{2.6}$$

where g_{Ca} is the conductance when minimal Ca^{2+} is present, m dictates how much calcium increases g_{Ca}, such that fully activated enhancement is $(m+1)g_{Ca}$, Ca_1 is the half-

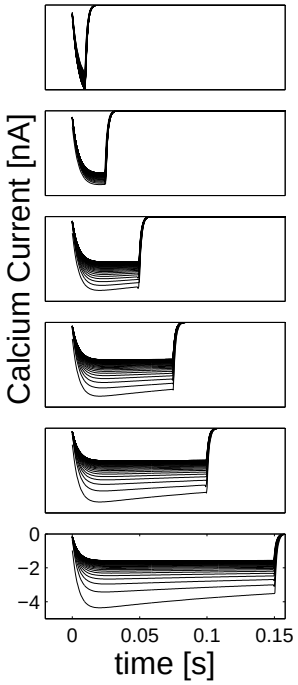

Figure 2.8: A simulation of use dependence in the calcium channel model yields similar results to experiment (Figure 6D *in vitro* from Hung, 2007 [50]).

activation of the enhancement, and Ca_2 is the slope. Enhancement parameters are tuned after implementation of nonselective channels, to assist in reproducing the afterdischarge.

Together, standard Hodgkin-Huxley gating, a calcium-based use-dependence, and calcium-dependent enhancement make up the complete calcium channel as it is modeled in the whole bag cell neuron.

2.1.2 Potassium Channels

It has been known for decades that the *Aplysia* bag cell neuron has two components to the potassium current [98]. The currents are, thus far, inseparable via standard channel blocking methods. The slow current, I_{K1}, and the fast current, I_{K2}, make up the potassium current via Kirchoff's current law

$$I_K = I_{K1} + I_{K2} \tag{2.7}$$

where the individual currents are defined by

$$I_{K1} = g_{K1} m(V,t)(V + 80) \tag{2.8}$$
$$I_{K2} = g_{K2} q(V,t) p(V,t)(V + 80) \tag{2.9}$$

where g_{K1} and g_{K2} are the maximal conductances, $m(t,V)$ and $q(t,V)$ are the typical activation variables, $p(t,V)$ is an inactivation variable, and $(V+80)$ is the driving force (assuming the potassium reversal potential is $V_K = -80$). Notice that I_{K1} does not have an inactivation variable associated with it, as experimental literature reveals that the K_1 channel shows "little or no inactivation" [98].

First attempts at resolving the ambiguities of two potassium channels involved using the Quattrocki model [89] to describe I_{K2}. In the associated experiment, Quattrocki expressed K_2 potassium channels in frog *oocytes* (unfertilized egg cells) and typical voltage clamp experiments were performed on the oocyte patches, resulting in the development of a model through fitting and finding appropriate functions. Because the Quattrocki experiment isolated K_2 from K_1, attempts at modeling the full potassium current involved taking data from the Magoski lab (which includes both currents) and subtracting the model-derived K_2 from the data. However, the Quattrocki model presented many conflicting and problematic characteristics and was eventually abandoned.

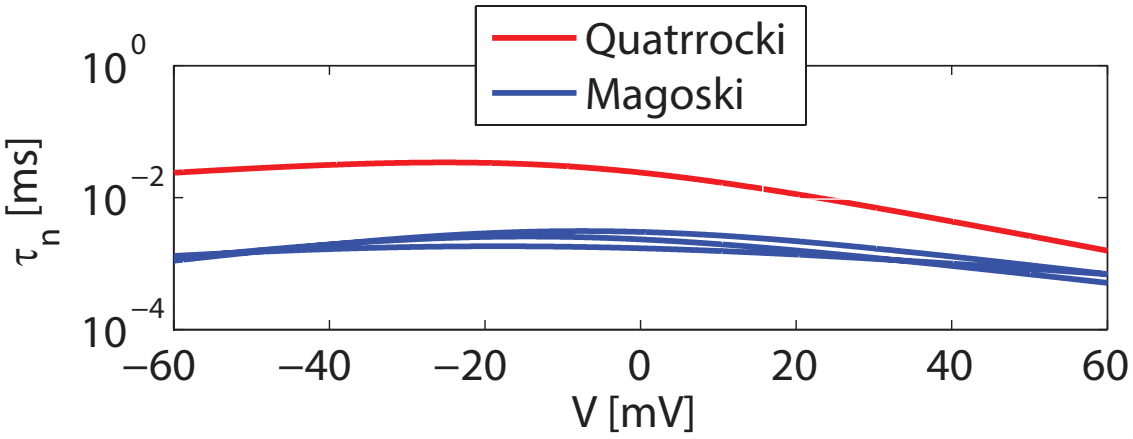

Figure 2.9: Comparison of K^+ activation time constants for Quattrocki [89] model (red) to a fit constructed from data provided by experimental collaborators for three different cells (blue).

The first conflict with the Quattrocki model was an order of magnitude difference in the activation time constant for K_2 when compared to data from collaborators (Figure 2.9).

Additionally, the formulation of the Quattrocki model is such that any adjustments or manipulations made to the system can cause numerical problems as solutions blow up or time steps approach zero. While one can take care to simply avoid regions where these issue occur, it severely limits the capabilities of optimization methods (like the genetic algorithm and the human-GUI interface) and requires hardcoding additional constraint considerations and loss of generality. This is because of the choice of equations used to represent the time constant and the steady state functions for the Quattrocki model which cross zero and blow up for large membrane potentials. Any horizontal transformations made to these functions could cause artifacts in the physiological range.

Another source of conflict with the Quattrocki data is that oocyte capacitance may significantly alter the wave form [111]. The systems context is lost in the isolated K_2

experiment. In nature, where many channels are present, molecular *crowding* occurs, which can play a significant role in cell kinetics [80]. Another phenomena, *cooperation*, can occur as different ion species interact with buffers and 2nd-messenger systems. There is no way to know how system phenomena like crowding and cooperation alter membrane responsiveness to current. The membrane of a bag cell neuron is a complicated electrochemical system and presents a different biological context than a lab-prepared oocyte.

An alternative to fitting separated currents is to attempt fitting both potassium currents simultaneously. The previously mentioned issue with fitting independent voltage traces applies even more strongly in the case of two currents. Using standard fitting practices yields noisy, nonsensical results when there is no unique solution. To account for this, the present study relies on "parameter forcing". With two superimposed currents, a total of eight functions exist to describe the voltage response over time in the potassium current. Each parameter is plotted and fit as usual with the addition of tight bounds. This allows the user to control the general shape of some functions in ways that they expect the outcome to be, given the data. For instance, K_2 is much faster than K_1, so the two are bound in their relative magnitudes (Figure 2.10). Similarly, activation functions are constrained to be activating (so that they start low and end high) and inactivation functions are constrained to be inactivating (so that they start high and end low). The parameter forcing avoids situations such as occurred with the full trace method (Figure 2.1). However, parameter forcing does not avoid the problem of multiple solutions when such solutions are physiologically meaningful. Adjusting the time constant to match experimental data is not a trivial process given the complicated form of the model, so this approach was not pursued.

Another consideration when fitting potassium parameters is that potassium tends to have a lot of variety across cells within a single organism. While calcium channels tend to be robust, potassium channels tend to be diverse [27] and, with respect to the *Aplysia* bag cell, can change channel density based on activity[117].

Bag cell excitability varies from cell to cell. Experimental data on the kinetics of potassium cells does not discriminate based upon whole cell excitability. To track how variability in potassium channels related to cell excitability, experimental collaborators at the Magoski lab provided data from cells containing both potassium voltage clamp experiments and whole bag cell spiking experiments for the same cells. Some cells did not spike at all or spiked poorly (Figure 2.11), so their potassium profiles were ignored. From the cells that spiked more robustly (Figure 2.12) potassium voltage clamp profiles were taken for fitting and the resulting values entered into the parameter forcing program for Phase II fitting.

Initial attempts at fitting in this way appeared to go well when directly fitting the voltage-dependent functions to the data (Figure 2.13), but when the derived parameters were put into the ordinary differential equation, the results lost significant accuracy (Figure 2.13, blue squares). The source of this discrepancy was found to be due to initial conditions for the activation of each channel and inactivation of K_2, adding three additional fitting parameters. Two of these three parameters have multiplicative operations between them which can be satisfied by a large range of physiologically reasonable values, introducing

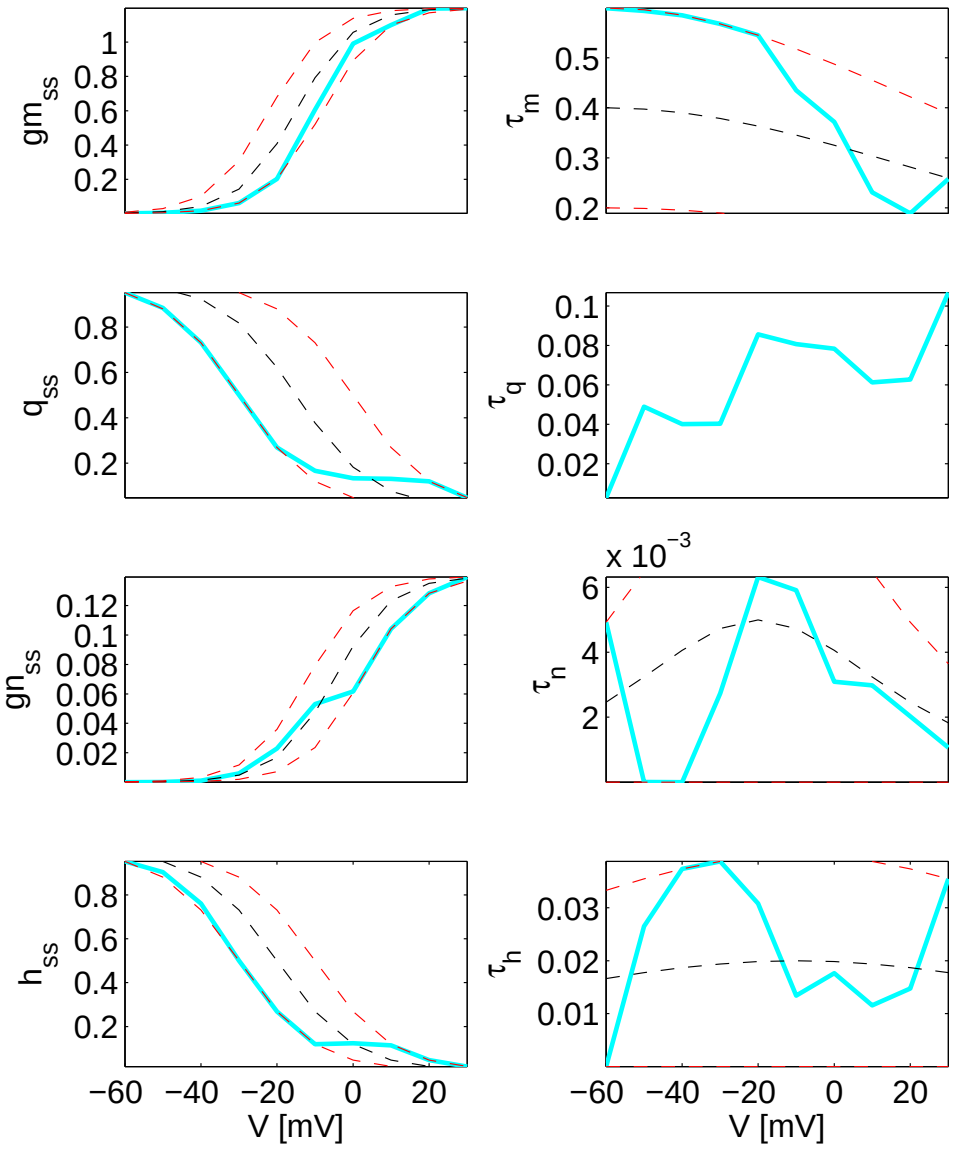

Figure 2.10: Parameter forcing method. Forcing is implemented by constraining maximum and minimum of fit with a voltage-dependent function (red lines) and providing a suggested value (black lines). The fit results (blue lines) are often noisy and require forcing for them behave in a biologically plausible way.

more ambiguity to the fitting result in the form of noise. In addition, it is the nature of excitable systems that they demonstrate some sensitivity to initial conditions.

The errors resulting from fitting the time constants, which were still quite noisy themselves (Figure 2.10, right hand column), likely also played a significant role. When tuning the system by hand, small changes to achieve one result would compromise changes to other characteristics of the channel's time course under voltage clamp.

To avoid the many complications encountered above, one particular potassium profile from experimental collaborators in which the whole cell still demonstrated spiking stood

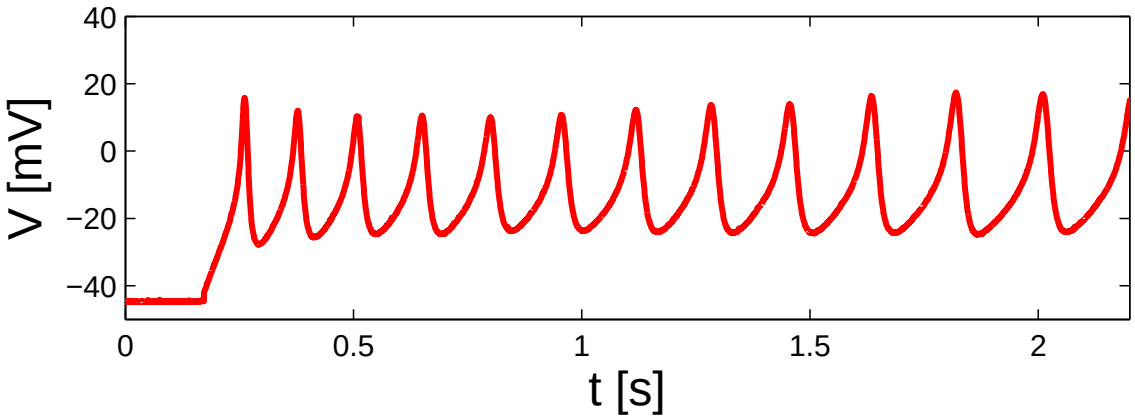

Figure 2.11: Experimental measurement of the membrane potential of a bag cell with medium excitability spikes under constant current injection. Data provided by experimental collaborators.

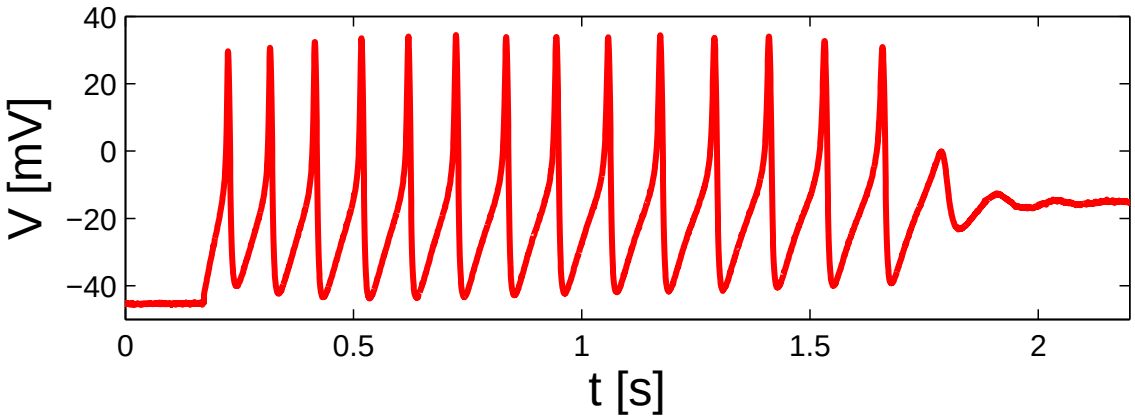

Figure 2.12: The recorded measurement of a spiking bag cell, held under constant current injection. The membrane potential saturates around -18.0 mV. Data provided by experimental collaborators.

out. Unlike most profiles, the time constants for the activation of K_1 and K_2 appear to be closer together, allowing one to fit the voltage clamp experiments as if there were a single channel involved (Figure 2.14).

Therefore, the single-channel is implemented in the final prototype of the *Aplysia* bag cell neuron, forgoing some early, fast potassium current for a simple implementation. Neglecting this nuance may affect action potential shape or alter eliminate important short-term behavior, but separating the currents has proven to be too cumbersome during first construction of the model.

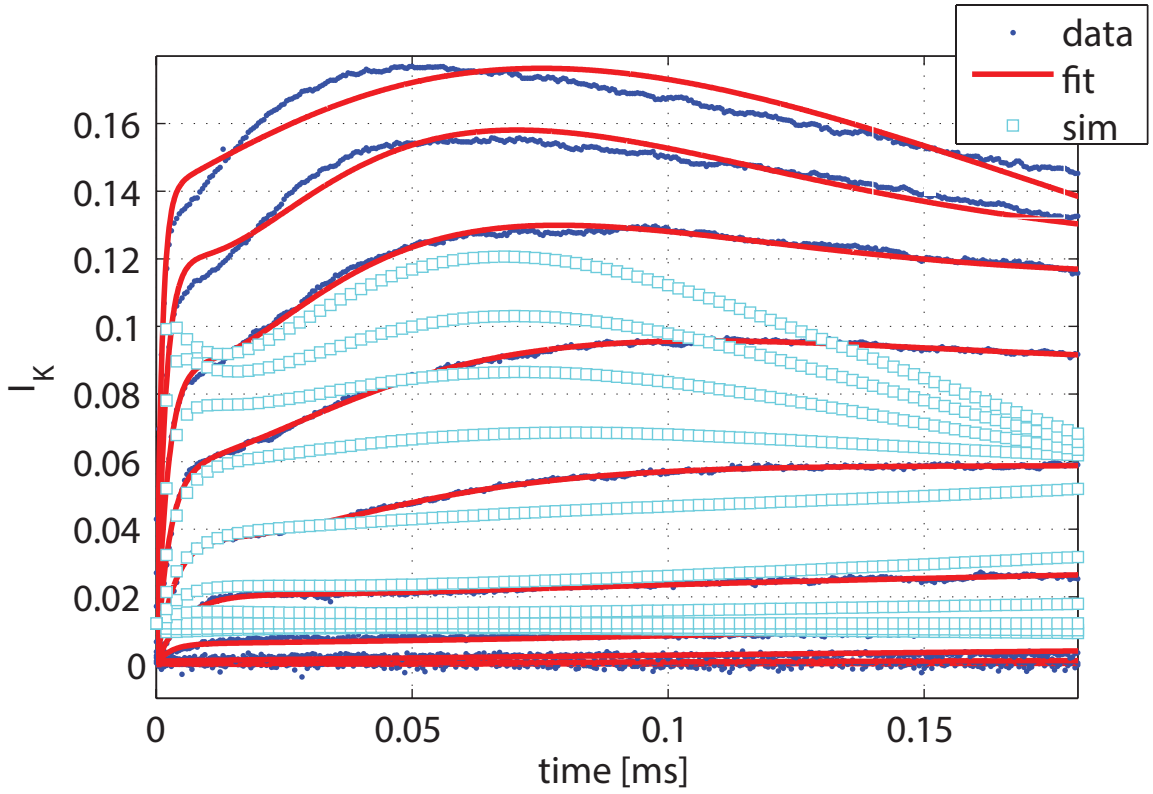

Figure 2.13: The direct fit solutions for voltage clamp (red) compared to the experimental data (blue) and the ODE-generated simulation result (blue squares). Experimental data provided by collaborators.

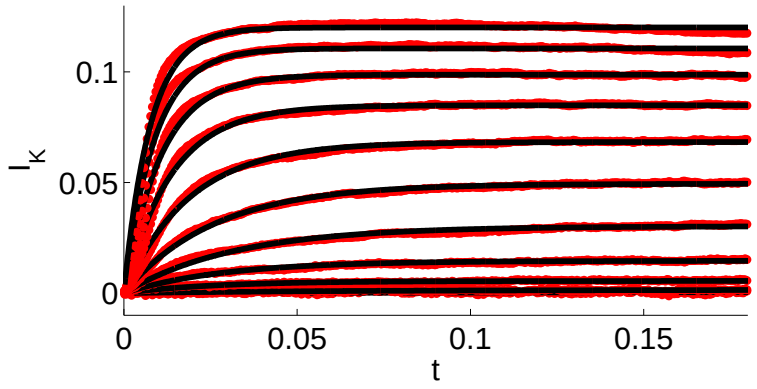

Figure 2.14: K^+ experiment (red) compared to a simplified single-current model (black). The cell that produced this potassium curve also produced spiking (Figure 2.12). Data provided by experimental collaborators.

2.1.3 Synthesis of Currents

Once individual channels have been constructed from voltage clamp studies, the whole membrane can be constructed. However, at this point, many parameters become relevant

for which there is no standardized data. In particular, the relative conductance of each channel is an open question. While some measures are available, they vary greatly from experiment to experiment depending on cell membrane variability, cell size, patch size, junction potential compensation, capacitive artifacts, and variability in driving and recording amps. Using the conductance from a calcium experiment along with the conductance from a potassium experiment is a meaningless combination given all the different environmental factors that contribute to the conductance measurement for each. Experimental intuition can, however, inform order of magnitude. Using reasonable bounds, informed by experiment, can help focus a numerical search for the appropriate parameter space.

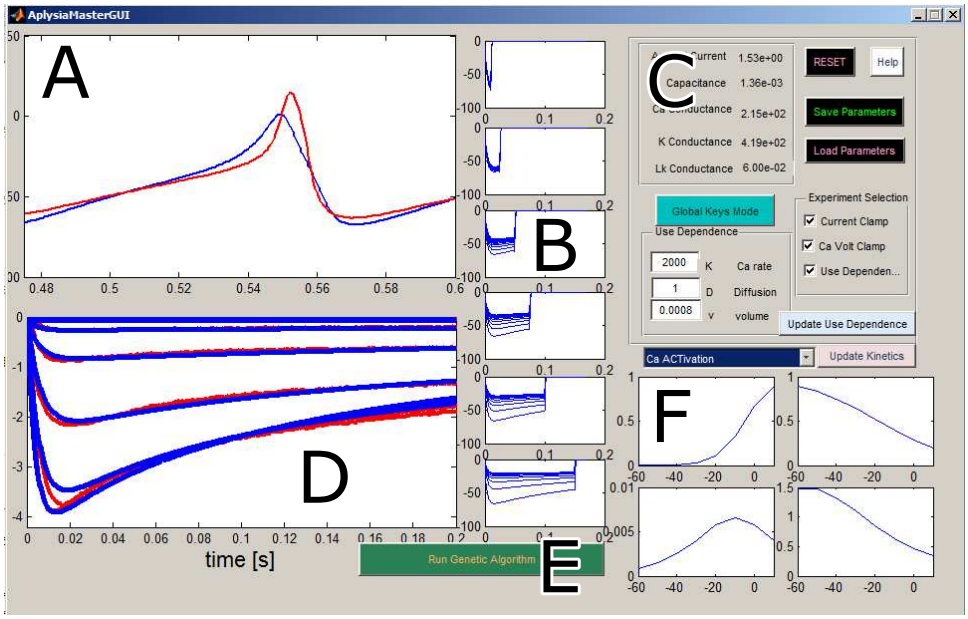

Figure 2.15: GUI program for parameter refinement. A - Output for whole bag cell model (blue) compared to experiment (red), B - Output for use-dependence simulation of model, C - Master control panel, D - Output for Ca^{2+} voltage clamp simulation (blue) compared to experiment (red), E - Genetic Algorithm button, F - kinetics manipulator. See Figures 2.16-2.18 for details.

For the present study, a sufficient bag cell model must do three things. It must reproduce, with reasonable accuracy, the voltage spike waveform when run as a current clamp, the calcium voltage clamp experiment, and use-dependent inactivation. For use-dependent inactivation, a series voltage clamp pulses are delivered to the bag cell and the resulting current is measured. Given the inherent variability in potassium, potassium parameters are more free to assist in producing the correct spike shape and timing. For each manipulation made to the model to better align it with one test, care must be taken that alignment is not lost with another test. To ensure this, a GUI was constructed to provide an immediate visual output for all three tests (Figure 2.15, A, B, and D). When changes are made to the parameter point (Figure 2.15, C, F, and E) the GUI automatically updates the visual output (A,B, and D) to reflect the changes. Further, because the use-dependence simulation is computationally exhaustive, rerunning of the simulation can be disabled to more quickly achieve a better fit for spiking (A) and calcium voltage clamp (D), then the simulation

can be re-enabled to ensure the new parameter set satisfies a visual comparison to use-dependence experiments. Using panels C and F, the user can manually change parameters using different interfaces (see Figures 2.16 and 2.17), while the Genetic Algorithm button (E) runs MATLAB's *ga.m* from the Optimization Tool Box. A secondary GUI screen allows the user to choose which parameters will be altered through the genetic algorithm (Figure 2.18). Most of the parameters in the system are available for manipulation in the genetic algorithm interface, including the maximum conductances and channel kinetics for all channels, use-dependence terms, and global terms like capacitance and applied current. Once the genetic algorithm is done optimizing about the chosen parameters, the result is implemented and all the windows are updated so that the user can immediately see the results of the new parameter set, and analyze its performance on the different tests.

The features combined in one one screen give the user a lot of efficient control, combining both manual and automatic fitting procedures to optimize time spent exploring parameter space.

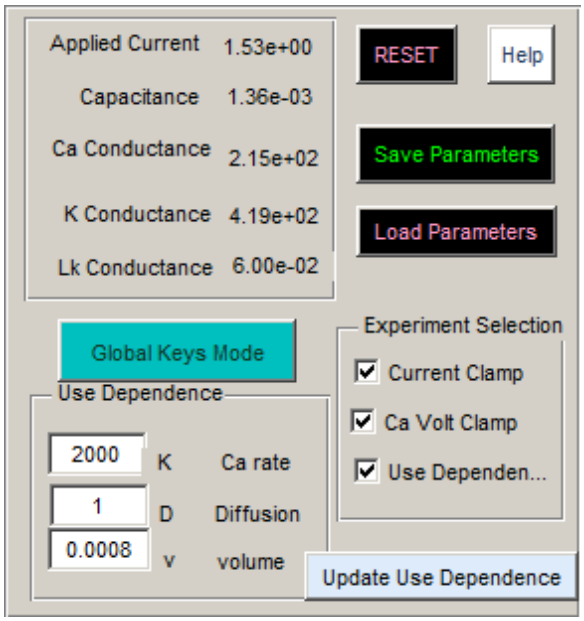

Figure 2.16: GUI master control panel. "Global Keys Mode" button allows key press manipulation of the parameters listed above it, updating the parameters and plotting the output with each key press. The "Use Dependence" panel allows direct entry of diffusion parameters, RESET resets to default parameters (hard coded in GUI code), the SAVE and LOAD functions allow parameters to be saved while exploring the parameter space, and loaded later. "Experiment selection" allows user to select which tests make it to the visual output. This allows time to be saved, particularly when using "Global Keys Mode" it is helpful to exclude (uncheck) "Use Dependence" to skip the use-dependence test to avoid long wait times. "Update Use Dependence" runs all selected simulations again and plots the new outputs (Figure 2.15, A, B, and D).

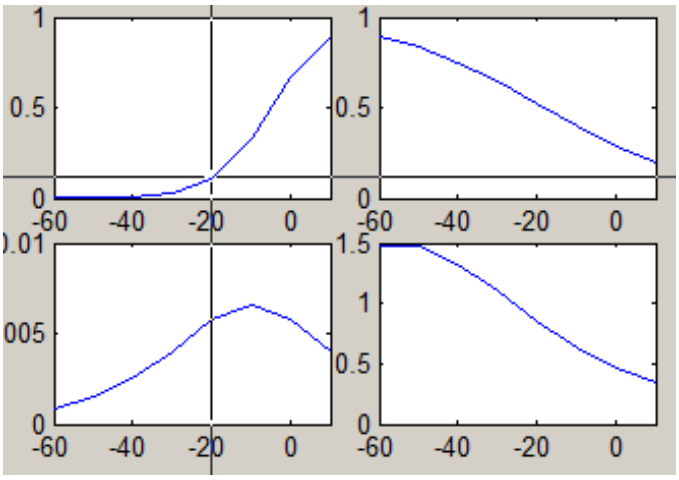

Figure 2.17: GUI kinetic manipulation. The kinetics for each channel can be selected and changed visually, using MATLAB's *ginput* function to choose points. This allows for a quick changes to be made based on intuition about the currents. The user chooses: three points for *activation* (top left), with the first two points lying on the activation curve and the third, the maximum conductance; three points for *activation time constant* (bottom left), with the first two points lying on the curve and the third, the maximum time constant. If inactivation is selected, two points are required for the *inactivation* curve (top right) and three points, as before, for the *inactivation time constant*. Once points are chosen, the new kinetics are plotted, the selected tests are run, and their corresponding outputs are redrawn in GUI outputs (Figure 2.15 A,B, and D).

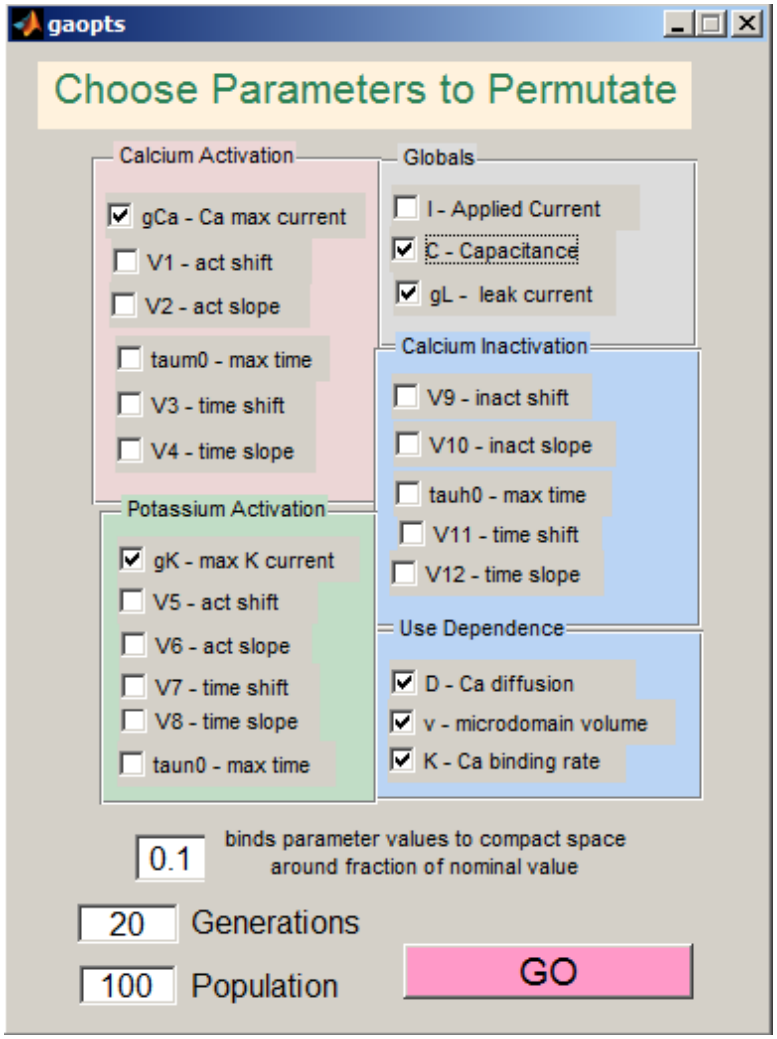

Figure 2.18: GUI Genetic Algorithm options panel. Once manual tweaking through the main control panel (Figure 2.16) is close enough, user can use a genetic algorithm with a least-squares fit between experiment and model as the test. Additionally, the user can choose which parameters to allow the genetic algorithm to work on. In the above example, non-measurable parameters are perturbed 10% around the nominal values provided by the main GUI output. Once the genetic algorithm completes running (when it has reached the number of GENERATIONS designated) the simulations are repeated and the output plotted (Figure 2.15 A,B, and D)

2.1.4 Nonselective channels

With the basal currents modeled, the nonselective channels and enhanced calcium current can be implemented in the bag cell in order to replicate experimental observations. In the biological cell, depolarization of the membrane potential is observed following a 5Hz, 10 s long stimulus to the bag cell neuron. The depolarization appears to be initiated by nonselective voltage-independent channels at its onset, but is later thought to be dominated by a PKC-enhanced calcium current related to calcium channel recruitment in the membrane [31] as well as persistent activation of calcium [50].

Both cation channels require a *delayed calcium* variable for the model to have a delayed response from the end of stimulus to the beginning of afterdischarge, as is typically observed *in vitro* [50]. The delay is a simplification and could represent either internal processes, such as internal calcium release via 2nd messenger signaling or calmodulin-facilitated kinetics in the nonselective cation channels. It appears in the final model (Appendix A) as

$$\dot{r} = \frac{r - s}{\tau_r} \tag{2.10}$$

where s is the previously established calcium concentration at the internal domain. The time constant. A convenient constant value is chosen for τ_r (see AppendixA) such that it produces a delay prior to onset of afterdischarge.

Voltage-independent nonselective channels have a reversal potential of -45 mV and appear to activate and inactivate depending on internal Ca^{2+} concentration [50]. Thus, they can be modeled

$$I_{CATvi} = g_{CATvi}\theta\phi(V + 45) \tag{2.11}$$

$$\dot{\theta} = \frac{\theta_{ss} - \theta}{\tau_\theta} \tag{2.12}$$

$$\dot{\phi} = \frac{\phi_{ss} - \phi}{\tau_\phi} \tag{2.13}$$

where

$$\theta_{ss} = \frac{1}{2}\left(1 + \tanh\frac{Ca_i - Ca_3}{Ca_4}\right) \tag{2.14}$$

$$\phi_{ss} = \frac{1}{2}\left(1 + \tanh\frac{Ca_i - Ca_5}{Ca_6}\right), \tag{2.15}$$

in which the nonselective, voltage-independent current, I_{CATvi} is computed with the conductance, g_{CATvi}, activation θ, inactivation ϕ, and the driving force, $V+45$. The activation functions follow the modern formulation of the Hodgkin Huxley model, but the functions are dependent on the delayed internal Ca^{2+} concentration, r, rather than the membrane

potential, V. Note that the driving force, $(V + 45)$ is still dependent on membrane potential. The time constant functions, τ_θ and τ_ϕ do not have functions associated with them, but are treated as constants.

Similar to the voltage-independent nonselective channels, the *voltage-dependent* nonselective channels also have a Ca^{2+} dependence. That dependence has been quantified in experimental literature, along with measurements of the reversal potential ($V_{vdp} = 10mV$) [69]. Because the data in the published work is normalized, the unnormalized data was provide by experimental collaborators and a fit was performed. Because the channel functions as a voltage-gated channel and more data points are available for voltage-dependence, the channel is treated as voltage-dependent with calcium-dependent modulation. That is, the half-activation and slope constants of the voltage-dependent terms are dependent on Ca^{2+} such that

$$V_1 = V_{i1} + V_{i2}\frac{1}{2}\left(1 + \tanh\frac{Ca_i - Ca_7}{Ca_8}\right) \tag{2.16}$$

$$V_2 = V_{j1} + V_{j2}\frac{1}{2}\left(1 + \tanh\frac{Ca_i - Ca_9}{Ca_{10}}\right), \tag{2.17}$$

where $Ca_7 - Ca_{10}$ are the usual activation-like Ca^{2+} parameters. Calcium influx modulates the voltage-dependent half activation, V_1, between the values of V_{i1} and V_{i2}. The analogous is true for the slope, V_2, and its bounds, V_{j1} and V_{j2}. There is no inactivation term for the voltage-dependent channels, thus the current is modeled as

$$I_{CATvd} = g_{CATvd}\eta(V - 10) \tag{2.18}$$

$$\dot{\eta} = \frac{\eta_{ss} - \eta}{\tau_\eta}, \tag{2.19}$$

where

$$\eta_{ss} = \frac{1}{2}\left(1 + \tanh\frac{V - V_1(Ca_i)}{V_2(Ca_i)}\right). \tag{2.20}$$

and $\tau_\eta = \tau_{\eta 0}$ is a constant rather than a function.

The final form of both channels and their associated parameters are included in Appendix A.

2.2 Prototype *Aplysia* bag cell neuron model

Using the modular pieces developed thus far, the full bag cell neuron model was developed into 10 differential equations with nonlinear interdependencies. The system exhibits many different behaviors depending on parameter choice. Using the parameters established thus far throughout the methodology, the system is manually tuned to meet three criteria. The model must:

1. Sit at rest potential (≈ -55 mV) when zero current is applied at nominal values of calcium concentration, s.
2. Show tonic spiking for positive applied currents.
3. Display persistence after cessation of the command current (5 Hz frequency pulse, with 150 ms pulse width, 10 s duration, and 1.4 nA amplitude). The cell must continue to spike when external current is no longer being applied.

Properties like wave shape and current contribution require finer analysis, which will be handled later. Given the enormous complexity of the system coupled with a limited data set, a system that produces the desired qualitative results becomes a good baseline for continuation analysis. Qualitative changes to the system are often accompanied by *fixed points* in the dynamical system that can be found with numerical analysis, an approach which is much faster, computationally, than simulation analysis.

Starting with the results from the synthesis section (2.1.3), the voltage-dependent and voltage-independent nonselective cation channels were added to the system (section 2.1.4), along with calcium-dependent enhancement of the calcium channels (Equation 2.6). Using the knowledge of parameter roles gained from all prior experience in ion-channel modeling, parameter-tuning was performed manually and piece-wise as each component was added until a set of parameters were found (Tables A.1-A.4 in Appendix A) that allowed the system to meet the three criteria given above (Figures 2.19-2.27). The full *Aplysia* bag cell model is given in Appendix A.

Most steady state functions (e.g. m_{ss}) and time constant functions (e.g. τ_m) are of the standard form (Equations 1.4 and 1.22) with shifts labeled by odd-valued subscripts ($V_1, V_3, ...$) and slope labeled by even-valued subscripts (V_2, V_4). The exceptions are ϕ, θ, and η. For the voltage-independent cation channels, the steady state functions for the gating variables ϕ_{ss} and θ_{ss} are calcium-dependent, rather than voltage dependent. For η, there are two dependencies, such that $\eta_{ss} = \eta_{ss}(V, r)$ expressed

$$\eta_{ss}(r, V) = \frac{1}{2}\left(1 + \tanh\frac{V - V_{13}(r)}{V_{14}(r)}\right) \tag{2.21}$$

$$V_{13}(r) = 80 + 44.8\left[\frac{1}{2}\left(1 + \tanh\frac{r - Ca_1}{Ca_2}\right)\right] \tag{2.22}$$

$$V_{14}(r) = 51 + 28\left[\frac{1}{2}\left(1 + \tanh\frac{r - Ca_3}{Ca_4}\right)\right] \tag{2.23}$$

The numerical values for V_{13} and V_{14} were chosen from unnormalized data provided by the Magoski lab. The associated published literature contains normalized figures of the voltage-dependent nonselective cation channels [50]. Parameter values that successfully met the primary three model requirements are listed in Tables A.1-A.4

2.2.1 Prototype *Aplysia* model behavior

The prototype *Aplysia* model (Appendix A) demonstrates all three criteria for qualitative representation of afterdischarge in the *Aplysia* bag cell neuron. When no external current is applied, the membrane potential holds around -55 mV, while calcium and potassium channels drive tonic firing in the model cell (Figure 2.19). Wave shape is similar in shape to experimental results, but broader and taller, reaching more extreme limits of depolarization and hyperpolarization. The potassium current over the course of a spike is two or three times that of the calcium current (Figure 2.20, top). Early in the spike train, voltage-independent cation channels have little contribution as calcium and potassium channels carry the action potential. Leaky channels carry the largest current, with some small contribution from voltage-dependent channels (Figure 2.20, middle). Most of the currents work against calcium, with the exception of the voltage-dependent channels, which contribute to repolarization shortly after the spike. Finally, during the course of the 1.0 s current clamp, calcium concentration in the microdomain steps up with each spike, while the calcium delay slowly rises to match (Figure 2.20, bottom).

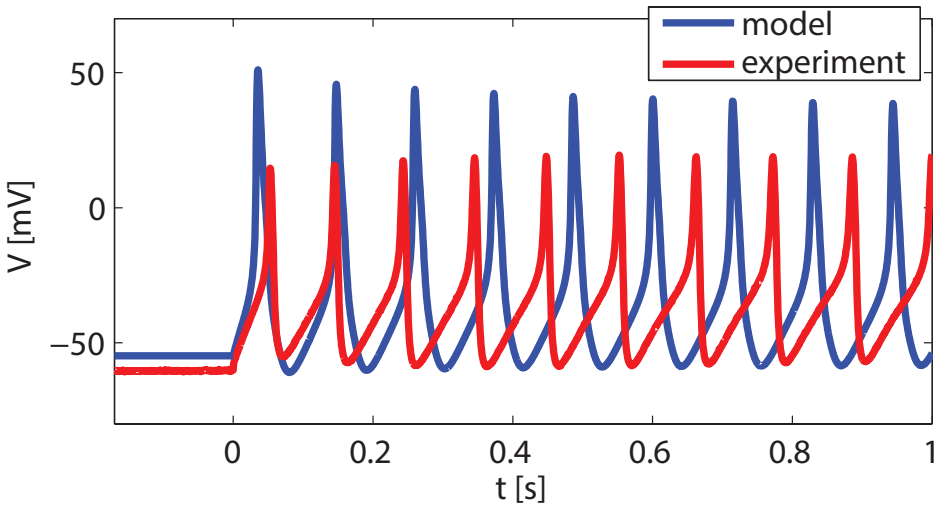

Figure 2.19: A profile of the action potential during *current clamp* ($I = 0$ nA, followed by $I = 1.4$ nA starting at $t = 0$) in the whole cell model. Data provided by experimental collaborators.

When the 5 Hz, 10 s command current (oscillating from 0.0 to 1.4 nA with a 150 ms duration) is applied to the bag cell model, it produces a similar action potential, but recovery between spikes is much slower (Figure 2.21). The current profiles don't diverge much from standard current clamp. However, calcium influx has a slower average rise compared to current clamp (Figure 2.22).

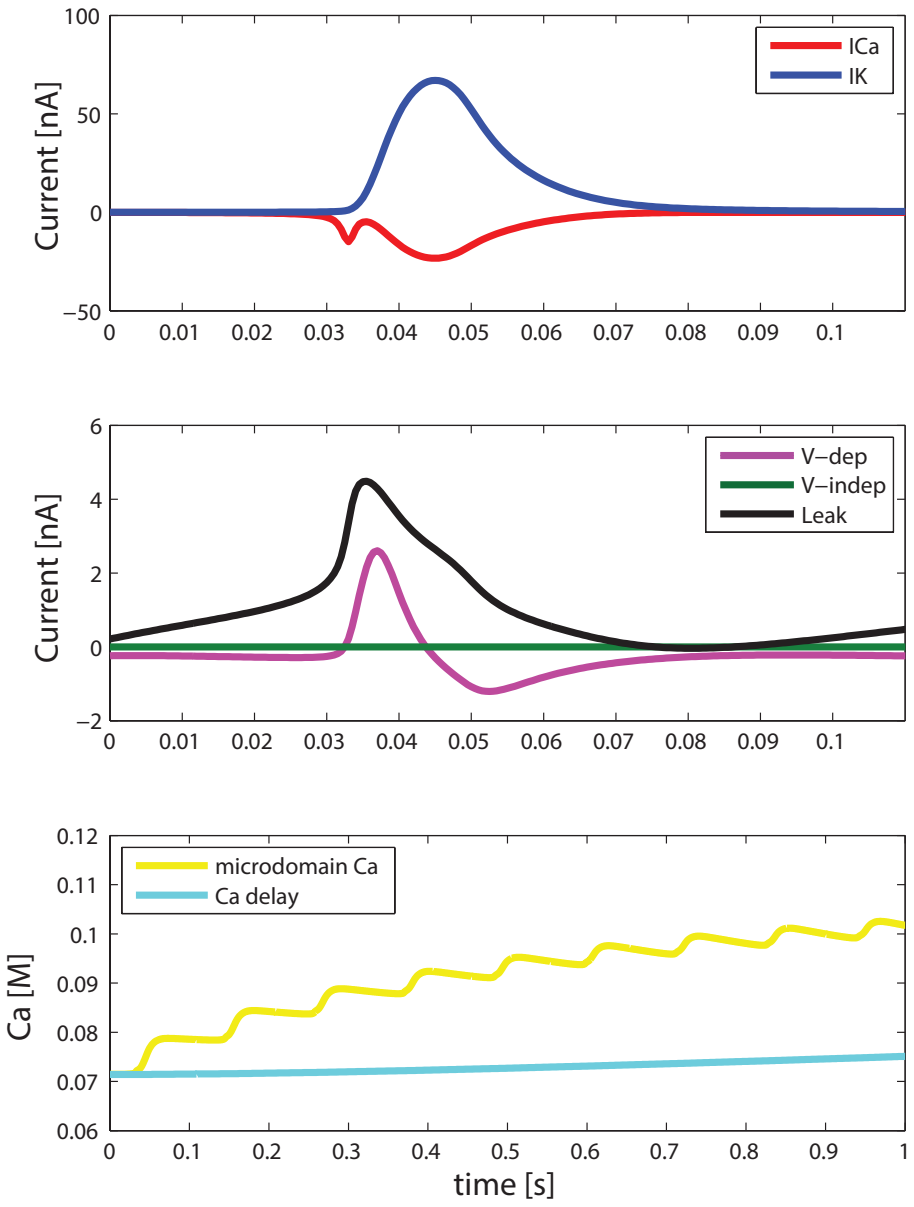

Figure 2.20: A profile of the individual currents, calcium concentration, and calcium delay term during *current clamp* ($I = 0$ nA, followed by $I = 1.4$ nA) in the whole cell model. Note that current profiles (top and middle) are given for a single spike from the onset of Figure 2.19, while the calcium profile (bottom) includes the entire duration.

The prototype *Aplysia* bag cell model demonstrates afterdischarge behavior. After 10 s of the 5 Hz command current, the external current is removed ($I = 0$ nA). At this point, the membrane depolarizes to around -45 mV followed by immediate persistent spiking (Figure 2.23). Looking at the current profile reveals that the command current raises the calcium concentration in the internal domain (Figure 2.24, bottom). The delay term slowly catches up, activating both voltage-independent and voltage-dependent nonselective cation channels (Figure 2.24 middle). By the time the external current is removed, sufficient

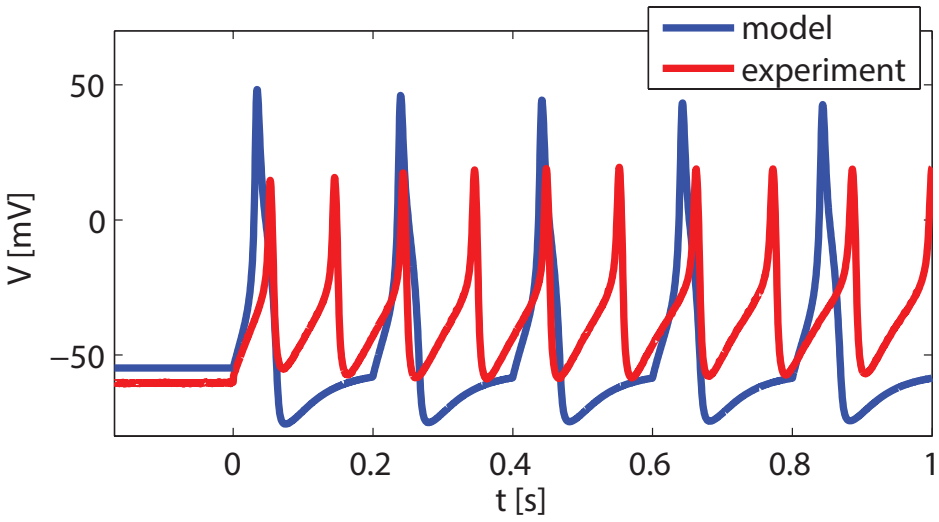

Figure 2.21: A profile of the action potential for the model cell (blue) during onset of alternating 5 Hz *command current* ($0nA < I < 1.4nA$) with a 150 ms duration. Experimental data for standard current clamp included for comparison (red).

calcium is present for calcium current enhancement (as governed by G in Eq. A.16). As the afterdischarge continues, the frequency of firing gradually declines (Figure 2.24, top) until the currents reach a stable peak to peak period of 900 ms (Figure 2.25).

A preliminary test showed that afterdischarge did not occur if either voltage-dependent nonselective channels were removed or calcium enhancement was removed. Removing voltage-independent channels only lowered the frequency of the afterdischarge. However, the system is highly sensitive and this picture could change under slightly different parameters for calcium or potassium kinetics. Additionally, because the reversal potentials of the nonselective channels lie between the calcium and potassium resting potentials, too large of a conductance drives trajectories to their reversal potentials, damping any oscillations. For the depolarization to occur in the delayed manner observed in experiments after the 5 Hz stimulus, a calcium delay term was required indicating a second-messenger system may play a role, responding to changes in calcium levels with a delay.

At the transition between the membrane's command response and afterdischarge, when voltage-independent channels are fully activated, there is a repolarization to about -45 mV before the onset of afterdischarge (Figure 2.26).

Under command current, the model bag cell spiked at 5 Hz, dropping to 2.3 Hz during afterdischarge. The membrane potential amplitude is similar for both command response and afterdischarge. This is in contrast to experimental observations, which show taller peaks during afterdischarge. The current profile does demonstrate an increase in potassium and calcium current from command to afterdischarge (Figure 2.27), which suggest that some fine tuning of current contribution may be necessary to ensure membrane potential isn't over saturated by the leak or modulating currents. The calcium concentration at the microdomain drops to a slightly lower steady state at the onset of afterdischarge.

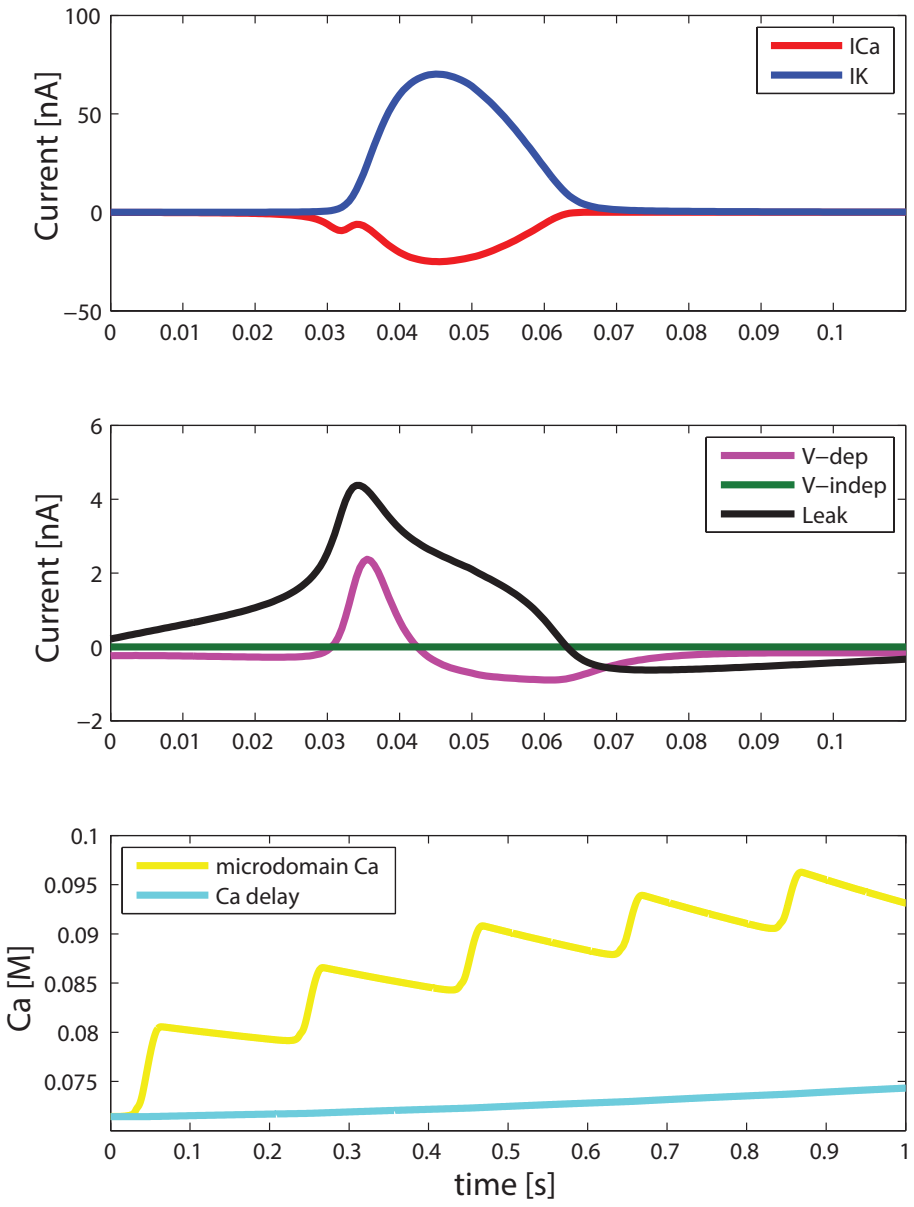

Figure 2.22: A profile of the currents and calcium concentration for the model cell during onset of alternating 5 Hz *command current* (0 nA $< I <$ 1.4 nA) with a 150 ms duration.

2.2.2 Conclusions

The prototypical *Aplysia* bag cell neuron meets the three criteria for a qualitative reproduction of the onset of afterdischarge in the natural cell. Many values were derived from fits on experimental data from the Magoski lab. In particular, the calcium activation kinetics and mixed (two-current) potassium kinetics, as well as reversal potentials for all currents. Activation kinetics for the voltage-dependent nonselective cation channels were also provided. Calcium inactivation, and all components of the potassium current, have at least two dependencies in them. As a result, there is no unique solution to fitting paradigms without

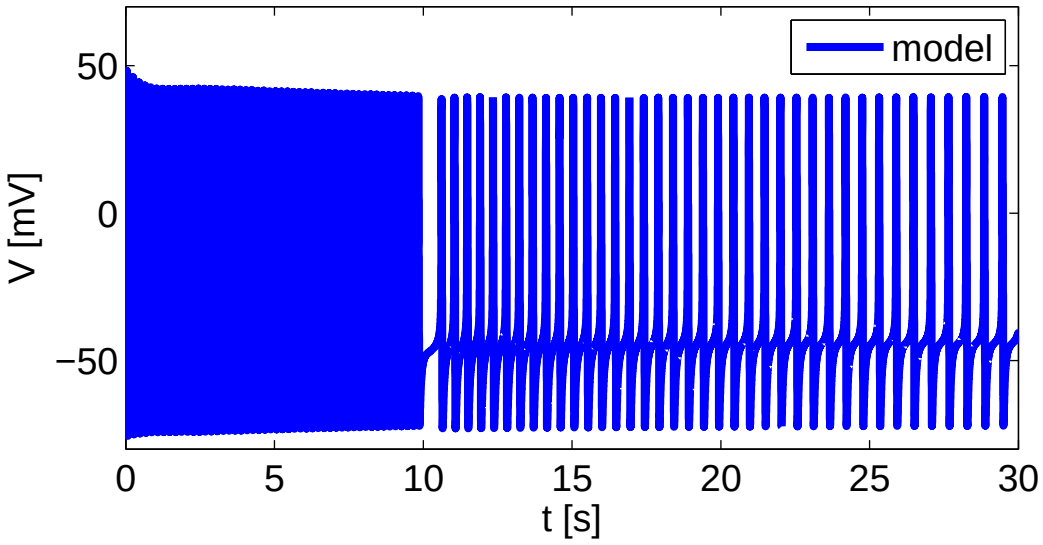

Figure 2.23: The action potential during afterdischarge: 10s of the command current (See Figure 2.22 for details) followed by zero input current. See Figure 2.26 for close a closer look at the spikes.

some reasoned constraints. To address this, inactivation was split evenly between calcium-dependent and voltage-dependent inactivation, then tuned until it matched activation (as discussed in the calcium channel section). Similarly, because no unique solution exists for a combination of two inseparable currents, an experimental potassium profile was found that allowed the currents to be treated as one single, equivalent current. The cell from which this data was taken also demonstrated spiking in current clamp, though the spiking wasn't sustained (Figure 2.12).

To address these problems, the next chapter will turn to numerical continuation for analysis of the system's fixed points and limit cycles. A handful of the 55 parameters will be perturbed to observe their effect on the properties of these mathematical objects, which can inform how the system will behave in different regions of parameter space without numerous tedious simulations.

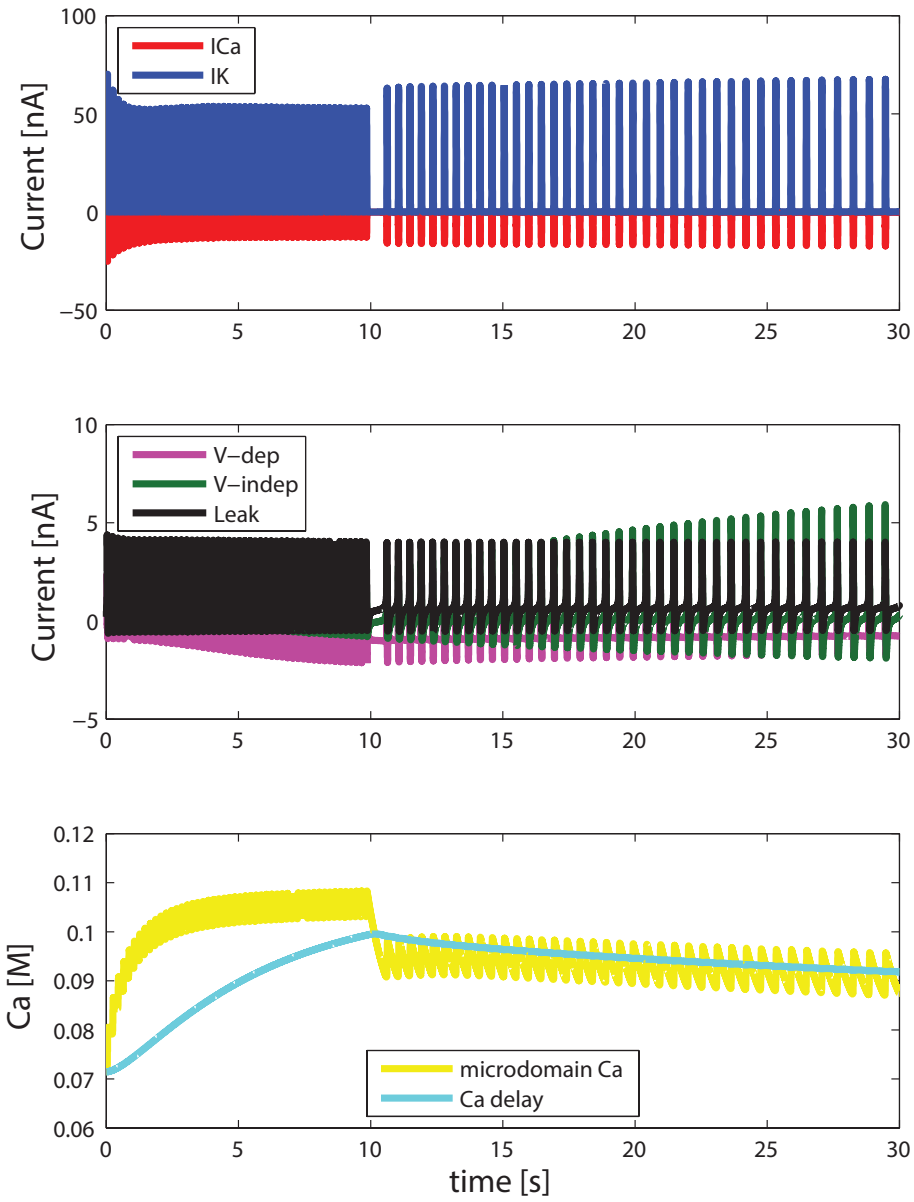

Figure 2.24: Current underlying the action potential during afterdischarge simulation (See Figure 2.23 for details).

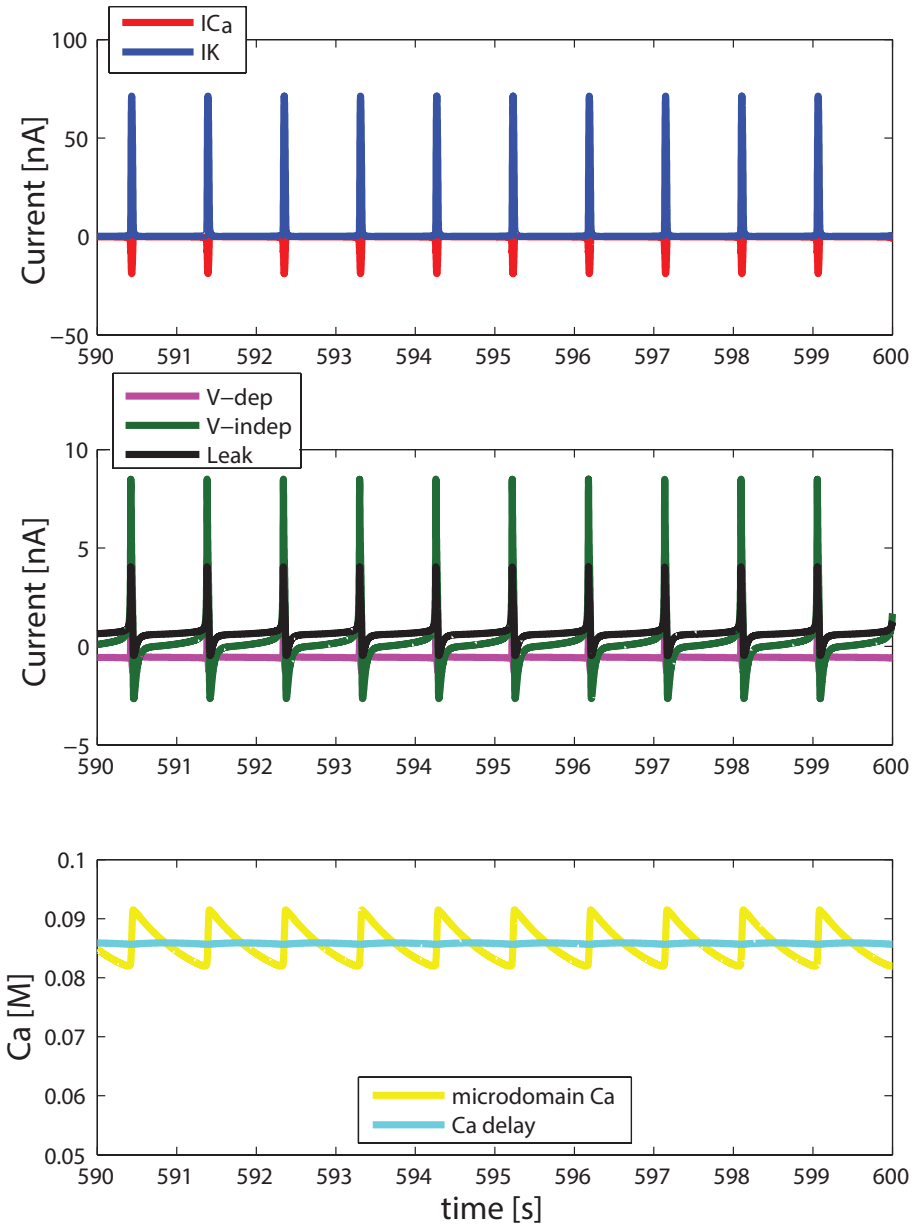

Figure 2.25: The current profile after 10 minutes of afterdischarge demonstrates a stable 900 ms duration between peaks.

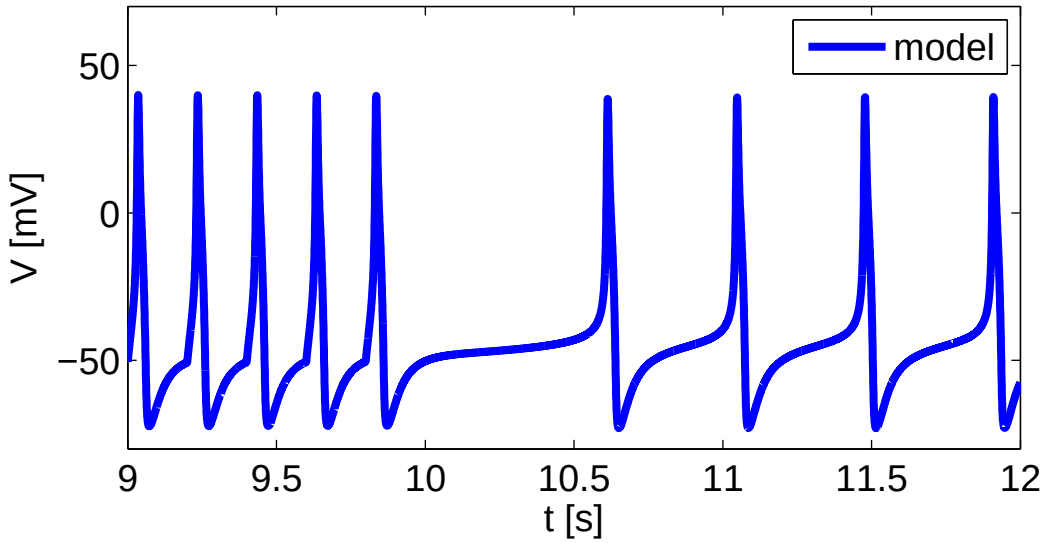

Figure 2.26: The membrane potential transitioning from external current drive to persistent spiking as $I = 0$ nA at 10 s.

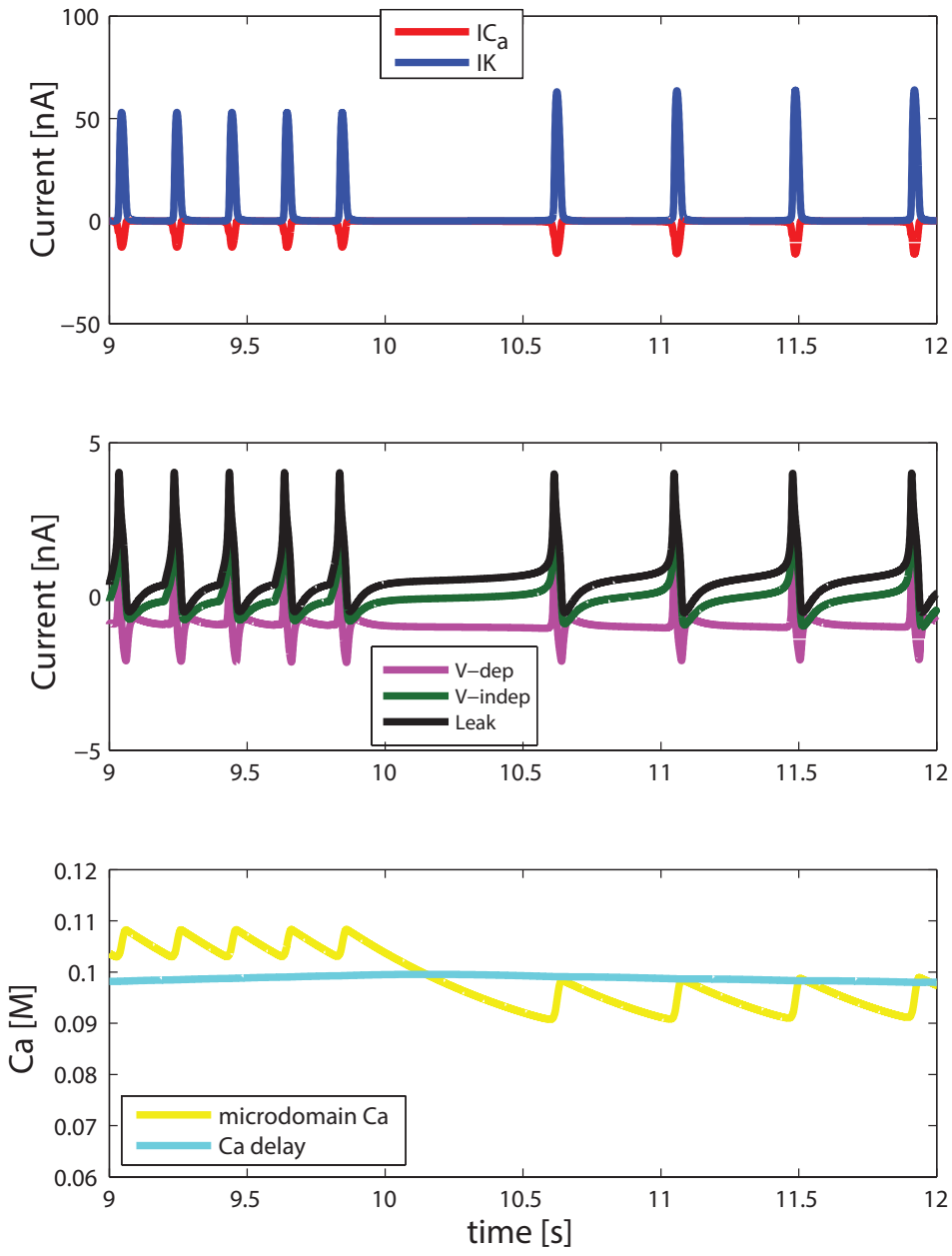

Figure 2.27: Corresponding currents and calcium concentration for Figure 2.26.

Chapter 3

Model parameter analysis: continuation curves and sensitivity

Given the complex construction of the *Aplysia* bag cell neuron model and the 55 parameters involved across numerous time scales (from milliseconds to minutes), it is of interest to analyze how parameters affect the core behavior of the system. The continuation curve of the prototype *Aplysia* bag cell neuron is computed across multiple values of different parameters and guided by eigenvalue analysis. The insights gained from continuation analysis allowed for finer tuning of the model to better match experimental observations. A follow-up exploratory analysis examines how the continuation curve and associated Hopf points are affected by parameter value changes. These insights can help guide tuning and modifications to the model.

Continuation curves follow fixed points in the system as parameters evolve. In the case of neural models where there is a designated external input parameter, I, fixed points are analyzed as a function of I. Thus, in a continuation context, the applied current, I, is the *bifurcation parameter*. Along the continuation curve, and often associated with dynamical transitions in the system, are *bifurcation points*. In the case of the prototype *Aplysia* bag cell, the bifurcations will be *Hopf bifurcations*, in which the system transitions from steady-state behavior to oscillatory behavior, with the amplitudes of the oscillation either growing to some finite point or decaying from some finite point as the bifurcation parameter is increased. Examples follow.

3.1 Model tuning with continuation

Continuation analysis of the prototype *Aplysia* bag cell is performed using the applied current, I, as the control parameter. At each value of I, the softwasre analyzes where the equilibrium points are. The resulting set of points is plotted (Figure 3.1). A Hopf point (H3) occurs around $I = 15$ nA, and a set of two Hopf points (H1 and H2) occurs near $I = 0$ nA.

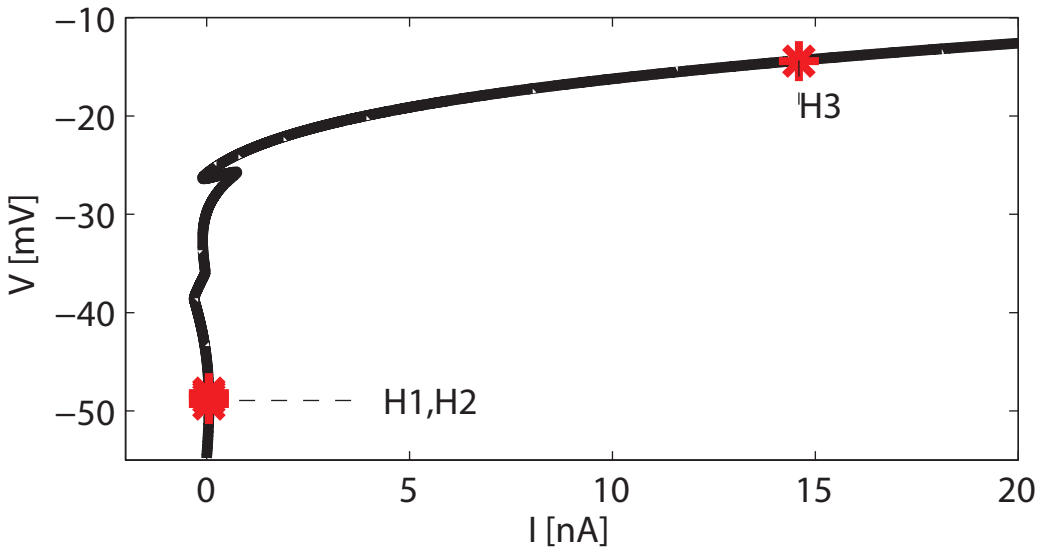

Figure 3.1: Continuation curve (black line) for the *Aplysia* prototype model with Hopf points (red asterisk). A horizontal expansion of the curve (inset) shows a complex arrangement of Hopf points. Hopf points H1, H2, and H3 have limit cycles associated with them.

The true Hopf points were associated with limit cycles. The outlier Hopf point (at $I = 15$ nA) is the source of the largest limit cycle in the range. The limit cycle begins with small amplitudes at the Hopf point and grows larger as $I \to 0$ nA (Figure 3.2). Near zero, the amplitude of the limit cycle is more stable and the continuation curve contains many Hopf points and limit points (Figure 3.2). It can also be observed that the limit cycle goes right up to (and even passes) $I = 0$ nA.

A very small amplitude limit cycle connects Hopf points H1 and H2 around the point (I, V) =(.055 nA, -48 mV). Its largest amplitude is 2 mV about $V = -48.3$ mV. It's unclear whether these Hopf points play a role in dynamics, as they occur concurrently with several limit points. It is in this region that the simulated system transitions from steady state to periodic behavior. This may imply that H1 and H2 play a role in that transition, as the limit cycle originating from H3 still exists in the region $I < .054$ nA, but spiking behavior does not.

In the physiological system, spiking behavior is eliminated when the external current exceeds 2 nA. In the model system, continuation reveals a limit cycle existing up to 15 nA, inconsistent with the physiology. To address this, the eigenvalues and eigenvectors of H3 are examined. When a pair of eigenvalues have a real part that is approximately zero and their associated eigenvectors are complex conjugates of each other, the eigenvector can sometimes reveal what system variables are playing a role in the properties of the Hopf point. For H3, the relevant eigenvector pair contained projections into m, the calcium activation, and n, the potassium activation (Figure 3.5). Parameters relating to both were varied and the effect on their continuation curves observed. While the m component had the largest amplitude in the eigenvector, it was n that had the most dramatic effect on

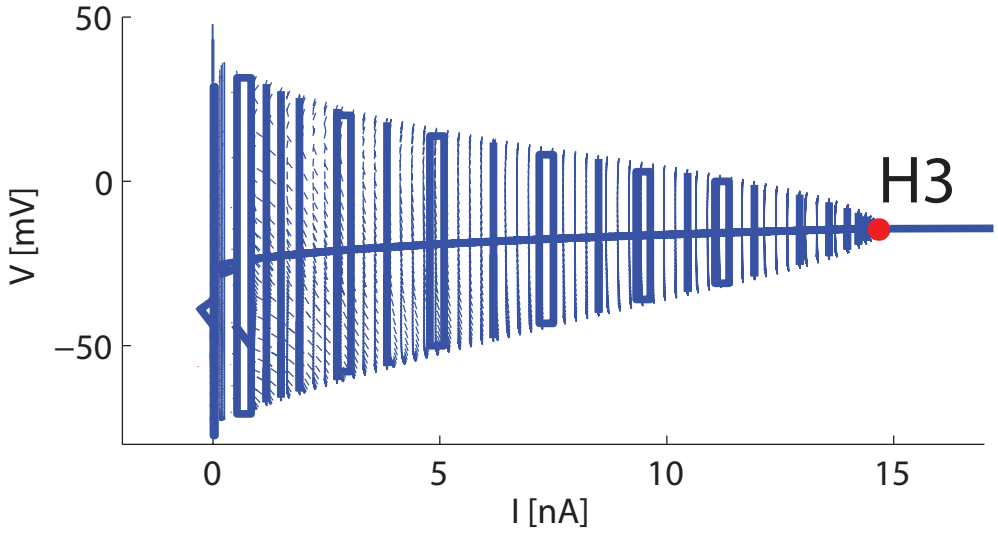

Figure 3.2: Continuation curve and limit cycle associated with H3 in the *Aplysia* bag cell neuron model. The vertical traces represent the maximum and minimum values of the membrane potential during spiking for a given value of applied current.

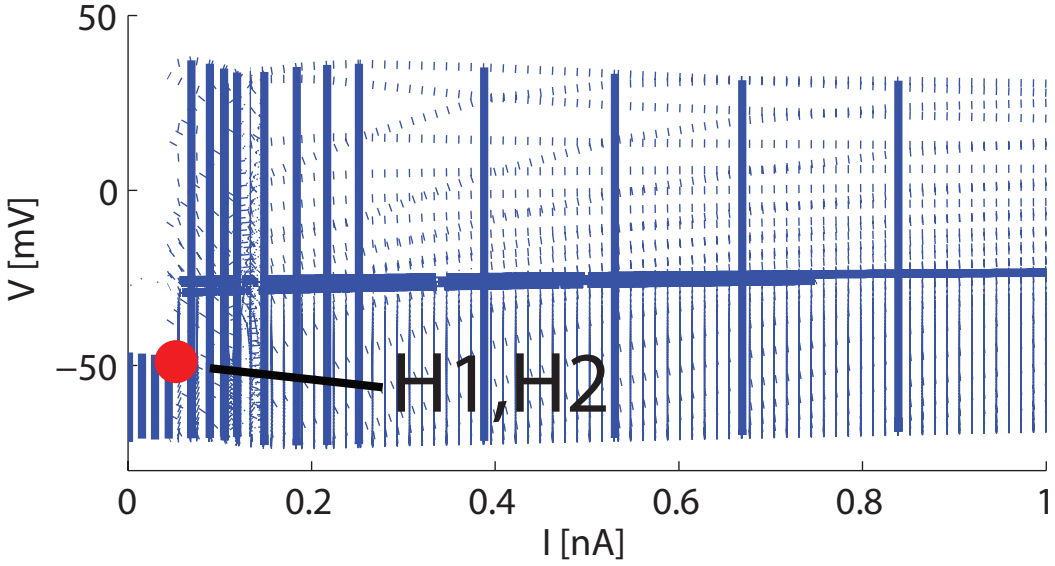

Figure 3.3: In the physiological range, the limit cycle has complex structures for $I < 0.2$ nA. The vertical traces represent the maximum and minimum values of the membrane potential during spiking for a given value of applied current.

Hopf point location.

Whereas many parameter changes will completely alter the shape of the continuation curve, disrupting the established behavior, the time constant voltage-shift, V_7, only changed the location of the Hopf point along the curve (Figure 3.6). It had the additional effect of

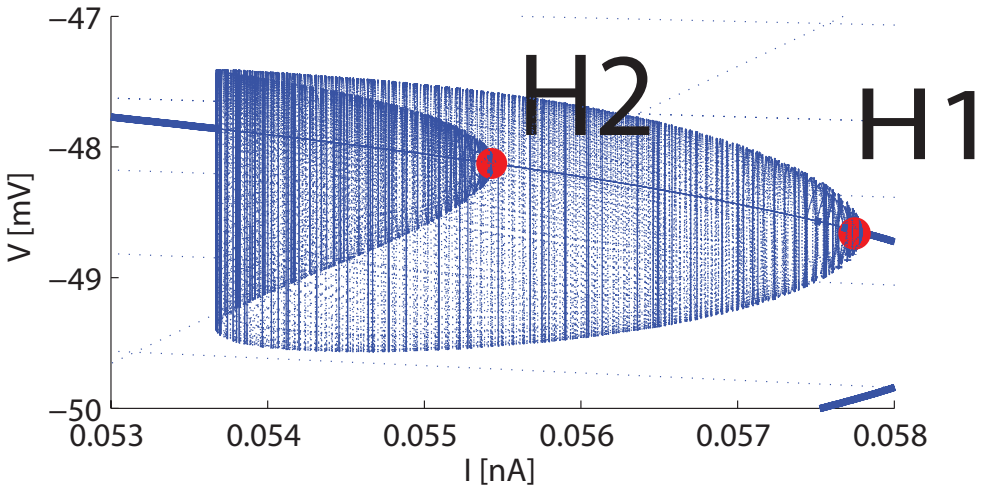

Figure 3.4: A small limit cycle structure connects Hopf points H1 and H2.

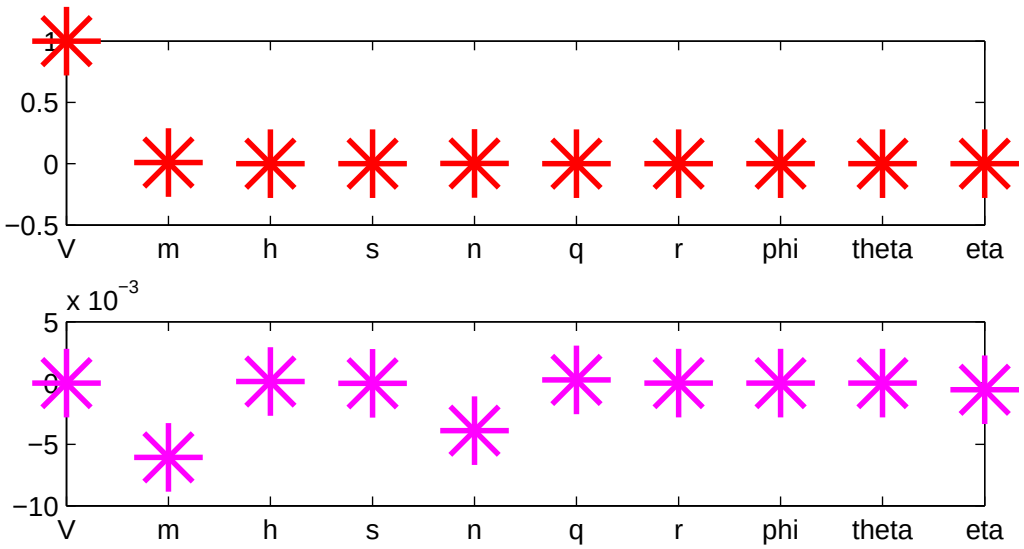

Figure 3.5: The real (top) and imaginary (bottom) parts of an eigenvector from H3 for which 1) the associated eigenvalue was approximately zero, and 2) a complex conjugate existed.

eliminating neutral saddles as H3 drew closer to $I = 0$ nA. Similar observations were made for the potassium time-constant, τ_{n0} (Figure 3.7). It's unclear why potassium activation timing parameters would have this unique effect on the bifurcation diagram. Parameters associated with the calcium activation timing yielded similar results, but to much less effect.

A value of $\tau = .02$ brought H3 down from $I = 15$ nA to $I = 4.5$ nA and greatly reduced the number of spurious neutral saddles (Figure 3.8). H1 and H2 still remain. The model still suffers gradual amplitude loss up to the new location of H3 (Figure 3.9). However,

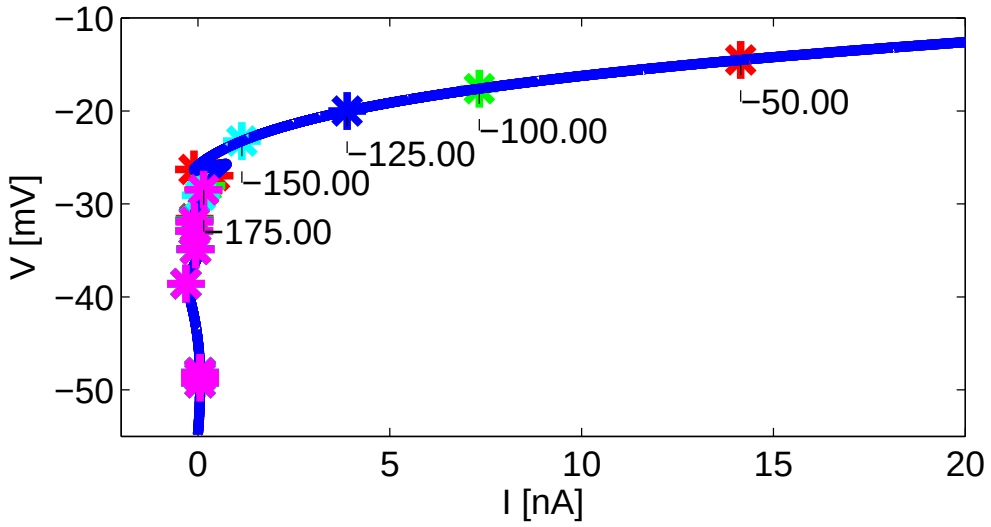

Figure 3.6: The change in location of H3 as V_7, the potassium activation time-constant voltage shift, varies. Value of V_7 for each Hopf location is labeled.

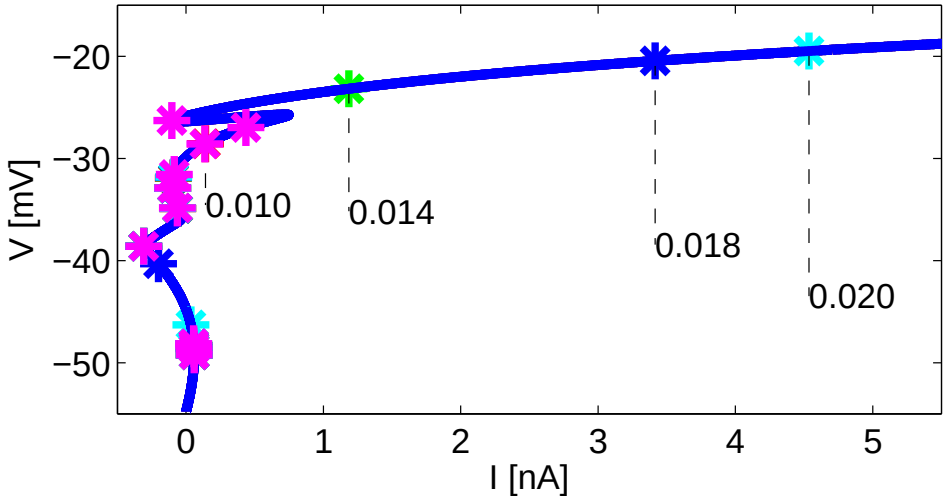

Figure 3.7: The change in location of H3 as τ_{n0}, the potassium time-constant maximum, varies. Value of τ_{n0} for each Hopf location is labeled.

the limit cycle no longer exists for values $I < .05$ nA (Figure 3.10).

These results are verified via simulation, confirming limit cycle decay and elimination at the Hopf point, and confirming that the model still meets the three criteria: no spiking at $I = 0$ nA, tonic firing for $I > 0$ nA, and afterdischarge behavior. Spike shape was preserved, and the spike minimum was lifted to match physiological data better. However, once transients from initial conditions settle, the spike maximum of the model becomes lower than those observed in biology experiments (Figure 3.9). After some hand tuning, the final value, $\tau_{n0} = 0.018$, is chosen as part of standard parameters for the modified prototype.

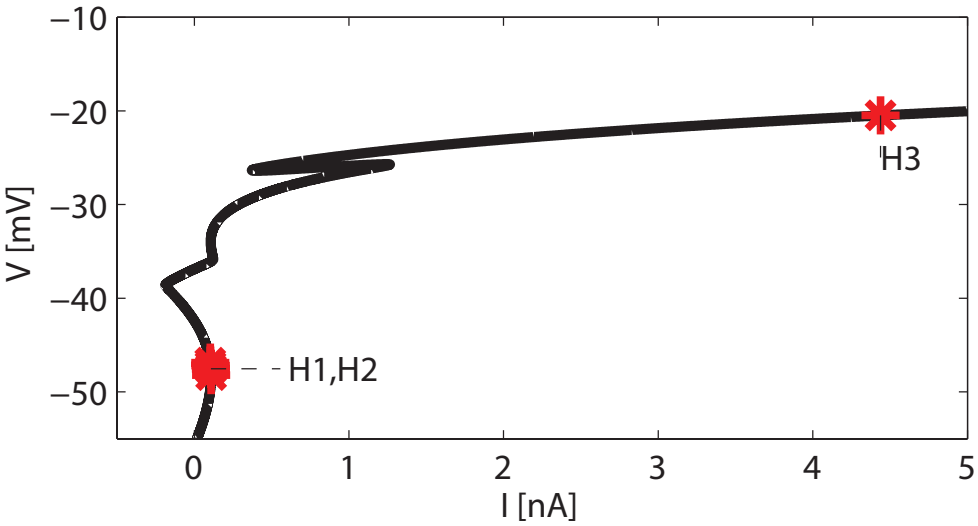

Figure 3.8: Continuation curve of the new parameter point, $\tau_{n0} = 0.018$, for the system with H3 closer to physiological ranges.

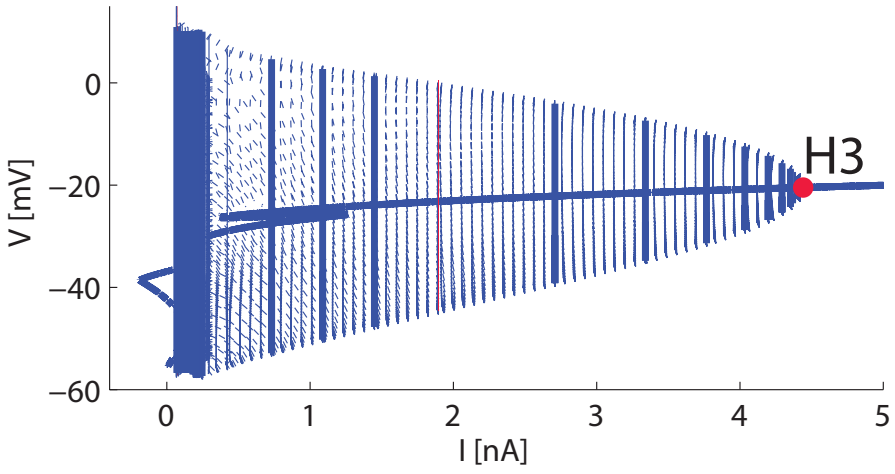

Figure 3.9: Limit cycle of the *Aplysia* model at the new parameter point, $\tau_{n0} = 0.018$.

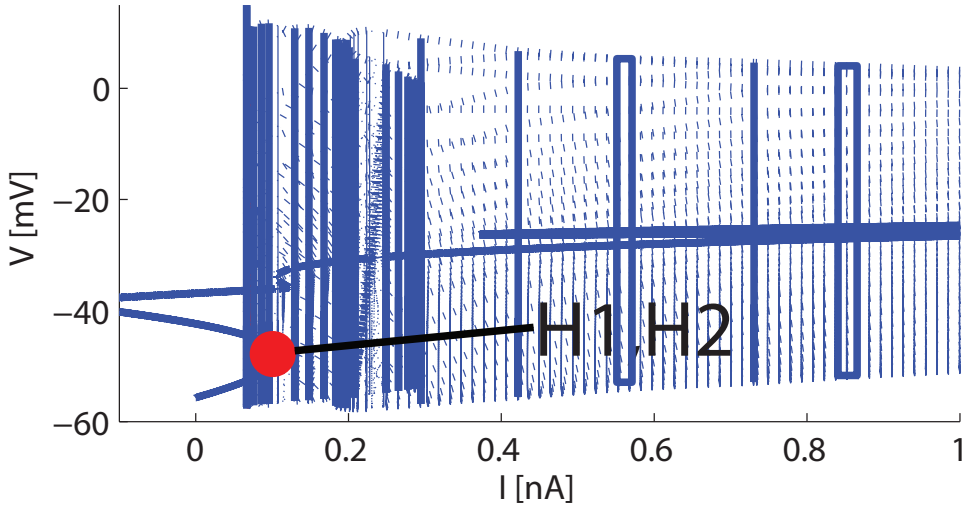

Figure 3.10: Limit cycle in the physiological range of the model at the new parameter point, $\tau_{n0} = 0.018$.

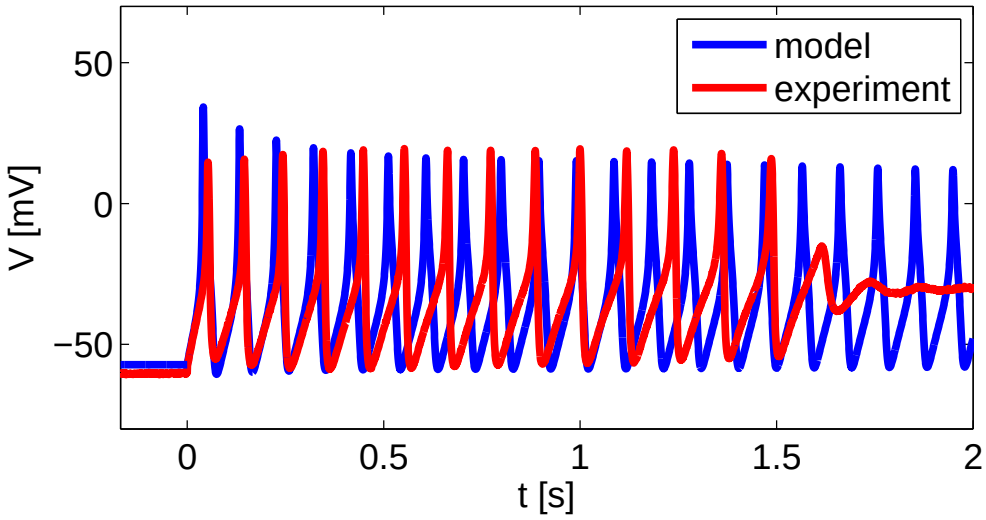

Figure 3.11: A time-series simulation of the system at its new parameter point, $\tau_{n0} = 0.018$.

3.2 Sensitivity analysis with continuation

Continuation curves reveal the location of bifurcation points that are numerically calculable, independent of simulations. In a computational context, this can often save a lot of time and resources in place of trial and error. It is therefore of interest to explore how parameter changes can can affect continuation curves and associated Hopf points to gain insights into how they might change the behavior of the system.

As before, the bifurcation parameter is the applied current, I. Continuation curves follow fixed points in the system as parameters evolve. In the case of neural models where there is a designated external input parameter, I, fixed points are analyzed as a function of I. Transitions from rest state to tonic spiking can often be associated with bifurcation points that are numerically discoverable, independent of simulations.

Using the new, established parameter point as the standard model, analysis is carried forward with the MATCONT continuation software and some additional handwritten software (wrappers) to facilitate its usage across parameters and generate graphics from the results. Distinct parameters are perturbed and their continuation curves measured. For each perturbation, a parameter or set of parameters is chosen and perturbed four times about their nominal value from 80% to 120%. This is achieved by multiplying their nominal values by p (which takes the values of $0.8, 0.9, 1.1$, and 1.2) and examining their continuation curves at each perturbation. Each of the figures are plotted with color coding such that a black line corresponds to $p = 0.8$, a red line corresponds to $p = 0.9$, the green line is the nominal system, a magenta line corresponds to $p = 1.1$, and a blue line corresponds to $p = 1.2$.

Further continuation at Hopf points examines how changes in parameter might affect the existence, amplitude, and current-dependency of the limit cycle. This analysis gives insight into not only the sensitivity of certain parameters, but some of the qualitative outcomes of changes to those parameters. Because the entire parameter set is sufficiently large, priority was given to parameters which, through the intuition gained by hand-tuning the system, were known to change the outcome in desired ways. The intuition generally follows logical conclusions. For example, parameters that can increase calcium efficacy (such as the maximum conductance and the associated kinetic parameters) will likely lead to more excitability, while augmentation of potassium will likely reduce excitability. Parameters that were found to be qualitatively sensitive through hand-tuning were investigated, such as the enhancement multiplier, mg_{Ca}. Additionally, parameters were randomly selected to ensure some coverage beyond the author's cognitive grasp, such as use-dependence.

Perturbations on the slope of the calcium activation, V_2, yielded large changes in the continuation curve (Figure 3.12). This is not particularly surprising as changes to the slope of activation curves have a significant effect on the voltage-dependence of channel currents. Since the primary calcium channel plays a significant role in the behavior of the bag cell model, changes to its activation slope will have significant consequences. As V_2 is increased, the Hopf point H3 approaches $I = 0$ nA. This would normally be desired given the experimental evidence of a saturation point at $I = 1.5$ nA. However, changes in the continuation curve either diminish or annihilate the limit cycle generated by H3 (Figure

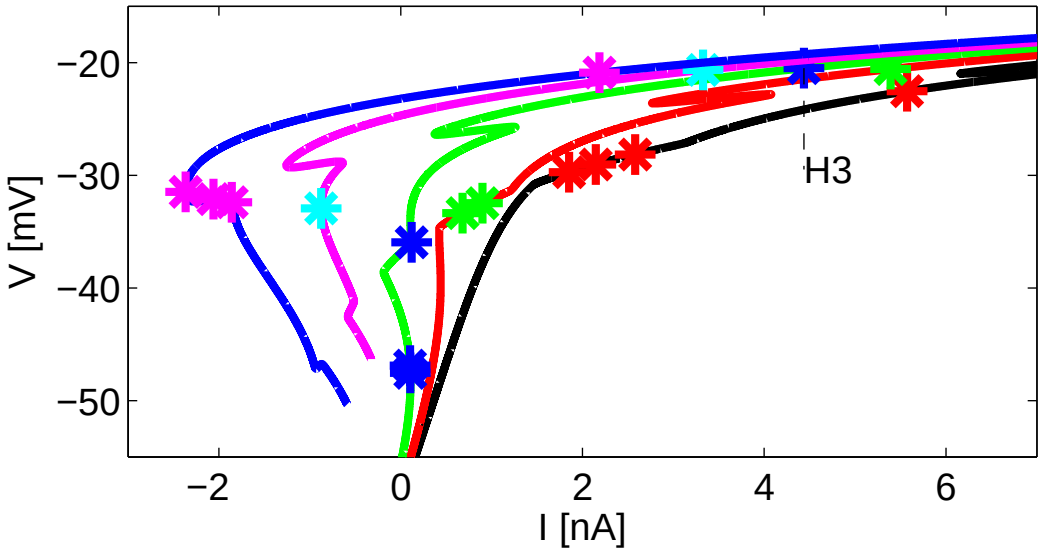

Figure 3.12: Variants of the continuation curve as V_2, the slope of calcium activation, is changed. Color of line maps [black, red, green, magneta, blue] to $p = [0.80.91.01.11.2]$, the multiplier on the nominal value.

3.13).

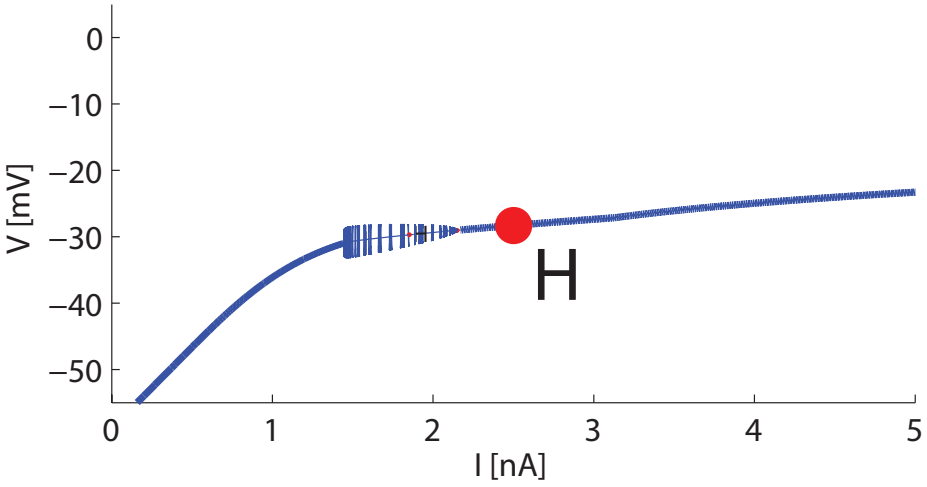

Figure 3.13: Limit cycle for $V_2 = 11.52$ mV has small amplitudes near an unidentified Hopf point, possibly H3.

When the diffusion rate is altered by the perturbation, p, little change in the continuation curve is observed (Figure 3.14). The continuation curve is lifted and shifted right slightly (Along with Hopf points H1, H2, and H3). No appreciable change in limit cycle behavior is observed. Because of the influence of diffusion on the afterdischarge, care must be taken. Since afterdischarge behavior depends on long-term changes in calcium, the effects of changing D on afterdischarge behavior is not immediately apparent from these

continuation curves, which are more informative about short-term dynamics in the system.

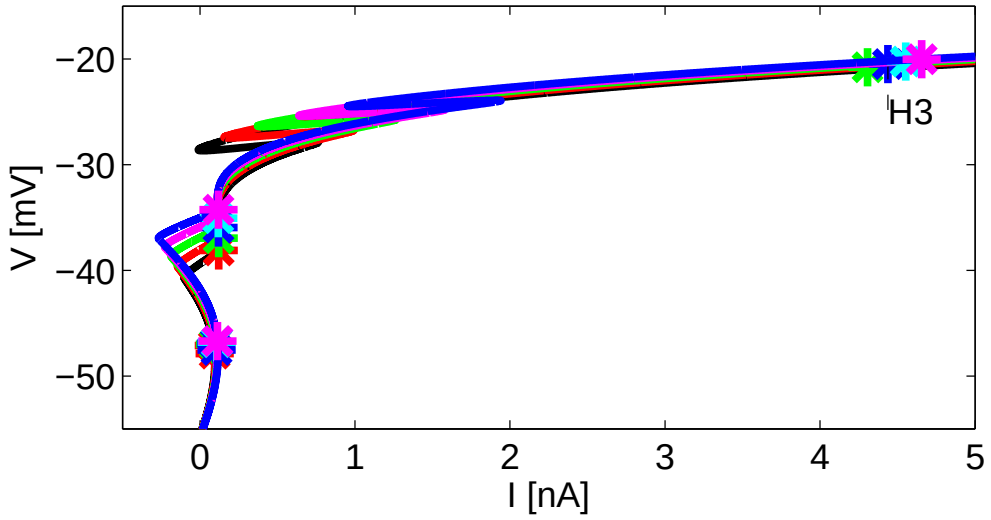

Figure 3.14: Variants of the continuation curve as D, the rate of calcium diffusion out of the domain, is changed. Color of line maps [black, red, green, magenta, blue] to $p = [0.8, 0.9, 1.0, 1.1, 1.2]$, the multiplier on the nominal value.

Observations from the simulated model demonstrate that a large D can cause calcium to escape too quickly from the system, eliminating the afterdischarge, while smaller values of D can cause oversaturation of calcium in the system, making it too excitable.

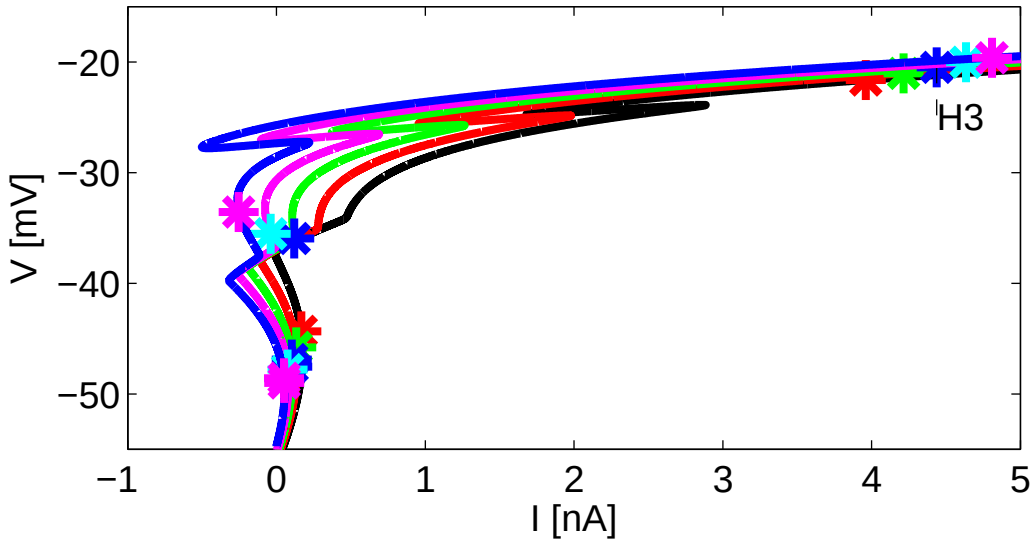

Figure 3.15: Variants of the continuation curve as mg_{Ca}, the calcium-dependent calcium conductance magnification, is changed. Color of line maps [black, red, green, magneta, blue] to $p = [0.8, 0.9, 1.0, 1.1, 1.2]$, the multiplier on the nominal value.

Calcium enhancement is modeled as a calcium-dependent magnification on the conductance of the calcium current. Not surprisingly, increasing this value raises the continuation

curve (Figure 3.15) along with the Hopf points. Additionally, for increased values of mg_{Ca} the cell becomes too excitable and the limit cycle persists for applied current values down to $I = 0$ nA (not shown). Too many calcium channels have been introduced, bringing in more calcium, which activates all the calcium-dependent channels. The resulting solution is oscillatory, as calcium serves as the primary driver of the upstroke in bag cell model oscillations.

When mg_{Ca} is decreased too much, afterdischarge behavior ceases. Thus, the continuation curve isn't able to show how changes in mg_{Ca} affect propensity for afterdischarge. Again, this is because calcium enhancement pertains to the longer-term behavior of afterdischarge, while the continuation curve is more relevant to a short-term snapshot of the dynamics. This result suggests that calcium enhancement plays a significant role in initiating the afterdischarge.

To expand on previous potassium sensitivity analysis, both V_6 and V_8, the slopes of the potassium activation and the potassium activation time constant, are perturbed by p. Both parameters are varied simultaneously in order to cover changes in both the timing and amplitude of the potassium current, as they pertain to wave shape of the action potential. Similar to calcium kinetics, the curves show a high sensitivity to changes in potassium kinetics. As the slopes are increased, the continuation curve and the associated Hopf point, H3, move downward and towards increasing values of I (Figure 3.16). Limit cycles are quickly annihilated with perturbations to the potassium parameters, as the delicate balance between calcium and potassium currents is disrupted. The sensitivity of the results to the slope of activation can be explained by its role in the model. A small change in activation slope changes dependency on membrane potential across the entire physiological range of the membrane-potential.

When the conductance of all five channels are simultaneously perturbed, the continuation curve does not vary greatly. This is perhaps unsurprising, as the balance between conductances is mostly preserved in this way. This is particularly true of the two major players, calcium and potassium. Increasing the conductance of all channels results in the continuation curve and H3 moving down and towards increasing I.

Continuation analysis is computationally expensive, especially when limit cycle continuation is involved, but it does allow broader investigations into the stability of a model that can only be achieved by sampling the system for each value of applied current, I, with simulations. Thus, continuation sacrifices some details in favor of a more general understanding of how the system behaves. Details like wave shape, and the onset of afterdischarge are not immediately available from continuation analysis, but the excitability of the cell and its saturation point, and the existence of limit cycles are all useful information that can be extracted from continuation analysis.

3.2.1 Conclusions and Discussion

The high-dimensional parameter space associated with complex models can be a difficult maze to navigate. Often, gains in model accuracy with respect to one experiment can cause losses in accuracy with respect to another experiment. Tuning the model to be consistent

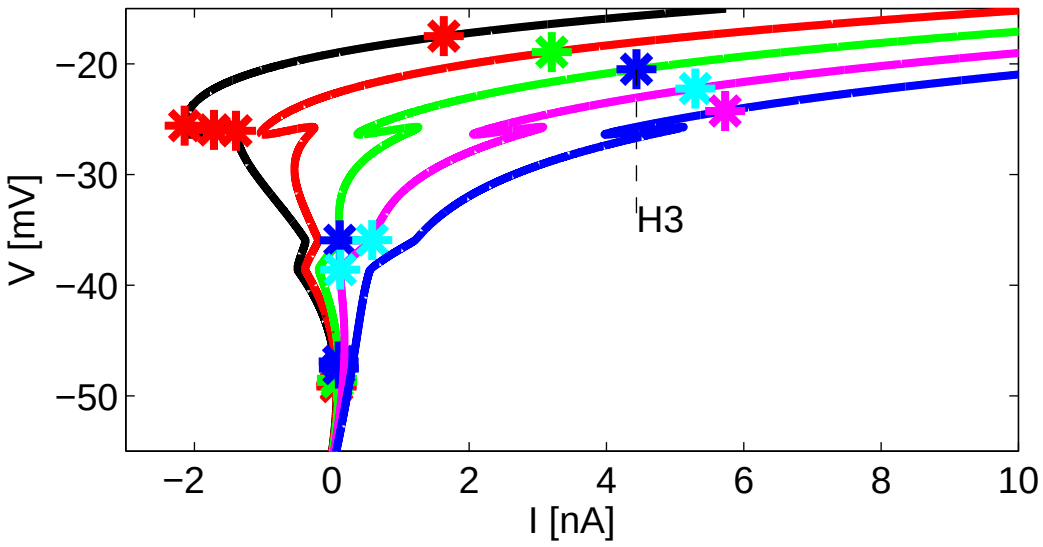

Figure 3.16: Variants of the continuation curve as V_6, the potassium activation slope, and V_8, the potassium activation time-constant slope, are simultaneously changed. Color of line maps [black, red, green, magneta, blue] to $p = [0.8, 0.9, 1.0, 1.1, 1.2]$, the multiplier on the nominal value.

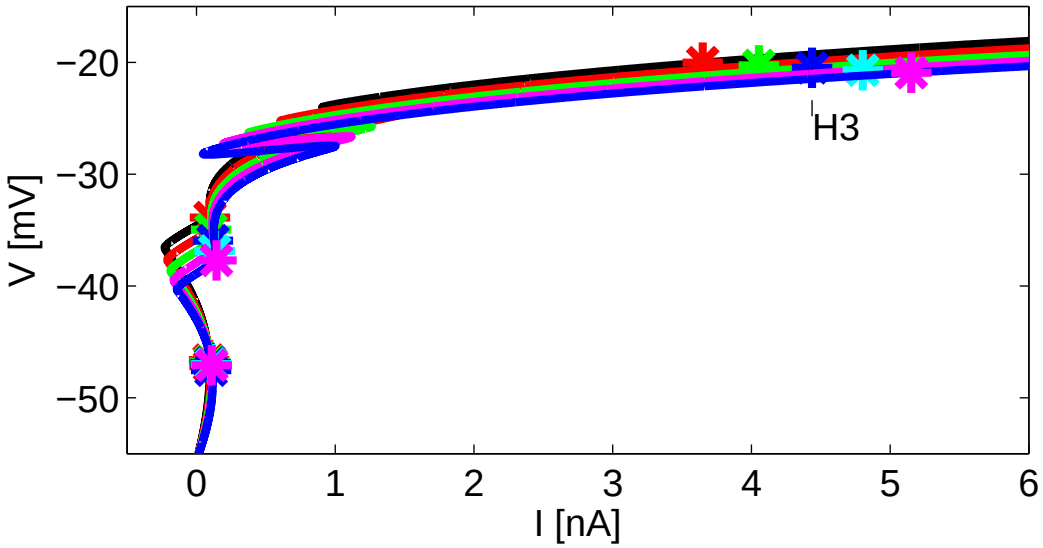

Figure 3.17: Variants of the continuation curve as the conductance of all channels are simultaneously changed. Color of line maps [black, red, green, magneta, blue] to $p = [0.8, 0.9, 1.0, 1.1, 1.2]$, the multiplier on the nominal value.

across all schemes, is not a trivial process. A first approach at addressing this issue relied on a genetic algorithm to test and score the model for each of the experimental cases, using a combined score at the end. While the genetic algorithm helped significantly in finding the ballpark of parameter space necessary for limit cycle behavior, modeling afterdischarge and ensuring an appropriate degree of excitability still required direct simulation.

To address these issues and guide hand-tuning, continuation analysis provides a close look at where oscillations come from in the system and what variables are associated with them. Using this method of analysis, parameters were discovered in the system that could alter the position of a Hopf point along the continuation curve without altering the continuation curve itself. The result fits our intuition, based on the definition of the time constant. Time constants don't factor into any steady-state values. Rather, they describe the time-course required for the relevant system variable to reach steady state. The shape of the continuation curve, should therefore remain unaltered when these values change - but they still affect the dynamics through manipulating the location of the Hopf point of interest along the curve. This fact is not immediately apparent and required this in-depth continuation analysis to bring it to light and make it actionable information.

The result of the parameter changes in the potassium timing create an interesting picture. Quattrocki's time constants for expressed I_{K2} channels are on the order of 10^{-2} s, while our own measurements of the fast current in potassium voltage clamp data provided by the Magoski Lab are on the order of 10^{-3} s (Figure 2.9). Meanwhile, Strong and Kaczmarek measured tail currents of the potassium current to be on the order of 10^{-2} s [98]. Prior to tuning via continuation analysis, we used a value of 4×10^{-2} s. However, after continuation tuning $\tau_h = 1.8 \times 10^{-2}$ s. It seems that timing constants on the order of 10^{-2} s serve as a useful effective current to represent both I_{K1} and I_{K2}. It would be interesting to see how one could manipulate Hopf locations on the continuation curve when including both of these currents!

The computational investment required to produce continuation curves is high and the Matcont software is not automated, requiring different options for different regions of parameter space to be attempted and discovered as they fail or succeed. A comprehensive investigation into how parameter changes affect continuation curves would require a long-term collaboration between analytical and applied mathematical disciplines, constrained by the neurobiology. For example, here we use eigenvector analysis of the nominal system at the location of relevant dynamics (e.g., the Hopf point in the case of the bag cell model). This allows the model to be tuned to match biological observations. After some investigation, much of this process could be automated. There are likely several other analytical tools that could prove useful if applied in a similar fashion to modeling problems.

Chapter 4

Wave propagation in various topologies of the electrically coupled *Aplysia* bag cell network model

Gap junctions are a distinct type of coupling that occurs between biological neurons. Unlike chemical synapses, which involve a delay, gap junctions directly link the dynamics of the membrane potential of neurons in a straightforward way that can be modeled relatively easily using an electrical coupling term between participating neurons [61].

In *Aplysia*, the bag cell neurons exist in clusters in the abdominal ganglia, coupled electronically via gap junctions. Little is known about the connectivity between neurons in the bag cell cluster. In 1979, an experimental study of bag cell processes determined that bag cell neurons are multipolar, having two or three major processes originating from the soma [54]. Further, it was determined that electrical coupling that occurred near the soma of the bag cell neurons was much stronger than the distal coupling between neuritic processes that extended from bag cell neurons. These results imply network model construction should implement sparse or nearest-neighbor coupling when considering network topology in the absence of experimental work on a definitive topology for the *Aplysia* bag cell cluster. Recent experimental work has shown that the connection strength of gap junctions between neurons is decreased by Ca^{2+} influx [30]. Thus, an investigation into how changes to the coupling strength affect network dynamics is desired.

When considering a network, N instances of the modified prototype *Aplysia* bag cell neuron are generated. As such, an N-neuron network is encoded by $10N$ variables. For the nth neuron, the membrane potential is modified such that

$$\dot{V}_n = \dot{V} + \frac{D_n}{C} \sum_{m=1}^{N} A_{m,n}(V_m - V_n) \tag{4.1}$$

where $\dot{V}$ is Eq. (A.1) as before, N is the number of neurons in the network, V_m is the mth neuron in the network, V_n the nth neuron in the network, D_n is the coupling constant,

and A is the association matrix that indicates which pairs of neurons have connections. The matrix A is an $N \times N$ matrix, where each row designates the mth neuron and column entries for that row determine the relationship between neuron m and all other neurons in the network. For instance, if the mth and nth neurons share a reciprocal connection, then $A_{m,n} = A_{n,m} = 1$. When there are no connections between a neuron, $A_{m,n} = A_{n,m} = 0$. Rectifying connections can be handled by $A_{m,n} = 0$, $A_{n,m} = 1$ or $A_{m,n} = 1$, $A_{n,m} = 0$. Some common types of association matrix used include

$$A_m = \begin{bmatrix} 0 & 1 \\ 1 & 0 \end{bmatrix}, A_r = \begin{bmatrix} 0 & 1 & 0 & 1 \\ 1 & 0 & 1 & 0 \\ 0 & 1 & 0 & 1 \\ 1 & 0 & 1 & 0 \end{bmatrix}, A_s = \begin{bmatrix} 0 & 1 & 0 & 1 & 0 \\ 1 & 0 & 0 & 0 & 1 \\ 0 & 1 & 0 & 0 & 1 \\ 0 & 0 & 1 & 1 & 0 \\ 1 & 0 & 1 & 0 & 0 \end{bmatrix},$$

in which A_m is a mutually connected two-neuron network, A_r is a four-neuron ring network, and A_s is a five-neuron scatter network. The association matrix makes topology construction intuitive and can be implemented with computational efficiency via vectorization in Matlab.

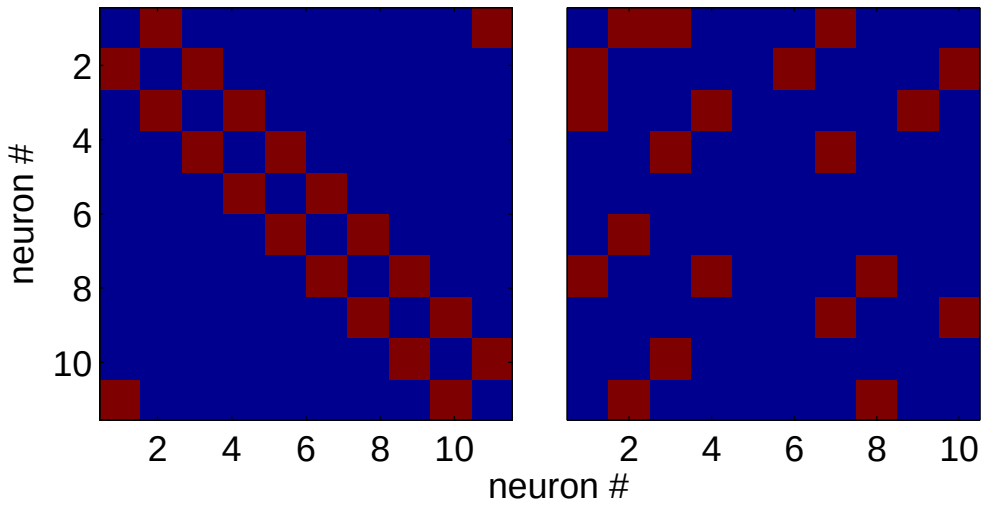

Figure 4.1: The topology matrix for a ring (left) and scatter (right) network. Binary values are represented by red ($A_{m,n} = 1$) and blue ($A_{m,n} = 0$).

4.0.1 Synchronization in a two-neuron network

The *cross-correlation* serves as measure of synchronization between two signals in experimental contexts. Here, we use Matlab's *xcorr.m* to reproduce the measure on simulated neurons. The cross-correlation compares two signals by introducing a delay (known as *lags*) between them and varying it to see how well correlated the signal is at each value for the delay.

A first verification of the network properties compares a simple 2-neuron model ensemble to a similar experimental arrangement in culture. In the experiment, two pairs of neurons are tested [29]. In each case, both neurons are driven at $I = 1.0$ nA, but only one pair of neurons is coupled. For the uncoupled pair, no phase locking occurs. To achieve this result *in silica*, the value for capacitance is varied for one of the neurons to elicit a unique frequency dependence. As expected, the uncoupled *in silica* neurons are not phase-locked (Figure 4.2). With strong coupling ($D_n = 0.05$ μS), the driven neurons quickly synchronize with a delay similar to that observed in experiment (Figure 4.3). In the model, an applied current of 1.5 nA is used.

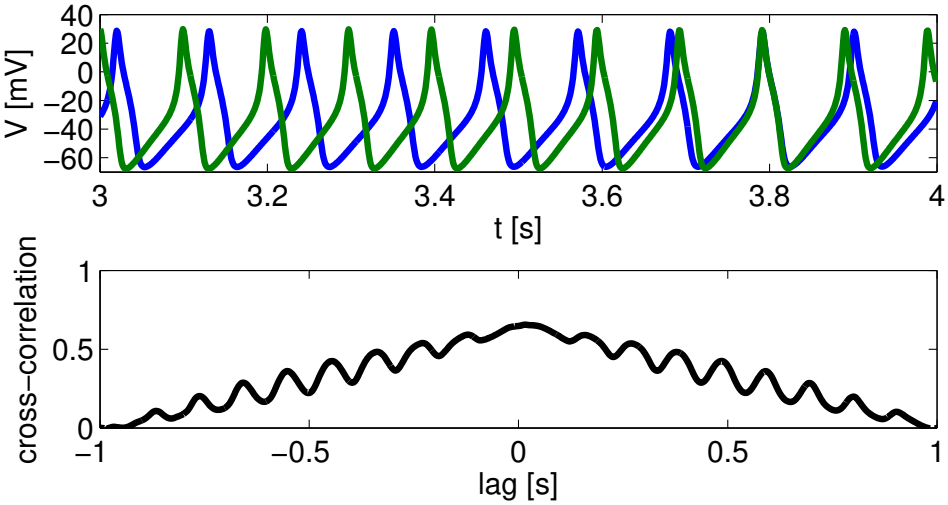

Figure 4.2: The membrane potential (top) and cross correlation (bottom) for two uncoupled model neurons driven at 1.5 nA. The intrinsic properties of the two neurons are identical with the exception of capacitance, $C_1 = 1300$ pF and $C_2 = 920$ pF. Cross-correlation is computed over 1.0 s window shown in top plot.

Another experiment in the same study examined the effects of driving one neuron of a coupled pair with an applied current and observing the effects on the unstimulated neuron. Unlike the experimental result, which showed a gradual ramping up in the amplitude of the oscillations ([29], Figure 5D) the unstimulated model neuron appeared to be responding as a temporal coder, wherein a superposition of closely timed inputs produces an a spike (Figure 4.4). This disparity in results may indicate that the Hopf bifurcation in the model points in wrong direction compared to the experiment. The ramping up of amplitudes is consistent with a Hopf point starting at low I and growing with increased I, whereas the model features a Hopf bifurcation at high I growing with decreased I, as demonstrated by continuity analysis. Constructing or altering a model to enforce appropriately behaving bifurcations is not a trivial task and the result could ultimately come down to unintuitive network properties or additional currents, so this avenue was not pursued. For example, addition of other, known *Aplysia* bag cell currents, or the splitting of the potassium current into its component pair will likely alter the continuation curve of the model with respect to I.

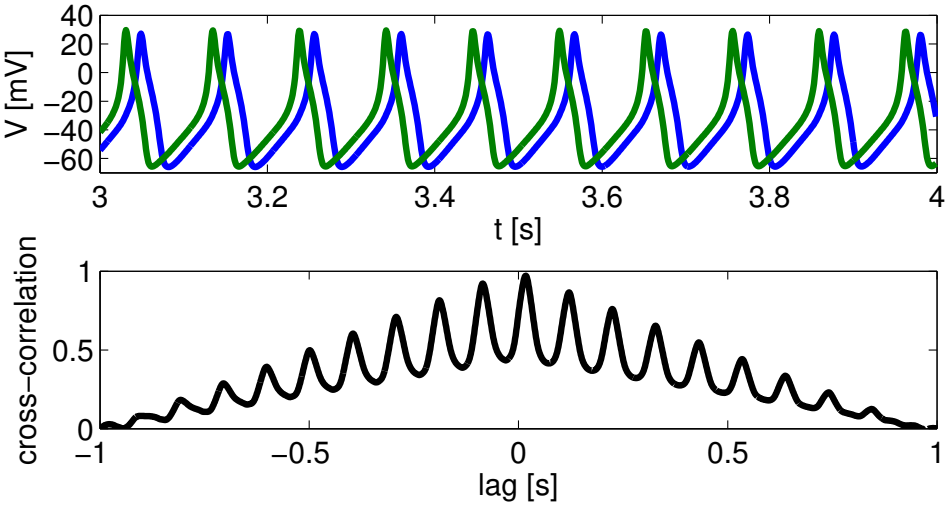

Figure 4.3: The membrane potential (top) and cross correlation (bottom) for two coupled model neurons ($D_n = 0.01$ μS) driven at 1.5 nA. The intrinsic properties of the two neurons are identical with the exception of capacitance, $C_1 = 1300$ pF and $C_2 = 920$ pF. Cross-correlation is computed over 1.0 s window shown in top plot.

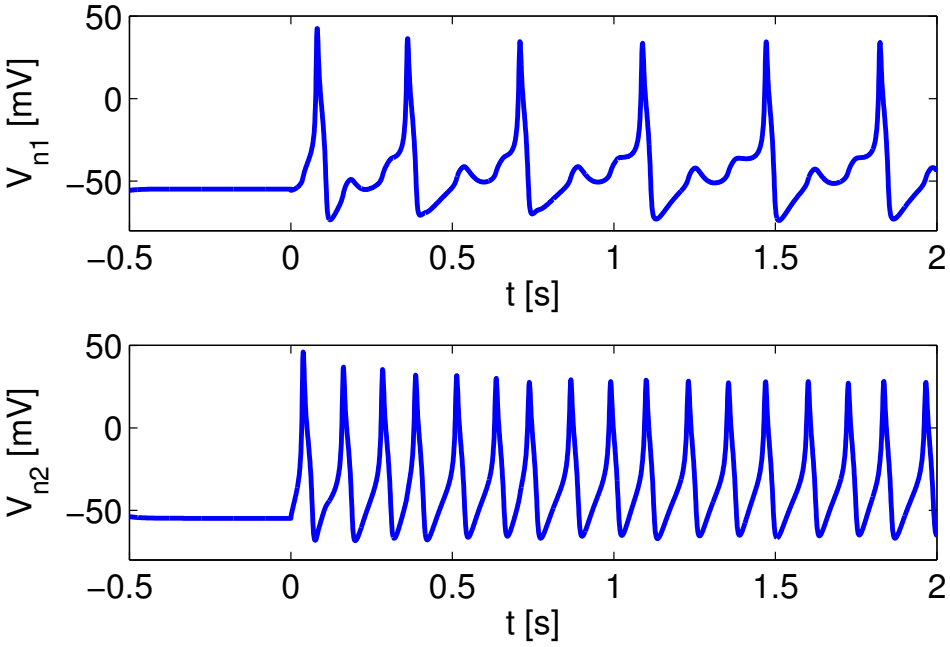

Figure 4.4: Two coupled model neurons ($D_n = 0.015$ μS) with only V_{n2} driven at 1.5 nA. The intrinsic properties of the two neurons are identical with the exception of capacitance, C.

4.0.2 Wave propagation in a network

In order to study wave propagation, three network topologies are implemented on the *Aplysia* network model. In a *ring* network, each neuron couples reciprocally to its two

nearest neighbors, forming a chain. The first and last neurons are then linked together to complete the ring. In the *ring cluster* network, a ring network is augmented with two additional connections so that each neuron is coupled to its nearest neighbors as well as its *next* nearest neighbors for a total of four connections per neuron. Finally, in a *scatter* network, connections are determined randomly and have no linear order to them. The results for scatter-type networks vary greatly depending on how dispersed the connections are through the network. When connections get concentrated on a single neuron, the electrical coupling often acts as a drain on the network, suppressing most of the neurons from activating. In this case, only well dispersed networks are used, which are found mostly through trial and error.

The membrane potential of each neuron was perturbed slightly from the resting potential, using a normal distribution with approximate variance of 1.0 mV about -54 mV. Additionally, the capacitance was perturbed using a normal distribution of 20% (272 pF) about 1363 pF. These alterations introduce some variability to the network. A single, stimulated neuron received 10s of 5 Hz stimulus, with maximum 1.4 nA and an on-duration of 150 ms. The choice to stimulate a single neuron in an intact cluster follows from Brown [11]. To date, Brown's results have not been successfully repeated, but it is one of the only cases of comprehensive experiments on bag cell networks reported in the literature.

As the stimulated neuron is excited by this experimental protocol, known to initiate afterdischarge in experiments, the excitation spreads through the network. The network is left running until it reaches a final time of $t_f = 120$ s.

In the simple (nearest neighbor) network, with $D_n = 0.015$ μS, wave propagation initially only occurs within a small group of less than 20 neurons during external driving (Figure 4.5A). The waves themselves propagate at about 35 neurons per second, but don't extend past the first ten neurons on either side of the stimulated neuron (neuron 50). During afterdischarge, the wavefront spreads to the whole network, sending waves of excitation at a rate just under 2 Hz, traveling at the same approximate rate of 35 neurons per second (Figure 4.5B). Inflections in the wave front temporally (the wave collision at neuron 37 vs. the wave initiation at neuron 13) are a likely a result of the asymmetries in the network introduced by varying initial conditions and capacitance. At this point, no neurons are receiving external current, and the process is driven entirely by Ca^{2+}-dependent channels, as we will explore in more depth in the next section. A profile of the stimulated neuron (neuron 50) and a distant neighbor (neuron 60) verifies that initially, the wave front is not spreading to the distant neurons. However, the simulated neuron is spiking faster than the driving current, likely due to feedback from its neighboring neurons, delivered through the electrical coupling term (Figure 4.5C). This feedback may deplete energy from the wave spread as it is returned to the stimulated neuron. During the persistent spiking phase, the two neurons are locked in the traveling waveform (Figure 4.5D).

In the cluster (nearest and next-nearest neighbor) ring network, wave propagation comes easier to the whole network at the same coupling strength ($D_n = 0.015$ μS) as used in the simple ring network (Figure 4.6A). The waves travel at 85 neurons per second, spreading across the whole network with minimal failure at every peak of the stimulated neuron. Feedback on the stimulated neuron is not as robust as in the simple ring network, causing

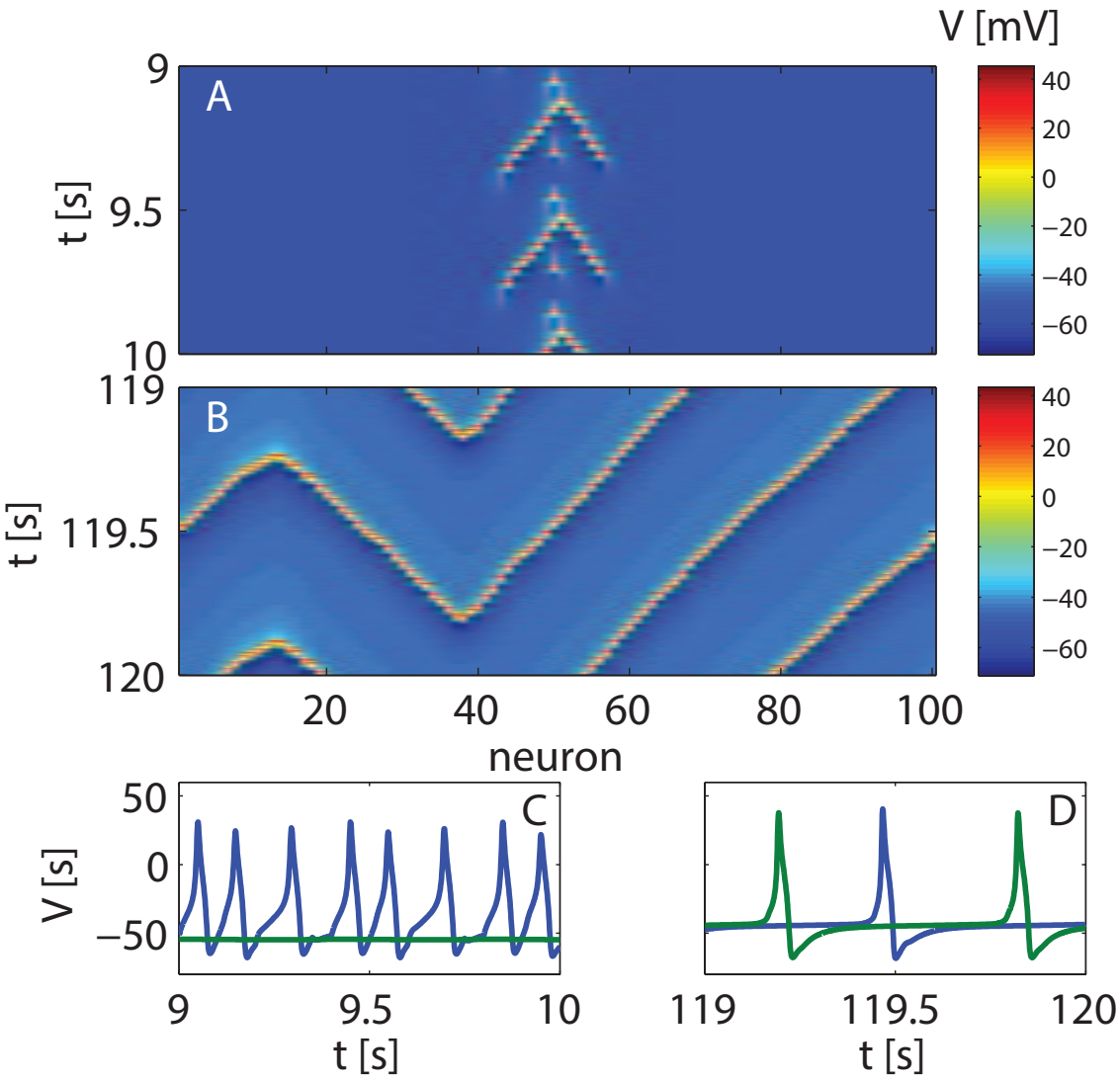

Figure 4.5: $D_n = 0.015$ μS for a spatially extended 100 neuron ring network with a single bag cell neuron being driven by a 1 nA, 5 Hz current for 10 s. A: the membrane potential across the network for the first second of activity, B: the membrane potential across the network over the 120th second of activity. C: a time-series plot of the driven neuron and neighbor ten neurons away from the driven neuron in the first second, and D: the same neuron pair after 119 seconds.

slower polarization (Figure 4.6C). This is likely a result of the stimulated neuron being drained now by four nearby neurons instead of two, as in the simple ring case. The resulting waveform during afterdischarge, two minutes later maintains the same approximate wave speed of 85 neurons per second, over two times faster than the simple ring, but still maintains an interwave frequency of less than 2 Hz (Figure 4.6B). This can be observed in the stimulated neuron and the distant neighbor neuron, 10 neurons away (Figure 4.6D), as their spike emissions are closer in time, but each neuron's interspike delay remains just

over 0.5 s.

The scatter network differs significantly from the ring networks in that its topology is not well defined. Because a certain degree of dispersity of connections is enforced, the resulting network tends to have no long distance connections within it. For example, in a 100-neuron ring network, you can be certain that neuron 01 and neuron 50 have the longest distance between them that a wave must travel. In a dispersed scatter network, any would-be long distance connections are often shortcut by other, random connections. This increases the overall energy dispersion in the network, so the coupling constant must be increased to compensate for the additional drain on the stimulated neuron. For a scatter network with a coupling strength of $D_n = 0.02$ μS, the network was immediately responsive to the stimulated neuron during the driving phase (Figure 4.7A). Excitation appears scattered, but may still contain wave-like behavior. Because a scatter topology cannot be neatly mapped to two dimensional space like a ring network, the spatial component (the neuron axis) of the spatiotemporal plots is not as informative in the scatter case. However, spatial arrangement becomes less important during afterdischarge in the scatter topology as the wave no longer travels across the network, but occurs across the network in a much shorter window of time (Figure 4.7B), likely because of the shortcuts introduced through scatter coupling. For the scatter network, firing occurs nearly simultaneously during persistent spiking for the previously stimulated neuron and its distance neighbor (Figure 4.7D).

This preliminary look at spatiotemporal dynamics in the *Aplysia* bag cell cluster model demonstrates how network topology can affect wave propagation. In some cases, topology can even alter the requirements on the coupling strength, D_n, for wave propagation to occur, as was the case in the scatter topology. Experimental investigations into the general structure of network topology can help confine future bag cell cluster models, and these theoretical insights may give experimentalists clues on ways to test propagation in a cluster.

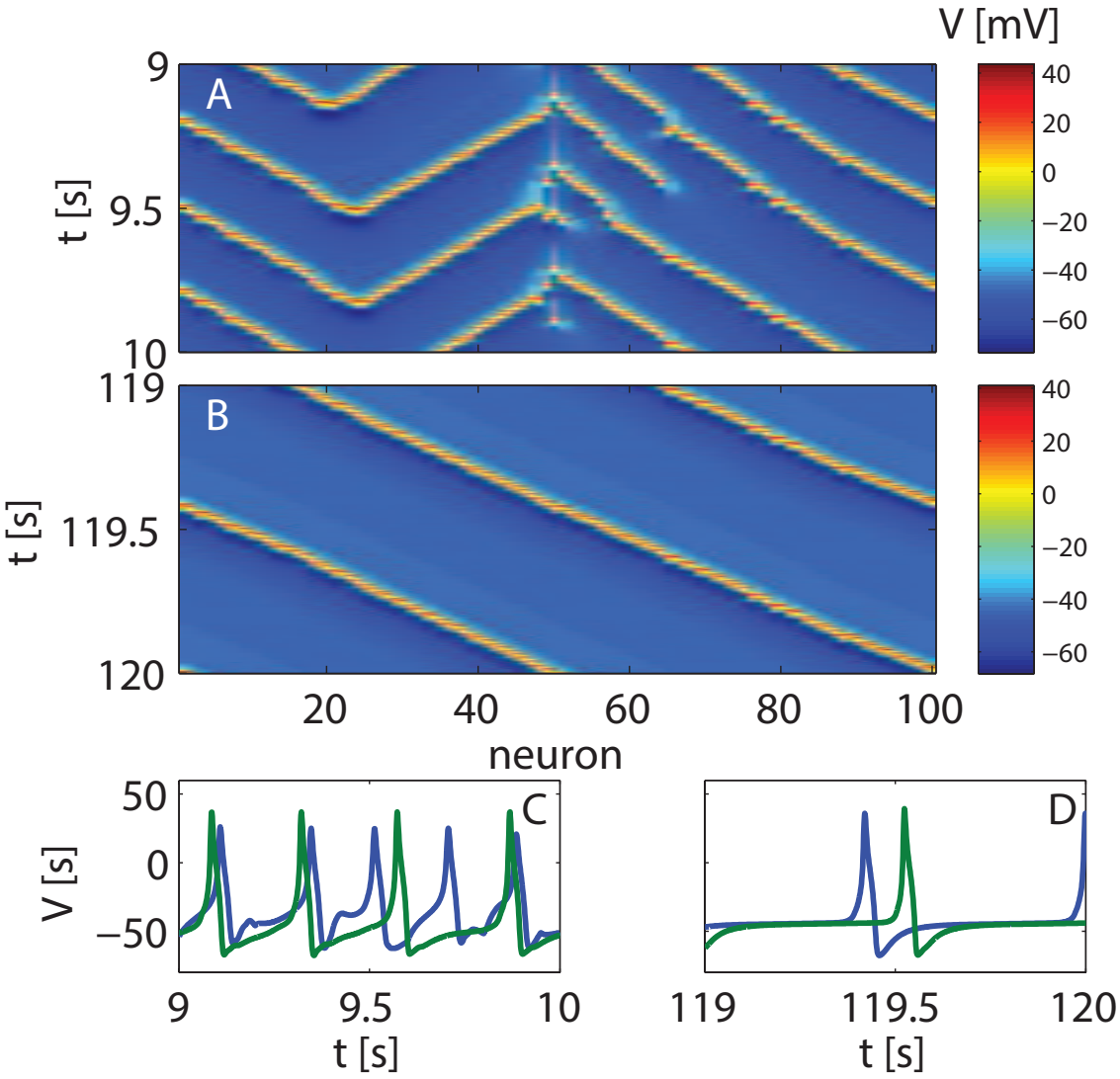

Figure 4.6: A cluster ring network topology with $D_n = 0.015$ μS. A: the membrane potential across the network for the first second of activity, B: the membrane potential across the network over the 120th second of activity. C: a time-series plot of the driven neuron and neighbor ten neurons away from the driven neuron in the first second, and D: the same neuron pair after 119 seconds.

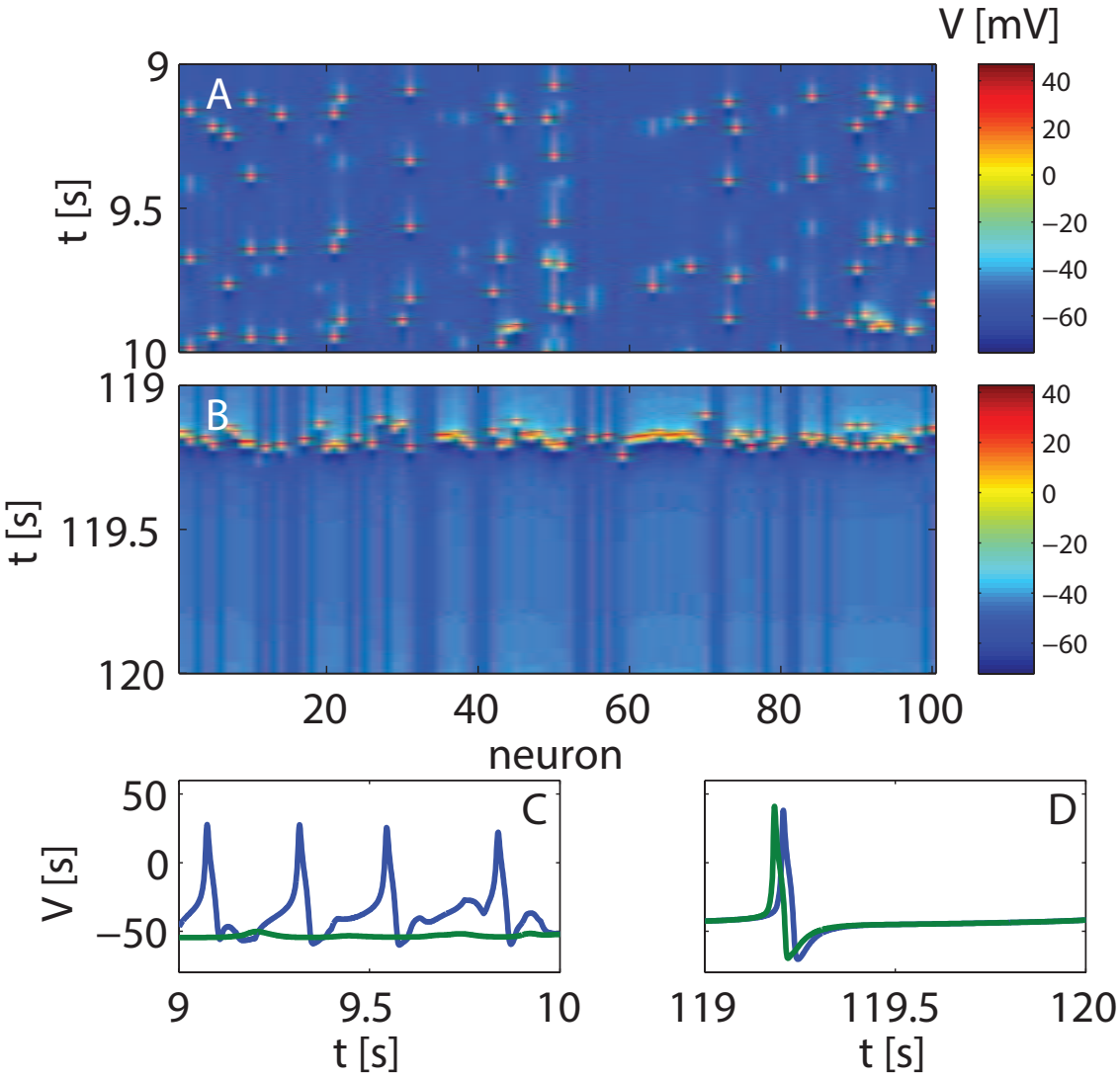

Figure 4.7: A scatter network topology with $D_n = 0.020$ μS. A: the membrane potential across the network for the first second of activity, B: the membrane potential across the network over the 120th second of activity. C: a time-series plot of the driven neuron and neighbor ten neurons away from the driven neuron in the first second, and D: the same neuron pair after 119 seconds.

4.0.3 Effect of coupling strength and network size on phase coherence

In biological neural networks, synchronization is thought to play an important role in managing communication between networks of neurons, mediating relationships between distinct subpopulations of neurons [100] by modulating their interactions [108]. Synchronization is used for timed encoding in the hippocampus [26] and plays a role in directing network processing to relevant perceptions in attention processes [96]. Further studies have found synchronization to play a role in use-dependent plasticity, motor performance enhancement, perception, and the dynamic grouping of neural populations [95] which appears to play a role in integrating large-scale processing across the nervous system [100]. In the *Aplysia* bag cell cluster, synchronization likely plays a role in increasing the efficacy of peptide release, ensuring downstream neurons receive the signal to prepare each of the slug's participating cells for egg-laying behavior [29]. It is thus, of interest, to see how synchronization in a bag cell cluster may depend on network properties such as connectivity of the network or the strength of the electrical coupling between neurons.

Care must be taken in defining synchrony. The phase coherence discussed in this section is not comparable to the cross-correlations used earlier. For example, in the scatter network of the previous section, firing of neurons happened more simultaneously across the network. Pairs of neurons from this network would likely yield a high cross-correlation compared to the ring network. However, phase coherence measures the disparity in phase between each neuron in the network. In the ring network, at any given time, most neurons are all in the rest state, thus they are more synchronized in the ring network from a phase-coherence perspective, despite the scatter topology producing, arguably, more synchronized spiking. It is sufficient to say that previously, cross-correlation was used and now phase-coherence is being used and they are each measures of different aspects of synchrony of a system.

To measure phase coherence in the system, the Kuramoto order parameter is used [65]. The order parameter measures the average distance in radians between the phase angles of members of the network and provides a value encoding the disparity in phase angle across the network. In order to define a phase angle, two coordinates in the system must provide a closed loop that define the system's membrane potential oscillations. To find such a coordinate pair, we first look at the *Aplysia* bag cell's ten dimensions, comparing the membrane potential, V, to each of the other dimensions. It is immediately obvious that the $V - n$ plane exhibits the most circle-like trajectories (Figure 4.8).

The center of the planar oscillation is defined by $(V, n) = (-20, 0.26)$ (Figure 4.9, left), the approximate center of the traces drawn by the trajectories over time (blue lines). The phase angle, θ_i is measured from this point's x-axis to the angle (red lines) given by the direction vector from the origin to the trajectory's point in (V, n) (red dots). From here, the order parameter is defined

$$Re^{j\Psi} = \frac{1}{N}\sum_{i=1}^{N} e^{j\theta_i}, \tag{4.2}$$

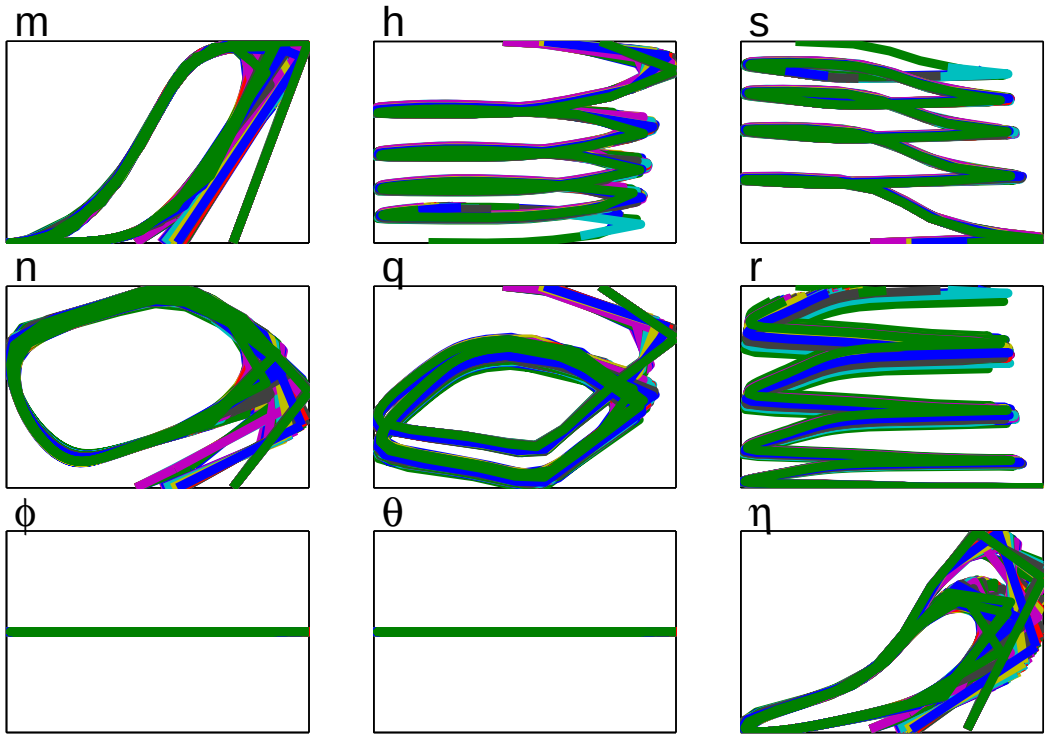

Figure 4.8: Trajectory projections of all 100 neurons on a two-dimensional plane comparing the membrane potential (horizontal axes) to each of the other nine dimensions (labeled for each plot).

where $j = \sqrt{-1}$, N is the total number of neurons, and θ_i is the phase angle of the ith neuron, as defined by the transformed origin. The result is a complex number, $Re^{j\Psi}$, which can be decomposed into the order parameter, R, and the average phase angle, Ψ. Here, we consider only the order parameter, extracting it with

$$R = \sqrt{(\Re[Re^{j\Psi}])^2 + (\Im[Re^{j\Psi}])^2}. \tag{4.3}$$

where $Re^{j\Psi}$ is defined in Equation 4.2.

Extracting both R and Ψ for comparison, the distribution of average phase angles over time and the disparity between them can be viewed in polar coordinates (Figure 4.9). In this case, we see the system is highly synchronized at 240^0, near the rest state $(V, n) = (-60, 0.15)$. This isn't surprising, as even oscillating trajectories tend to get caught near the resting potential for some time as they pass by it and observations of the active network demonstrate that neurons spend most time there between spikes.

To confirm that the order parameter measures synchronization in an intuitive way, an uncoupled ($D_n = 0$) 100-neuron network is initiated. All neurons are set with the exact same internal parameters and set to the same initial condition. The network fires synchronously (Figure 4.10, top left) and a time-average of the resulting phase coherence is taken from the period over which it's displayed, yielding $\langle R \rangle = 1.0$, indicating perfect

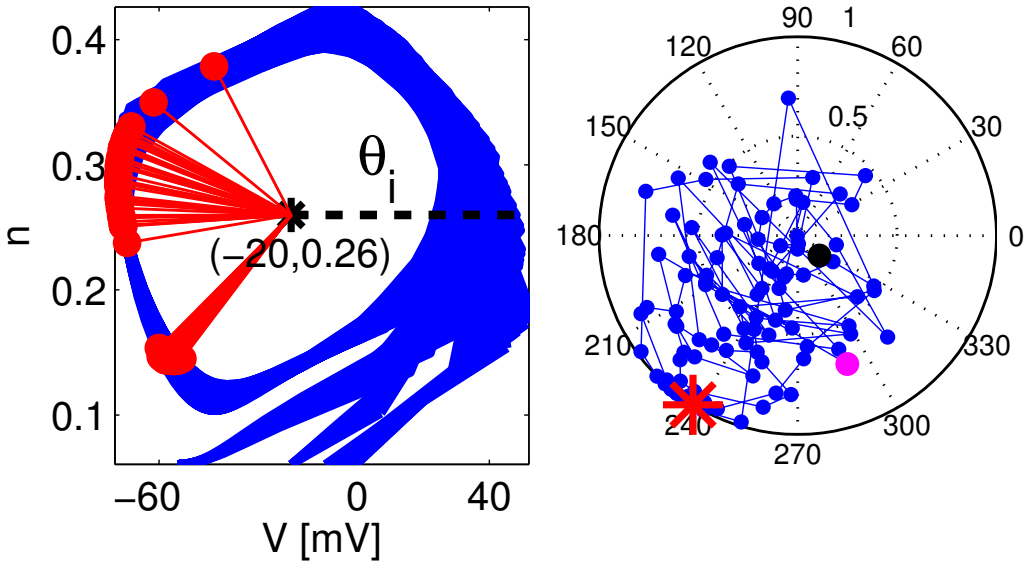

Figure 4.9: Left: the angle, θ_i, in the Kuramoto order parameter is defined as the angle from the transformed origin's horizontal axis (black asterisk and black, dotted line) to the ith neuron's point in (V, n) for a single point in time. Right: the order parameter shows the evolution of the the average phase of the network (polar angle of blue dot) and the phase coherence (polar magnitude of blues dot) at each point in time, starting at $t = 0$ s (black dot) and ending at $t = 0.5$ s (magenta dot). The time point cooresponding to figure left is distinguished (red asterisk).

synchrony (Figure 4.10, top center). Next, the initial conditions and the capacitance of each neuron are perturbed in a Gaussian distribution about their nominal values and the (still uncoupled) network is stimulated. This time, the difference in firing rate and initial conditions sets each neuron on its own path, leading to a noisy pattern and unsynchronized firing (Figure 4.10, bottom left) and the corresponding order parameter is much lower (Figure 4.10, bottom center). A moving average of the phase coherence, R, is taken and denoted $\langle R \rangle$. Notice, however, that the phase coherence does still reach the instantaneous phase coherence value, $R = 1.0$ frequently, when most of the network is in the rest state. This demonstrates how the phase coherence measures synchrony of the system with no bias towards a particular state. To the right, the Ca^{2+} levels are shown as they will play a role in the coupled system.

To see how network topology affects phase coherence, the order parameter is applied to the *ring*, *ring cluster* and *scatter* network topologies (recall Figure 4.1). The experiment is performed in an afterdischarge schema, selecting a single neuron to receive the 5 Hz, 10 s input. The membrane potential of all neurons, including the stimulated neuron, are set to values perturbed a small amount about the rest potential and the capacitance of each cell is perturbed around the nominal capacitance value to emulate variability in the network. In the case of the scatter network, a low 0.5 nA input current is injected into the neurons to help propagate activity when the coupling constant is equivalent to the ring and cluster ring topologies. A moving average of the phase coherence, R, is taken from the

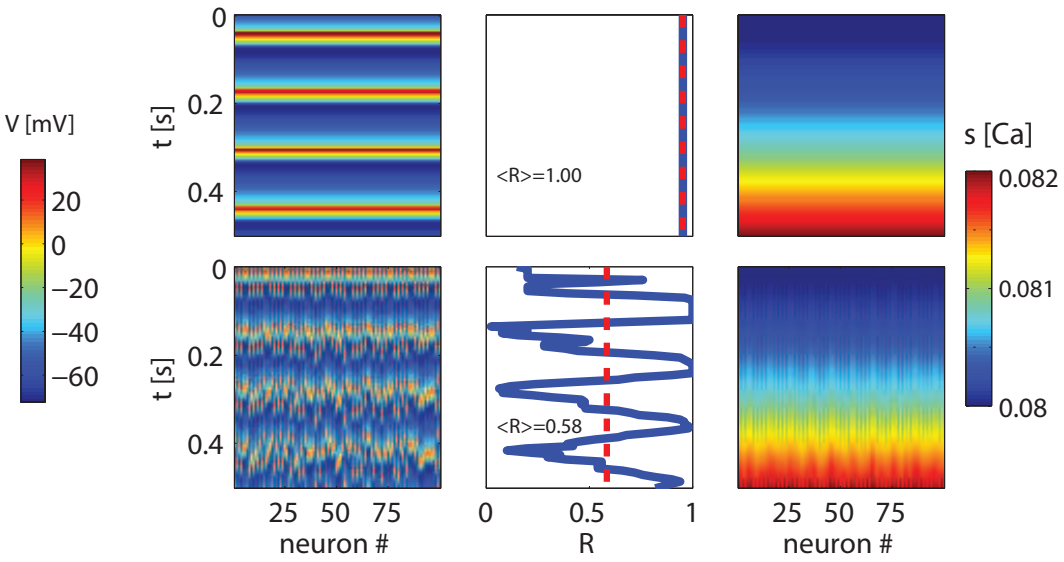

Figure 4.10: The uncoupled network, with all initial conditions and parameters homogenized, fires synchronously (top left) giving an order parameter, $R = 1.0$ (top middle). An uncoupled perturbed network appears disordered (bottom left) and the order parameter (middle bottom) reaches lower values. The instantaneous phase coherence (black line) is averaged over the given window to produce the mean phase coherence (red, dashed line). The microdomain's Ca^{2+} concentration, s, steadily increases with time (top and bottom right). The color map's orientation in color space decreases towards blue ($s = 80$ mM) and increases towards red ($s = 100$ mM).

time-window over which its instantaneous value is plotted.

For the ring network, wave propagation is slow and discrete (Figure 4.11, top left). That is, the wave front spreads only to a portion of the network at a time. It isn't until Ca^{2+} levels are sufficient within those neurons (Figure 4.11, top right) that they enter discharge and spread the waveform to nearby, resting neurons. Because this is such a slow process in the ring network at low coupling strength, the time stamps of measurement were much later than for the other cases discussed in this section. It wasn't until 210 s that the entire network was caught in the traveling wave (Figure 4.11, bottom left). By this time, the Ca^{2+} microdomain concentration has leveled off at 90 mM (Figure 4.11, bottom left) denoted by the green hue. The phase coherence starts out high ($\langle R \rangle = 0.97$) for the network, as most neurons are initially all sharing the rest state, but eventually falls $\langle R \rangle = 0.90$ as the excitation spreads.

When the coupling strength is increased to $D_n = 0.05$ μS, waves easily entrain the entire network at the onset of afterdischarge (Figure 4.12, top left, $t = 10$ s). This correlates with Ca^{2+} saturating at 100 mM (Figure 4.12, top right, red hue) just before afterdischarge. After 120s, the Ca^{2+} concentration has leveled out to 88 mM (Figure 4.12, bottom right) and the moving average of the order parameter has settled to $\langle R \rangle = 0.94$ (Figure 4.12, bottom middle).

In the ring *cluster*, at $D = 0.015$ μS, the results are similar to the simple ring network

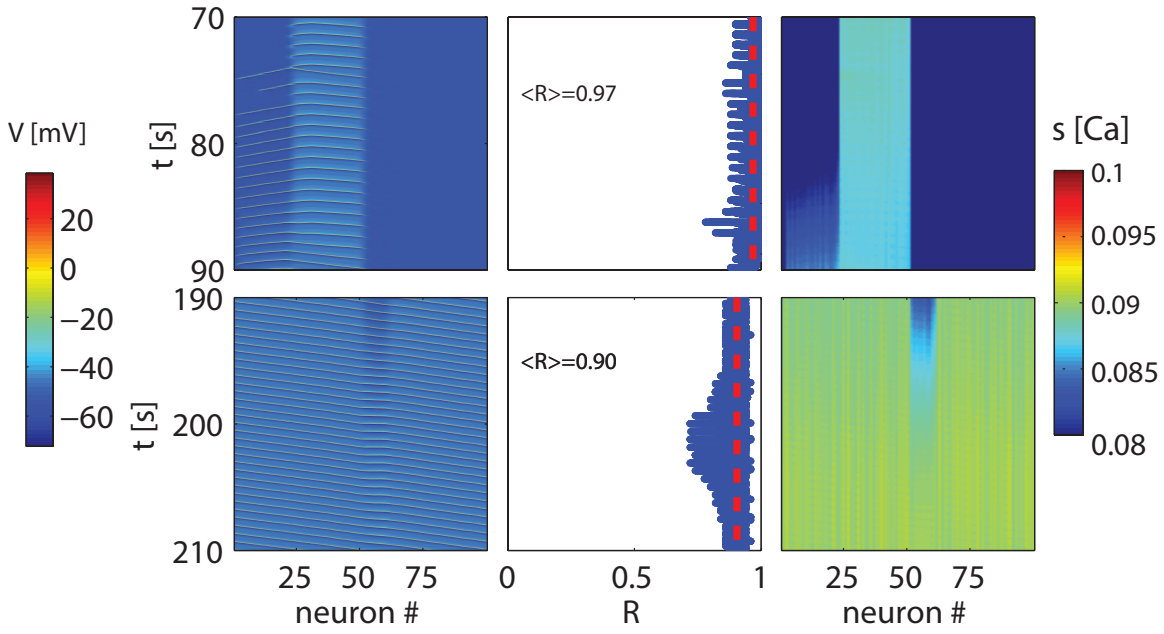

Figure 4.11: The membrane potential (left), phase coherence (middle), and Ca^{2+} concentration (right) for a ring network with $D = 0.015$ μS. Action potentials reach over 20 mV peaks (see Figure 4.10 for a higher resolution example). . The microdomain's Ca^{2+} concentration, s, steadily increases with time (top and bottom right). The color map's orientation in color space decreases towards blue ($s = 80$ mM) and increases towards red ($s = 100$ mM). The instantaneous phase coherence (black line) is averaged over the given window to produce the mean phase coherence (red, dashed line).

with a higher coupling constant (Figure 4.13, top left). However, distinct from the simple ring network, Ca^{2+} levels to do not saturate across the network (denoted by less red in the spatiotemporal plot in Figure 4.13, top right) like they do for the strongly coupled ring network, but eventually settle to a larger microdomain concentration of $s = 92$ mM. The average phase coherence after 110 s of afterdischarge is $\langle R \rangle = 0.89$.

In the scatter network, slow network propagation occurs at $D = 0.07$ μS (Figure 4.14, top left). The network activity is initially confined to a small handful of neurons, but begins to spread across the network after 20 seconds. Calcium levels remain low (Figure 4.14, top right) and phase coherence is high while most neurons sit at resting potential. At 120 seconds, when the majority of the network has entered a persistent spiking phase (Figure 4.14, bottom left), the overall microdomain concentration is approximately $s = 92$ mM (Figure 4.14, bottom right). Because of the random nature of electrical coupling in the scatter plot, some neurons often get left out of network activity (denoted by the streaks of blue in both the membrane potential and microdomain concentration spatiotemporal plots). The time-averaged order parameter is relatively high ($\langle R \rangle = 0.92$), but during spiking, the instantaneous phase coherence drops as low as $R = 0.5$.

When the coupling constant is increased to $D_n = 0.015$ μS, complete network activa-

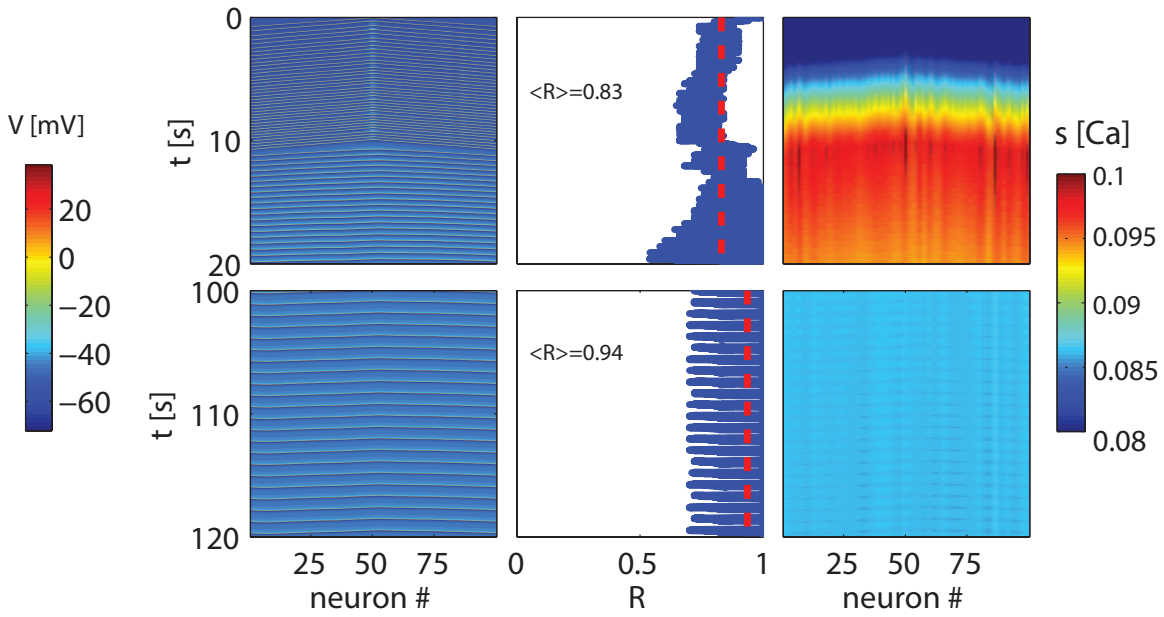

Figure 4.12: The membrane potential (left), phase coherence (middle), and Ca^{2+} concentration (right) for a ring network with $D = 0.05$ μS. The microdomain's Ca^{2+} concentration, s, steadily increases with time. The color map's orientation in color space decreases towards blue ($s = 80$ M) and increases towards red ($s = 100$ M). The instantaneous phase coherence (black line) is averaged over the given window to produce the mean phase coherence (red, dashed line).

tion is instantaneous (Figure 4.15, top left). By $t = 10$ s, Ca^{2+} levels in the microdomain are sufficient to induce activation of the whole network (Figure 4.15, top right). The time-averaged phase coherence after 120 s does not differ significantly from that for the weakly coupled scatter network, despite the instantaneous phase coherence reaching minimums near $R = 0.25$ (Figure 4.15, bottom middle). The Ca^{2+} concentration within the microdomain holds steady at 90 mM (Figure 4.15, bottom right).

Regardless of topology, the spread of activity through the 100-neuron network was dependent on sufficient internal levels of Ca^{2+} (as shown best by Figures 4.11, 4.13, and 4.15, top right). Calcium concentrations in the microdomain tended to stabilize around 90 mM and the networks appear to have reached a stable state of persistence by 120 s. Activity spread across the network in phases dependent on internal Ca^{2+} levels. First, rest neurons are stimulated by active neurons (which can be either the stimulated neuron or a neuron that has entered persistence). During this phase, waves travel short distances (in terms of number of neurons the signal propagates through), briefly stimulating nearby neurons, but with decreased excitability at long distances. As the neurons are stimulated, their internal Ca^{2+} levels rise, and they begin to excite their nearby neighbors.

This process unfolds slowly when connections are limited and the coupling constant is small, as in the weakly-coupled ring network in which excitations travel to neurons 1-25, originating from neurons 25-50, which have entered a persistent state, as indicated by

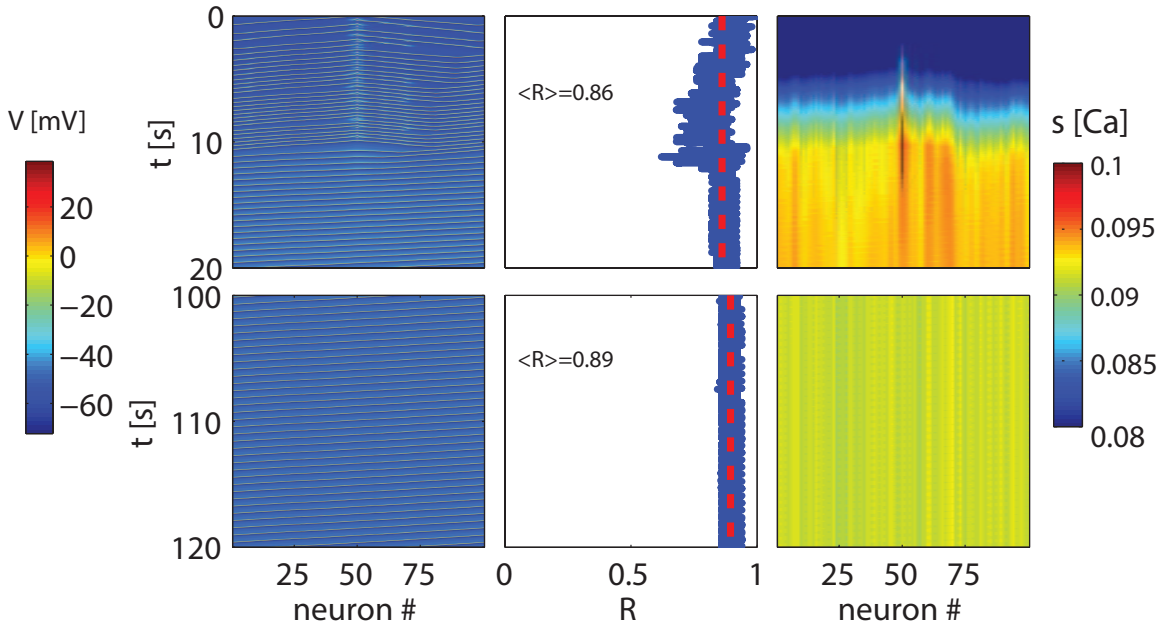

Figure 4.13: The membrane potential (left), phase coherence (middle), and Ca^{2+} concentration (right) for a ring cluster network with $D = 0.015$ μS. The color map's orientation in color space decreases towards blue ($s = 80$ M) and increases towards red ($s = 100$ M). The instantaneous phase coherence (black line) is averaged over the given window to produce the mean phase coherence (red, dashed line).

their raised resting potential (Figure 4.11, top left) and their increased internal Ca^{2+} levels (Figure 4.11, top right). This ring network is a unique case, as the asymmetry induced by varying initial conditions and capacitance has randomly prohibited wave travel to the right. It's not until $t = 200$ s that internal Ca^{2+} levels in neurons 50-60 (Figure 4.11, bottom left) reach sufficient levels for the neurons to get in phase with the rest of the network (as demonstrated by the minimum of R increasing after all neurons have entered persistence (Figure 4.11, bottom middle). Increasing the connectivity (as in the ring cluster and the scatter network topologies) or increasing the electrical coupling conductance, D_n, both make this process faster (as in Figures 4.13, 4.12 and 4.15).

Within, the bag cell clusters of the biological *Aplysia*, the coupling strength is regulated by various processes. Calcium, in particular, had an effect on coupling strength when measured in *Aplysia* bag cell cultures [30], reducing coupling strength as Ca^{2+} levels increased. Adding such a dependency to the present *Aplysia* bag cell model will likely require an understanding of how different topologies and coupling strengths correspond to different Ca^{2+} levels. This preliminary work looks across the various options for insights into how such a dependency may look, quantitatively. To this end, phase coherence analysis is extended statistically on the ring and ring cluster networks, running sets of 10 120-second trials and averaging the time-averaged phase coherence, $\langle R \rangle$, across trials from the last 20 s of run time, as was done for spatiotemporal plots (Figure 4.15). In this way, the long-term phase coherence is measured across changing coupling strength as well as network size.

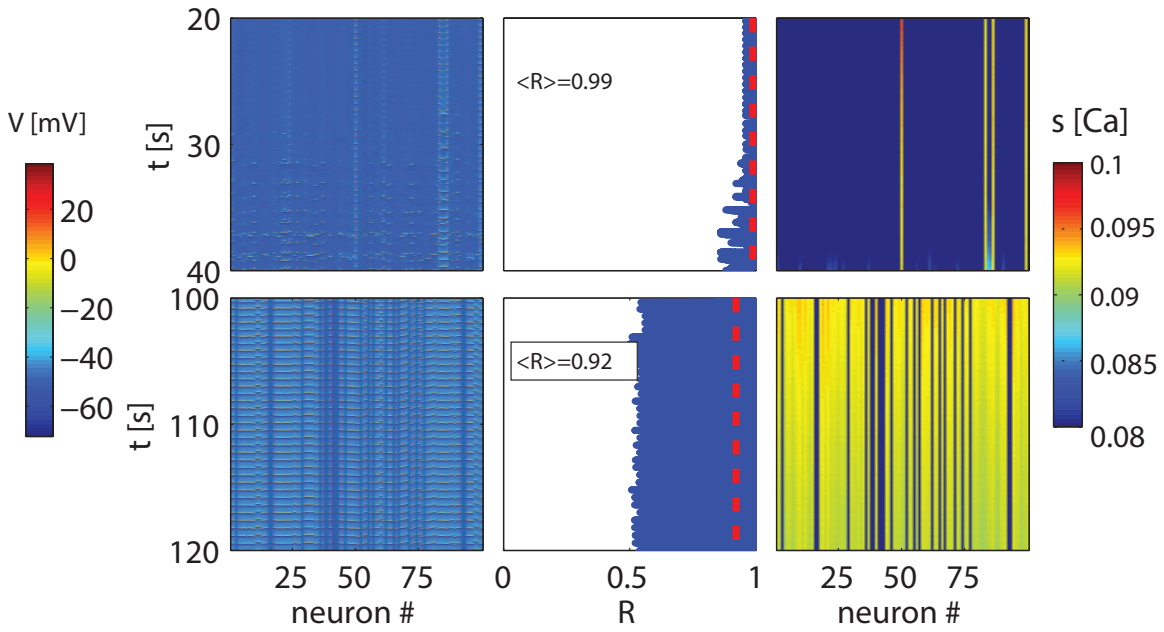

Figure 4.14: The membrane potential (left), phase coherence (middle), and Ca^{2+} concentration (right) for a scatter network with $D = 0.007$ μS. The color map's orientation in color space decreases towards blue ($s = 80$ M) and increases towards red ($s = 100$ M). The instantaneous phase coherence (black line) is averaged over the given window to produce the mean phase coherence (red, dashed line).

In the simple ring network, average phase coherence and its associated standard deviation grow with increasing D_n over the the range 0.05 to 1.0 μS (Figure 4.16, top). At $D_n = 0.05$ μS, the low-variance average of $\langle R \rangle = 0.91$ was consistent across different network size (Figure 4.16, middle) but for stronger coupling, phase coherence decreased as the size of the network increased (Figure 4.16, bottom). Results for the ring cluster network were similar for the weakly coupled case, but the coupling strength becomes too strong at $D_n = 0.5$ μS. At this coupling strength, the stimulated neuron is being drained by it's four neighbors and isn't able to elicit an action potential, let alone a wave of excitation. As a result, the whole network settles at the resting potential once the 5 Hz, 10s stimulation ceases, resulting in $\langle R \rangle = 1.0$ (Figure 4.17, top).

Consistent with the observation that large coupling constants tend to drain the network, and very weak coupling constants don't allow any wave transmission at all, there exists a restricted range of D_n over which network propagation can occur. For example, in the simple ring network, phase coherence grows in the range $D_n \in (0, 1]$ μS, but hasn't quite reached $\langle R \rangle = 1.0$, where network collapse occurs and waves can no longer propagate (Figure 4.16 top). For the cluster ring, in which more connections are involved, the network has already collapsed at $D_n = 0.5$ μS (Figure 4.17, top), indicating that for this network topology, the window of coupling strengths for which the network can propagate waves is much smaller than the window of the simple ring network. If this network topology is similar to the biological *Aplysia* bag cell cluster's topology, it may explain why Ca^{2+}-

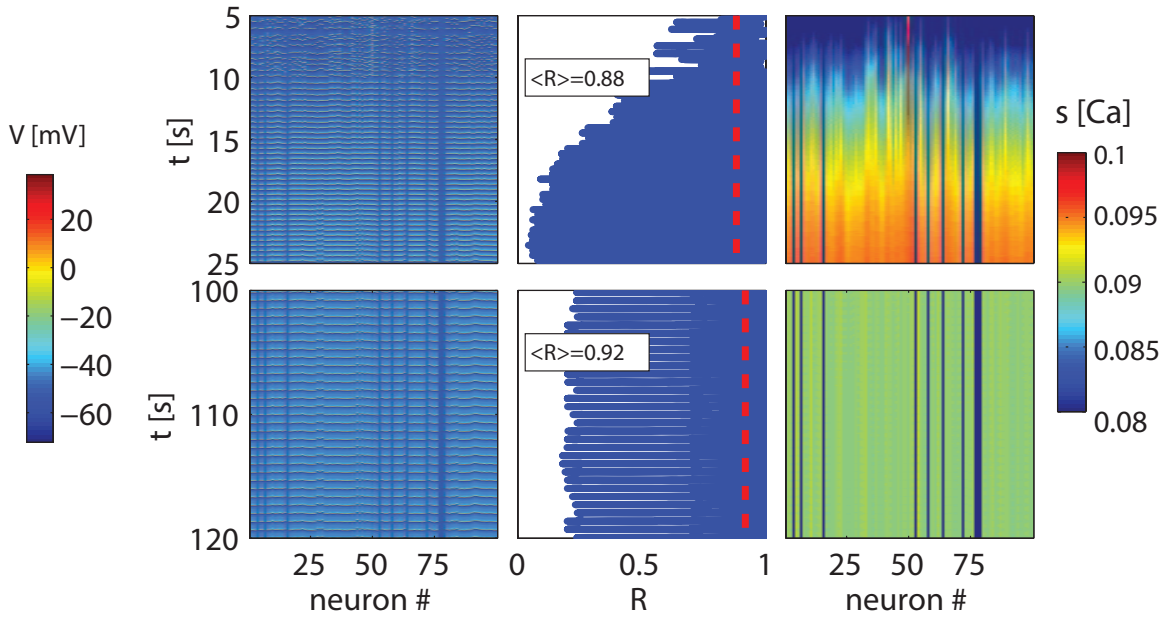

Figure 4.15: The membrane potential (left), phase coherence (middle), and Ca^{2+} concentration (right) for a scatter network with $D = 0.015$ μS. The color map's orientation in color space decreases towards blue ($s = 80$ M) and increases towards red ($s = 100$ M). The instantaneous phase coherence (black line) is averaged over the given window to produce the mean phase coherence (red, dashed line).

dependent down-regulation of the coupling strength is necessary to facilitate afterdischarge in the entire cluster [30].

4.0.4 Conclusions and Discussion

The network model constructed here starts with *Aplysia* bag cell prototype model, constructed over previous chapters. This model relies, largely, on Ca^{2+}-dependent processes, such as Ca^{2+} channel inactivation, Ca^{2+} channel enhancement, and the activation of both voltage-dependent and voltage-independent nonselective cation currents. In the network implementation, only membrane potential is coupled between neighboring neurons, while these second-messenger processes are intrinsic and isolated to each neuron.

Simulations on a two neuron network reproduced similar results to biological bag cell neurons grown in culture with some exceptions. The unstimulated, coupled neuron in the experiment exhibited variable amplitudes as it approached synchrony with the stimulated neuron, while the unstimulated *model* neuron exhibited all-or-nothing firing. Additionally, hyperpolarization of the model neuron (not shown) occurred with a much faster time constant in the model neuron than in the experimental neuron. These differences could be the result of model deficiencies excluding channels involved in the A-current, or the implementation of a single, effective potassium current. They could also stem from differing assumptions between the experimental context and the inherently isolated, theoretical

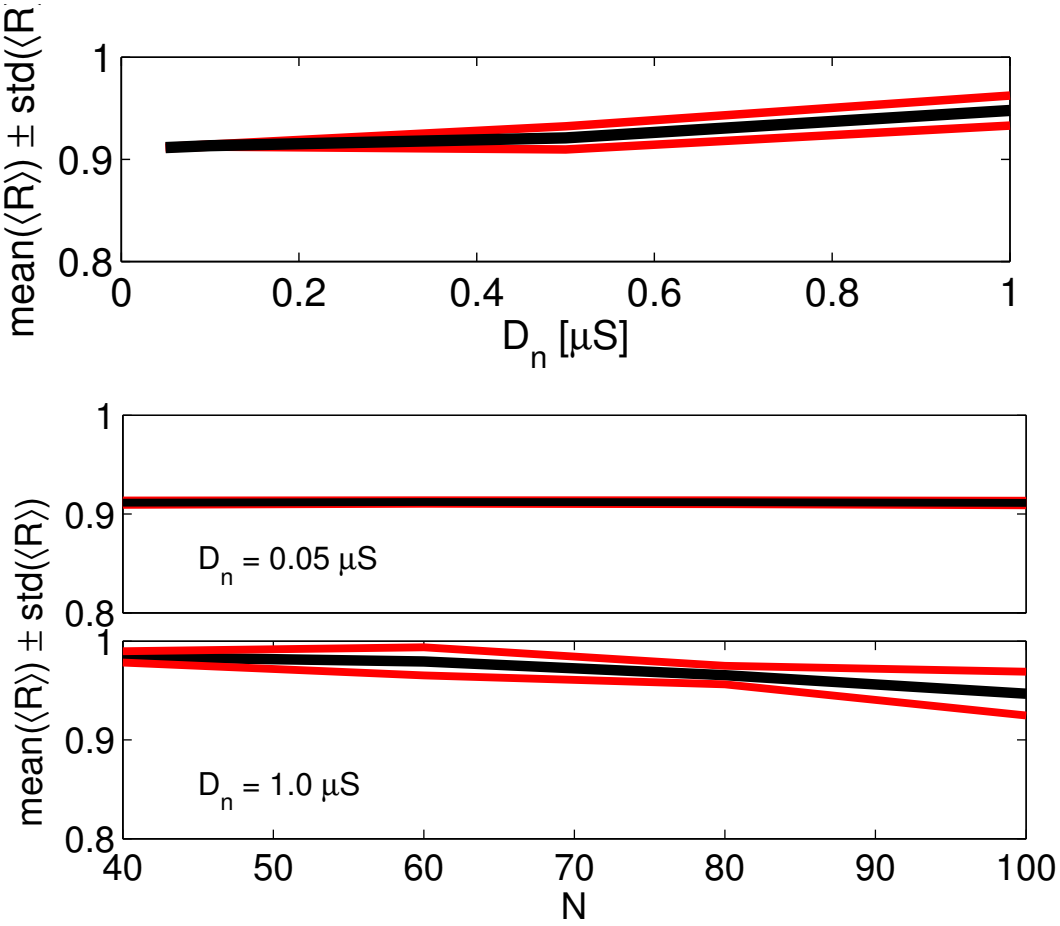

Figure 4.16: Top: Mean value of the phase coherence (black line) with standard deviation (red lines), taken from the last 20 s of a 120 s run across coupling strength, D_n for a 100-neuron network. Lower, the order parameter across changes in network size, N for weak coupling (middle axes) and strong coupling (bottom axes). Each point is average from $n = 10$ runs. The initial conditions and capacitance are randomly perturbed for each neuron in the network.

model neuron.

In the 100-neuron network, network excitability was determined by the propensity for a wave to spread from the stimulated neuron to its immediate neighbors, and for this process to continue until the whole network is saturated. This required a coupling constant strong enough that nearby neighbor were sufficiently excited, but also weak enough that the neighbors did not drain the stimulated neuron of its spiking capacity. With more connections per neuron, this effect became more pronounced, as evidenced by the results for the cluster ring network and the scatter network. Distances in the network become important for traveling waves. For instance, in the simple ring network, waves travel slowly as the ring network requires series transmission through the whole network, from one neuron to the next. If this distance is shortened, by additional connections (as in the cluster ring topology) or adding random shortcuts (as in the scatter topology), signals

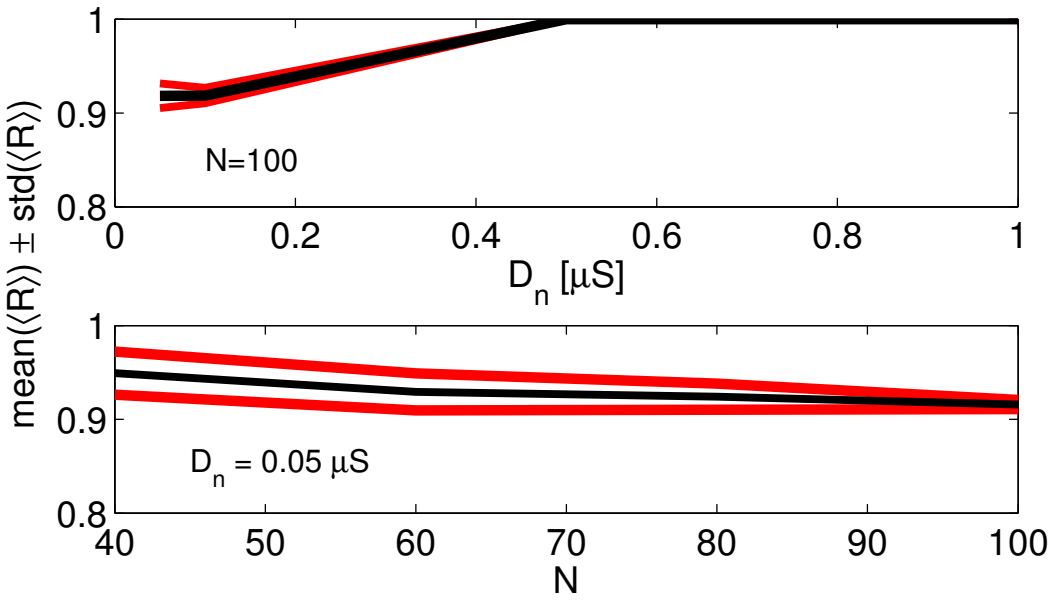

Figure 4.17: The mean of the time-average order parameter $\langle R \rangle$ (black line) and standard deviation (red) for a 100-neuron cluster ring network for varying D_n (top) and varying N (bottom). See Figure 4.16 for details.

propagate across the network much faster.

In the literature, there is only a limited picture of how excitation spreads through biological bag cell cluster. The *in silica* simulation experiments performed here bear some resemblance to experiments in the literature. Namely, experiments in which a single bag cell neuron in the pleural ganglion is excited and measurements in another region of the intact bag cell cluster were taken [10][11]. The author, Brown, proposes a "temporal spread of excitation" through the cluster, but doesn't give any explicit quantitative picture of the speed of that spread. An isolated two-neuron experiment in culture shows stimulation of a single neuron on an its electrically-coupled neighbor, in which propagation of action potentials from the stimulated cell to the unstimulated cell took approximately 1.5 s [30]. Yet another experiment, using an acetylcholine bath to initiate afterdischarge in an intact cluster, reported the onset of afterdischarge occurring roughly one minute after submersion in the bath [104], though this delay is likely due to diffusion of the acetylcholine into the cluster. Kuperfermann & Kandel reported fast and robust synchrony across the bag cell cluster [64]. Experimental collaborators have verified this through personal communication. Thus, it is highly probable that the scatter network model best represents the bag cell cluster.

Chapter 5

Conclusions

5.1 Prototype *Aplysia* bag cell and network models

Looking at an example of the time-series evolution of the membrane potential over time during an afterdischarge (Figure 5.1, top), there are three obvious ways such a behavior could arise in a dynamical system representing it. In the simplest case, the apparent transitions from a steady state to a limit cycle could imply a bistable system in which both of these attractors exist (Figure 5.1, left bottom). In this case, actions that transition the system from one attractor to another would be considered external to the system. Given the experimental evidence, initiation of the afterdischarge comes from another neural cell, external to the bag cell [104]. Therefore, in a model of a bag cell neuron, the perturbation that causes trajectories to leave the steady state and get captured in the limit cycle must be considered external. Thus, we must exclude the single attractor case (Figure 5.1, bottom right). Since the refractory period is presumed to be internal, what results is a system with a single steady state at the resting potential and a limit cycle *quasi-attractor* (Figure 5.1, bottom middle). The quasi-attractor captures trajectories for a finite period before they are pulled (or pushed) back to the steady state. In the case of the bag cell neuron, that finite period is the duration of the afterdischarge. However, the model developed in this thesis focuses on the onset of afterdischarge, and therefore does not include any intrinsic machinery to initiate a refractory period. As such, the model constructed here consists of two attractors, as in Figure 5.1, left bottom.

The biologically motivated construction of the *Aplysia* bag cell model relies heavily on calcium dependent mechanisms and could help to inform experimentalists of the quantitative details underlying calcium mechanisms within the bag cell. For instance, measurements derived from calcium *inactivation* experiments predict a much sharper inactivation than what is observed in the in-step inactivation phase of *activation* experiments. This can be explained by a combination of calcium-dependent and voltage-dependent inactivation (Figure 2.7). Because calcium concentration acts as a much slower variable in the system, the in-step inactivation, having a low pre-clamp voltage, is likely to have lower values of calcium. The inactivation experiment, typically involves pre-clamp values at high voltages, in which case calcium is entering the cell and may be affecting inactivation kine-

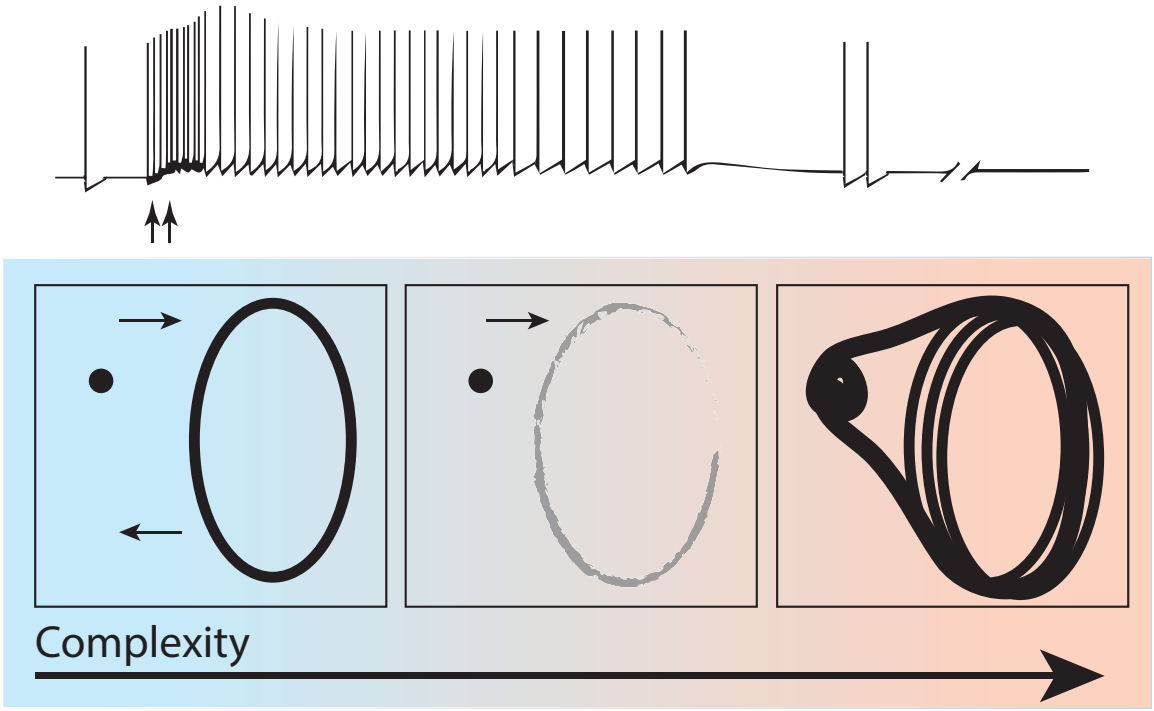

Figure 5.1: Various arrangements that could produce afterdischarge behavior. Left: a bistable system, middle: a single steady state and an attractor ruin, right: a strange attractor or complicated limit cycle. Afterdischarge trace (top) extracted from Scholarpedia [114].

tics. The quantitative details of this interplay aren't immediately available in the lab, but can be demonstrated (relatively) quickly via mathematical model. Through this calcium-dependence, the calcium channel constructed here displays use-dependence, as observed in biological bag cells [50]. Additionally, a calcium-dependent enhancement of the calcium current[31] was implemented (Equation 2.6). Complementing the calcium channels, the observed two-component potassium current was condensed into a single effective potassium channel (Figure 2.14) after several failed attempts at representing both currents in an accurate and robust way. This included parameter forcing and basic subtraction methods. Subtraction methods failed, likely because current experiments do not completely isolate the two channels. The parameter forcing method may have been more successful with a more careful approach to implementing initial conditions, which generated ambiguities in the present attempt. The necessity of parameter forcing becomes clear when carrying out two-phase fitting, in which ambiguities that arise in Phase I of fitting can be resolved, to a degree, by the expectations of Phase II fitting. In this regard, the fitting was quite successful (Figure 2.13, red). It was carrying the analysis through to a dynamical systems context (Figure 2.13, blue squares) where failure took place, due largely to oversight on the author's part. However, it appears that the single effective potassium channel is sufficient for a decent approximation of the spike waveform and generation of the afterdischarge. After extracting the kinetic parameters from experimental data, the conductances of the calcium, potassium, and leak channels (and any subsequent adjustments to use-dependence or potassium kinetics) were determined and optimized. Through both systematic trial and

error, using a self-coded GUI in Matlab (Figure 2.15) as well as optimization via genetic algorithm, model output was compared to experimental observations until spike shape, use-dependence behavior, and calcium activation reflected experimental results.

To elicit afterdischarge, the nonselective channels have been modeled for the first time, drawing on experimental data for their kinetics [69][50][70] and, using trial and error, determining appropriate conductances. The time constants were derived from a qualitative assessment of experimental data and basic intuition about the role time constants play, mathematically, in their associated current. Preliminary results showed that the nonselective channels were necessary for afterdischarge, as was the introduction of a delay term to nonselective channel response. The delay term may represent the time it takes for calmodulin binding and conformation to occur. Deeper modeling of this mechanism is likely required to enhance the model delay, as it currently is still a much shorter delay than observed in experiment. It's also possible that the nonselective channels draw from entirely different calcium pools than the microdomain near the calcium channels [69][44][37].

A preliminary analysis of the system using continuation curves provides a novel approach to constructing and tuning models. Comparing the continuation curves of a system as parameters are changed provides a quantitative measure of system sensitivity as well as qualitative insights into what aspects of system behavior particular parameters may be responsible for. For example, parameters associated with the time constant of potassium only modified the location of the Hopf point along the continuation curve (Figures 3.6 and 3.7), a change that maintained important properties like waveshape and afterdischarge, but tightened the range over which the applied current evoked spiking, better matching experimental observations.

To date, this is the only known network model of the electrically coupled bag cell cluster. The network propagates waves of excitation in a manner consistent with the observations of Brown [10] with a time delay that depends on positive feedback mechanisms. Brown experimentally highlighted the contribution of bag cell peptides to positive feedback, while the present study depends solely on calcium mechanisms. Long-range network propagation in the simple ring network clearly depended on intrinsic calcium mechanisms to activate nonselective channels, while short-range propagation enabled those calcium mechanisms to occur through low-frequency spiking (Figure 4.11). Not surprisingly, a stronger coupling strength and a higher number of connection per neuron, as demonstrated in the ring cluster and scatter networks, made this process occur much faster, but the phenomena can still be observed taking place over a shorter time scale (Figure 4.15).

A precursory analysis of phase coherence in the system observed along-side calcium levels suggest that most networks had reached a state of stable dynamics by 120 s with the exception of the weakly coupled ring (Figure 4.11 and statistical cases in which propagation never occurred due to a large coupling constant (Figure 4.17, $D_n > 0.5$ μS). It is plausible that the network has been captured by a stable limit cycle and spiking behavior will continue indefinitely in the current model. To address the refractory period, additional second-messenger modeling will probably be required.

5.1.1 Discussion and Outview

From a dynamical system perspective, the prototype *Aplysia* bag cell neuron contributes to persistence models; a class of neuron model distinct from the three traditional model types (excitable, oscillatory, and bursting cells). A similar persistence model describes a neural integrator proposed to underlie observations of persistence in neural populations in the prefrontal cortex during mammilian anticipation [34]. Similar to the present *Aplysia* model, it utilizes calcium-dependent modulation to generate positive feedback in the cell. Another integrator model relies on spatially extended calcium waves for persistence [68]. Both models include models of calcium dependent nonselective cation currents. A third author proposes an attractor with a dynamic fixed point for the attractor basin as the basis for the integrator [32]. This collection of papers offer some sophisticated tools in persistence modeling that may be of use to future modeling of persistence in the *Aplysia* bag cell model.

There are many issues with the present model that could be addressed. Splitting the effective potassium channel into the component pair typically observed in biological bag cells is likely to yield different observations, corresponding to an altered continuation curve, which may yield a more accurate waveform. The relative conductances of channels, particularly nonselective channels, is not derived from experimental data because of the sensitivity of channel conductance to experimental context. A more comprehensive approach to continuation analysis could help guide in tuning the *Aplysia* bag cell model deeper into biological relevance. For example, transforming the direction of the Hopf bifurcation might resolve discrepancies in the 2-neuron stimulation experiment (Figure 3.9). In Section 3, a parameter was revealed that shifted the location of the Hopf bifurcation, H3, along the continuation curve, without changing the curve itself. Flipping the limit cycle associated with H3 could require, first, shifting it towards I approaches 0, then trying to alter it's stability (or, possibly, the stability of Hopf points H1 and H2). It is still unclear what bifurcation underlies the transition from steady state (resting potential) to the limit cycle (tonic spiking), a feat which would require exploring the capability of various continuation software more deeply. Another analytical approach to tuning may lie in phase-plot analysis, touched on briefly as part of the development of the order parameter. Adjustments to parameters, followed by quantification of different projections in the system, will undoubtedly provide insight into underlying dynamics. For instance, the phase-planes involving the membrane potential (Figure 4.8) immediately tell us that the use-dependent inactivation, calcium concentration, and delay term (h, s, and r respectively) describe an evolution in state, while the other activation variables (m, n, q, and η) describe short term oscillatory dynamics. The kinetics of the voltage-independent cation channels (ϕ, θ) haven't yet responded to calcium, which is at insufficent levels for $t < 0.5$.

In the mathematical model, the afterdischarge elicited following the 5 Hz protocol happens a short time after cessation of the input (Figure 2.23), compared to typical experiments. This is likely because the calcium delay term associated with the voltage-independent nonselective cation channel is a direct time delay on microdomain calcium levels, which decay rather quickly in the absence of stimulus. The result was that the delay variable was just long enough to allow voltage-dependent channels to depolarize.

Extending the system with proper second-messenger dynamics may help sustain the cation's activation, θ, at low currents for a long enough time to account for the slow delay to the onset of afterdischarge. Alternatively, the previously mentioned integrator neuron model was able to produce a longer delay using a hyperpolarizing current [34]. Implementation of the refractory period could be relatively simple to implement, using a calcium-dependent activation function with a long time constant, but would require very long simulation times to test and verify, given the lengthy duration of afterdischarge. A more complicated and biologically relevant model could be derived from experimental evidence, which would require an implementation of PKC and/or the addition of the BK^+ current [71][72][116].

Experimental measurements of *Aplysia* bag cell's electrical junctions yield a conductance of 8-10 nS [29]. The simple ring network model exhibited "weak" coupling at 15 nS, while the ring cluster network model exhibited "strong" coupling at 15 nS. The scatter network exhibited "weak coupling" at $D_n = 7$ nS. Assuming that more connections in the network requires a smaller conductance value for similar behavior, the experimental result implies that the average number of connections per neuron should be more than four (as in the ring cluster topology). Finally, the network is lacking heterogeneity. It has previously been demonstrated that heterogeneity can be a necessary driver of system dynamics in systems. For example, taking averages can miss important regions of parameter space [74], heterogeneity can diminish effective negative feedback, enhancing network interactions [86], and heterogeneity raises the responsiveness of neural networks [66].

Network dynamics of the *Aplysia* bag cell neuron may be interesting in the context of spatiotemporal reaction-diffusion systems. Electrically coupled neurons are mathematically identical to discretized reaction-diffusion systems. The electrically-coupled Morris-Lecar network is similarly capable of wave propagation, and additionally exhibits transient spatiotemporal chaos [60]. It is possible that there is a physiologically relevant regime in which *Aplysia* bag cell clusters exhibit transient spatiotemproal chaos once a refractory period has been implemented. Experimentalists should look to evidence in the form of neurons intermittently exhibiting *spikelets* and full action potentials in intact clusters. The existence of such behavior might suggest such the interplay of complex dynamics [60]. Spikelets occur when electrically-coupled neurons don't elicit full action potentials, as has been observed in hippocampal neurons [101]. The spikelets are a result of draining from coupled neighbors and, as such, often require very fine tuning of the coupling constant, D_n. As is, the *Aplysia* bag cell model is unlikely to yield chaos, given the apparent stability of its oscillations and phase coherence. A more robust measure would require evaluating the Lyapunov exponent of the network [93].

In order to make the *Aplysia* bag cell network model more consistent with the biological *Aplysia* bag cell cluster, an experimental analysis of the bag cells cluster's connectome would be informative. As demonstrated here, topology can have an effect on what values of D_n are considered "strong" or "weak" coupling, and varying the longest distance in the network can reduce the time it takes for the network to synchronize. On the theoretical aside, a more systematic approach to construction of scatter networks or deriving a method to model the topology of a three dimensional, spherical cluster of neurons may yield more relevant results. For instance, rules that enforced a maximum number of connections per neuron (or equivalently, a maximum number of 1's per row in the matrix, A), and an

additional rule set that would confine the longest maximum and minimum distances in the network. This is not a trivial task, and I hereby declare it outside my scope. I suggest any hopeful graduate students reading this learn when to do the same when the time is appropriate. I leave you, now, with this quote, taken from an introductory text on statistical mechanics. And what are neurons to a geometrist besides particles of not 4, but 10 dimensions?

Ludwig Boltzmann, who spent much of his life studying statistical mechanics, died in 1906, by his own hand. Paul Ehrenfest, carrying on the work, died similarly in 1933. Now it is your turn to study statistical mechanics. Perhaps it will be wise to approach the subject cautiously...

-David Goodstein, *States of Matter* [39]

References

[1] L. Abbott and T. Kepler. Model neurons: from hodgkin-huxley to hopfield. In *Statistical mechanics of neural networks*, pages 5–18. Springer, 1990.

[2] A. Adamatzky. Universal dynamical computation in multidimensional excitable lattices. *International Journal of Theoretical Physics*, 37(12):3069–3108, 1998.

[3] W. Adams and J. Benson. The generation and modulation of endogenous rhythmicity in the *Aplysia* bursting pacemaker neurone R15. *Progress in Biophysics and Molecular Biology*, 46(1):1–49, 1985.

[4] W. Adams and I. Levitan. Voltage and ion dependences of the slow currents which mediate bursting in *Aplysia* neurone R15. *The Journal of Physiology*, 360(1):69–93, 1985.

[5] H. Alexopoulos, A. Böttger, S. Fischer, A. Levin, A. Wolf, T. Fujisawa, S. Hayakawa, T. Gojobori, J. Davies, C. David, et al. Evolution of gap junctions: the missing link? *Current biology*, 14(20):R879–R880, 2004.

[6] D. Bartsch, M. Ghirardi, P. Skehel, K. Karl, S. Herder, M. Chen, C. Bailey, and E. Kandel. *Aplysia* creb2 represses long-term facilitation: relief of repression converts transient facilitation into long-term functional and structural change. *Cell*, 83(6):979–992, 1995.

[7] H. Bellen, C. Tong, and H. Tsuda. 100 years of *Drosophila* research and its impact on vertebrate neuroscience: a history lesson for the future. *Nature Reviews Neuroscience*, (7):514–522, 2010.

[8] R. Bertram, M. Butte, T. Kiemel, and A. Sherman. Topological and phenomenological classification of bursting oscillations. *Bulletin of Mathematical Biology*, 57:413–439, 1995.

[9] A. Bragina, J. Csicsvari, M. Penttonen, and G. Buzsaki. Epileptic afterdischarge in the hippocampal-entorhinal system: current source density and unit studies. *Neuroscience*, 76(4):1187 – 1203, 1997.

[10] R. Brown and E. Mayeri. Positive feedback by autoexcitatory neuropeptides in neuroendocrine bag cells of aplysia. *Journal of Neuroscience*, 9(4):1443–1451, 1989.

[11] R. Brown, S. Pulst, and E. Mayeri. Neuroendocrine bag cells of aplysia are activated by bag cell peptide-containing neurons in the pleural ganglion. *Journal of neurophysiology*, 61(6):1142–1152, 1989.

[12] T Budde, S. Meuth, and HC Pape. Calcium-dependent inactivation of neuronal calcium channels. *Nature Reviews Neuroscience*, 3(11):873–883, 2002.

[13] J. Burbach and H. Peter. What are neuropeptides? In A. Merighi, editor, *Neuropeptides*, volume 789 of *Methods in Molecular Biology*, pages 1–36. Humana Press, 2011.

[14] Robert J Butera, John W Clark, Carmen C Canavier, Douglas A Baxter, and John H Byrne. Analysis of the effects of modulatory agents on a modeled bursting neuron: Dynamic interactions between voltage and calcium dependent systems. *Journal of computational neuroscience*, 2(1):19–44, 1995.

[15] C. Canavier, J. Clark, and J. Byrne. Simulation of the bursting activity of neuron r15 in aplysia: role of ionic currents, calcium balance, and modulatory transmitters. *Journal of Neurophysiology*, 66(6):2107–2124, 1991.

[16] CC Canavier, DA Baxter, JW Clark, and JH Byrne. Multiple modes of activity in a model neuron suggest a novel mechanism for the effects of neuromodulators. *Journal of neurophysiology*, 72(2):872–882, 1994.

[17] T. Carew, R. Hawkins, and E. Kandel. Differential classical conditioning of a defensive withdrawal reflex in *Aplysia californica*. *Science*, 219(4583):397–400, 1983.

[18] T. Carew, HM. Pinsker, and E. Kandel. Long-term habituation of a defensive withdrawal reflex in *Aplysia*. *Science*, 175(4020):451–454, 1972.

[19] A. Casadio, K. Martin, M. Giustetto, H. Zhu, M. Chen, D. Bartsch, C. Bailey, and E. Kandel. A transient, neuron-wide form of creb-mediated long-term facilitation can be stabilized at specific synapses by local protein synthesis. *Cell*, 99(2):221 – 237, 1999.

[20] Jean-Christophe Cassel. Chapter 3.9 - experimental studies on the role(s) of serotonin in learning and memory functions. In C. Miller and B. Jacobs, editors, *Handbook of the Behavioral Neurobiology of Serotonin*, volume 21 of *Handbook of Behavioral Neuroscience*, pages 429 – 447. Elsevier, 2010.

[21] J. Chad, R. Eckert, and D. Ewald. Kinetics of calcium-dependent inactivation of calcium current in voltage-clamped neurones of aplysia californica. *The Journal of physiology*, 347:279, 1984.

[22] J. Chad, R. Eckert, and D. Ewald. Kinetics of calcium-dependent inactivation of calcium current in voltage-clamped neurones of *Aplysia californica*. *The Journal of Physiology*, 347(1):279–300, 1984.

[23] B. Chance, A. Ghosh, and E. Pye. *Biological and biochemical oscillators*. Academic Press, 2014.

[24] S. Cheng, M. Willmann, HC Chen, and Jen. Sheen. Calcium signaling through protein kinases. the arabidopsis calcium-dependent protein kinase gene family. *Plant Physiology*, 129(2):469–485, 2002.

[25] A. Chiu, M. Hunkapiller, E. Heller, D. Stuart, L. Hood, and F. Strumwasser. Purification and primary structure of the neuropeptide egg-laying hormone of *Aplysia californica*. *Proceedings of the National Academy of Sciences*, 76(12):6656–6660, 1979.

[26] S. Cobb, E. Buhl, K. Halasy, O. Paulsen, and P. Somogyi. Synchronization of neuronal activity in hippocampus by individual gabaergic interneurons. *Nature*, 378(6552):75, 1995.

[27] W. Coetzee, Y. Amarillo, J. Chiu, A. Chow, D. Lau, T. McCormack, H. Morena, M. Nadal, A. Ozaita, D. Pountney, et al. Molecular diversity of k+ channels. *Annals of the New York Academy of Sciences*, 868(1):233–255, 1999.

[28] P. Conn and L. Kaczmarek. The bag cell neurons of *Aplysia*. *Molecular neurobiology*, 3(4):237–273, 1989.

[29] Z. Dargaei, P. Colmers, H. Hodgson, and N. Magoski. Electrical coupling between aplysia bag cell neurons: characterization and role in synchronous firing. *Journal of neurophysiology*, 112(11):2680–2696, 2014.

[30] Z. Dargaei, D. Standage, C. Groten, G. Blohm, and N. Magoski. Ca2+-induced uncoupling of aplysia bag cell neurons. *Journal of neurophysiology*, 113(3):808–821, 2015.

[31] S. DeRiemer, J. Strong, K. Albert, P. Greengard, and L. Kaczmarek. Enhancement of calcium current in aplysia neurones by phorbol ester and protein kinase c. *Nature*, 313(6000):313–316, 1985.

[32] J. Dudman and S. Siegelbaum. Making the grade with models of persistent activity. *Neuron*, 49(5):649–651, 2006.

[33] T. Dunn, D. Storm, and M. Feller. Calcium-dependent increases in protein kinase-a activity in mouse retinal ganglion cells are mediated by multiple adenylate cyclases. *PloS one*, 4(11):e7877, 2009.

[34] D. Durstewitz. Self-organizing neural integrator predicts interval times through climbing activity. *Journal of Neuroscience*, 23(12):5342–5353, 2003.

[35] L. Fink, J. Connor, and L. Kaczmarek. Inositol trisphosphate releases intracellularly stored calcium and modulates ion channels in molluscan neurons. *The Journal of Neuroscience*, 8(7):2544–2555, 1988.

[36] L. Fricker. Neuropeptides and other bioactive peptides: From discovery to function. *Colloquium Series on Neuropeptides*, 1(3):1–122, 2012.

[37] K. Gardam and N. Magoski. Regulation of cation channel voltage and Ca^{2+} dependence by multiple modulators. *Journal of Neurophysiology*, 102(1):259–271, 2009.

[38] W. C Gerken, L. Purvis, and R. Butera. Genetic algorithm for optimization and specification of a neuron model. *Neurocomputing*, 69(10):1039–1042, 2006.

[39] D. Goodstein. *States of matter*. Courier Corporation, 2014.

[40] S. Grewal, A. Horgan, R. York, G. Withers, G. Banker, and P. Stork. Neuronal calcium activates a Rap1 and B-Raf signaling pathway via the cyclic adenosine monophosphate-dependent protein kinase. *Journal of Biological Chemistry*, 275(5):3722–3728, 2000.

[41] J. Guo and H. Duff. Inactivation of ICa-L is the major determinant of use-dependent facilitation in rat cardiomyocytes. *The Journal of Physiology*, 547(3):797–805, 2003.

[42] N. Hatcher and J. Sweedler. *Aplysia* bag cells function as a distributed neurosecretory network. *Journal of neurophysiology*, 99(1):333–343, 2008.

[43] S. Hedges, J. Blair, M. Venturi, and J. Shoe. A molecular timescale of eukaryote evolution and the rise of complex multicellular life. *BMC Evolutionary Biology*, 4(1):2, 2004.

[44] C. Hickey, J. Geiger, C. Groten, and N. Magoski. Mitochondrial ca2+ activates a cation current in aplysia bag cell neurons. *Journal of neurophysiology*, 103(3):1543–1556, 2010.

[45] B. Hille et al. *Ion channels of excitable membranes*, volume 507. Sinauer Sunderland, MA, 2001.

[46] A. Hodgkin and A. Huxley. The components of membrane conductance in the giant axon of *Loligo*. *The Journal of physiology*, 116(4):473–496, 1952.

[47] A. Hodgkin and A. Huxley. Currents carried by sodium and potassium ions through the membrane of the giant axon of *Loligo*. *The Journal of physiology*, 116(4):449, 1952.

[48] A. Hodgkin and A. Huxley. A quantitative description of membrane current and its application to conduction and excitation in nerve. *The Journal of physiology*, 117(4):500, 1952.

[49] JY Hu, F. Wu, and S. Schacher. Two signaling pathways regulate the expression and secretion of a neuropeptide required for long-term facilitation in *Aplysia*. *The Journal of Neuroscience*, 26(3):1026–1035, 2006.

[50] A. Hung and N. Magoski. Activity-dependent initiation of a prolonged depolarization in aplysia bag cell neurons: role for a cation channel. *Journal of Neurophysiology*, 97(3):2465–2479, 2007.

[51] E. Izhikevich. *Dynamical systems in neuroscience*. MIT press, 2007.

[52] R. Jolivet, R. Kobayashi, A. Rauch, R. Naud, S. Shinomoto, and W. Gerstner. A benchmark test for a quantitative assessment of simple neuron models. *Journal of Neuroscience methods*, 169(2):417–424, 2008.

[53] R. Jolivet, F. Schürmann, T. Berger, R. Naud, W. Gerstner, and A. Roth. The quantitative single-neuron modeling competition. *Biological cybernetics*, 99(4):417–426, 2008.

[54] L. Kaczmarek, M. Finbow, J. Revel, and F. Strumwasser. The morphology and coupling of aplysia bag cells within the abdominal ganglion and in cell culture. *Journal of neurobiology*, 10(6):535–550, 1979.

[55] L. Kaczmarek, M. Finbow, J. Revel, and F. Strumwasser. The morphology and coupling of *Aplysia* bag cells within the abdominal ganglion and in cell culture. *Journal of Neurobiology*, 10(6):535–550, 1979.

[56] L. Kaczmarek, K. Jennings, and F. Strumwasser. Neurotransmitter modulation, phosphodiesterase inhibitor effects, and cyclic AMP correlates of afterdischarge in peptidergic neurites. *Proceedings of the National Academy of Sciences*, 75(10):5200–5204, 1978.

[57] L. Kaczmarek, K. Jennings, and F. Strumwasser. An early sodium and a late calcium phase in the afterdischarge of peptide-secreting neurons of *Aplysia*. *Brain research*, 238(1):105–115, 1982.

[58] L. Kaczmarek and F. Strumwasser. The expression of long lasting afterdischarge by isolated *Aplysia* bag cell neurons. *The Journal of Neuroscience*, 1(6):626–634, 1981.

[59] K. Kaneko and I. Tsuda. Chaotic itinerancy. *Chaos: An Interdisciplinary Journal of Nonlinear Science*, 13(3):926–936, 2003.

[60] K. Keplinger and R. Wackerbauer. Transient spatiotemporal chaos in the morris-lecar neuronal ring network. *Chaos: An Interdisciplinary Journal of Nonlinear Science*, 24(1):013126, 2014.

[61] C. Koch. *Biophysics of computation: information processing in single neurons*. Oxford university press, 2004.

[62] R. Kretsinger. Calcium coordination and the calmodulin fold: divergent versus convergent evolution. In *Cold Spring Harbor symposia on quantitative biology*, volume 52, pages 499–510. Cold Spring Harbor Laboratory Press, 1987.

[63] A. Kriegstein. Development of the nervous system of *Aplysia californica*. *Proceedings of the National Academy of Sciences*, 74(1):375–378, 1977.

[64] I. Kupfermann and E. Kandel. Electrophysiological properties and functional interconnections of two symmetrical neurosecretory clusters (bag cells) in abdominal ganglion of aplysia. *Journal of Neurophysiology*, 33(6):865–876, 1970.

[65] Y. Kuramoto. *Chemical oscillations, waves, and turbulence*, volume 19. Springer Science & Business Media, 2012.

[66] J. Lengler, F. Jug, and A. Steger. Reliable neuronal systems: the importance of heterogeneity. *PloS one*, 8(12):e80694, 2013.

[67] D. Lloyd. A mathematical model of the bag-cell neuron in *Aplysia* californica. Master's thesis, University of Waterloo, 2011.

[68] Y. Loewenstein and H. Sompolinsky. Temporal integration by calcium dynamics in a model neuron. *Nature neuroscience*, 6(9):961–967, 2003.

[69] D. Lupinsky and N. Magoski. Ca2+-dependent regulation of a non-selective cation channel from aplysia bag cell neurones. *The Journal of physiology*, 575(2):491–506, 2006.

[70] N. Magoski. Regulation of an *Aplysia* bag cell neuron cation channel by closely associated protein kinase a and a protein phosphatase. *The Journal of Neuroscience*, 24(30):6833–6841, 2004.

[71] N. Magoski. Regulation of an *Aplysia* bag cell neuron cation channel by closely associated protein kinase A and a protein phosphatase. *The Journal of Neuroscience*, 24(30):6833–6841, 2004.

[72] N. Magoski and L. Kaczmarek. Association/dissociation of a channel–kinase complex underlies state-dependent modulation. *Journal of Neuroscience*, 25(35):8037–8047, 2005.

[73] G. Major and D. Tank. Persistent neural activity: prevalence and mechanisms. *Current opinion in neurobiology*, 14(6):675–684, 2004.

[74] E. Marder and A. Taylor. Multiple models to capture the variability in biological neurons and networks. *Nature neuroscience*, 14(2):133–138, 2011.

[75] L. Martin, A. Casadio, H. Zhu, Y. E, J. Rose, M. Chen, C. Bailey, and E. Kandel. Synapse-specific, long-term facilitation of *Aplysia* sensory to motor synapses: A function for local protein synthesis in memory storage. *Cell*, 91(7):927 – 938, 1997.

[76] E. Mayeri and B. Rothman. Neuropeptides and the control of egg-laying behavior in *Aplysia*. In *Model neural networks and behavior*, pages 285–301. Springer, 1985.

[77] M. Mitchell. *An Introduction to Genetic Algorithms*. MIT press, 1998.

[78] L. Moroz, J. Edwards, S. Puthanveettil, A. Kohn, T. Ha, A. Heyland, B. Knudsen, A. Sahni, F. Yu, L. Liu, et al. Neuronal transcriptome of *Aplysia*: Neuronal compartments and circuitry. *Cell*, 127(7):1453–1467, 2006.

[79] C. Morris and H. Lecar. Voltage oscillations in the barnacle giant muscle fiber. *Biophysical Journal*, 35(1):193 – 213, 1981.

[80] M. Mourão, J. Hakim, and S. Schnell. Connecting the dots: the effects of macromolecular crowding on cell physiology. *Biophysical journal*, 107(12):2761–2766, 2014.

[81] R. Newcomb and R. Scheller. Regulated release of multiple peptides from the bag cell neurons of *Aplysia californica*. *Brain research*, 521(1):229–237, 1990.

[82] T. Nick, L. Kaczmarek, and T. Carew. Ionic currents underlying developmental regulation of repetitive firing in *Aplysia* bag cell neurons. *The Journal of Neuroscience*, 16(23):7583–7598, 1996.

[83] D. Pazó and E. Montbrió. Universal behavior in populations composed of excitable and self-oscillatory elements. *Physical Review E*, 73(5):055202, 2006.

[84] A. Pertsov, R. Aliev, and V. Krinsky. Three-dimensional twisted vortices in an excitable chemical medium. *Nature*, 345(6274):419, 1990.

[85] T. Perumal and R. Gunawan. Understanding dynamics using sensitivity analysis: caveat and solution. *BMC systems biology*, 5(1):41, 2011.

[86] T. Pfeil, J. Jordan, T. Tetzlaff, A. Grübl, J. Schemmel, M. Diesmann, and K. Meier. Effect of heterogeneity on decorrelation mechanisms in spiking neural networks: A neuromorphic-hardware study. *Physical Review X*, 6(2):021023, 2016.

[87] R. Plant and M. Kim. Mathematical description of a bursting pacemaker neuron by a modification of the Hodgkin-Huxley equations. *Biophysical Journal*, 16(3):227–244, 1976.

[88] F. Plaza, M. Velarde, F. Arecchi, S. Boccaletti, M. Ciofini, and R. Meucci. Excitability following an avalanche-collapse process. *EPL (Europhysics Letters)*, 38(2):85, 1997.

[89] E. Quattrocki, J. Marshall, and L. Kaczmarek. A shab potassium channel contributes to action potential broadening in peptidergic neurons. *Neuron*, 12(1):73–86, 1994.

[90] T. Ree Chay and D. Cook. Endogenous bursting patterns in excitable cells. *Mathematical Biosciences*, 90(1):139–153, 1988.

[91] C. Rossant, D. Goodman, B. Fontaine, J. Platkiewicz, A. Magnusson, and R. Brette. Fitting neuron models to spike trains. *Frontiers in neuroscience*, 5:9, 2011.

[92] J. Russell, G. Leng, and A. Douglas. The magnocellular oxytocin system, the fount of maternity: adaptations in pregnancy. *Frontiers in neuroendocrinology*, 24(1):27–61, 2003.

[93] S. Sato, M. Sano, and Y. Sawada. Practical methods of measuring the generalized dimension and the largest lyapunov exponent in high dimensional chaotic systems. *Progress of Theoretical Physics*, 77(1):1–5, 1987.

[94] R. Scheller, J. Jackson, L. McAllister, B. Rothman, E. Mayeri, and R. Axel. A single gene encodes multiple neuropeptides mediating a stereotyped behavior. *Cell*, 32(1):7–22, 1983.

[95] W. Singer. Neuronal synchrony: a versatile code for the definition of relations? *Neuron*, 24(1):49–65, 1999.

[96] P. Steinmetz, A. Roy, P. Fitzgerald, S. Hsiao, K. Johnson, and E. Niebur. Attention modulates synchronized neuronal firing in primate somatosensory cortex. *Nature*, 404(6774):187–190, 2000.

[97] J. Strong. Modulation of potassium current kinetics in bag cell neurons of *Aplysia* by an activator of adenylate cyclase. *The Journal of Neuroscience*, 4(11):2772–2783, 1984.

[98] J. Strong and L. Kaczmarek. Multiple components of delayed potassium current in peptidergic neurons of *Aplysia*: modulation by an activator of adenylate cyclase. *The Journal of Neuroscience*, 6(3):814–822, 1986.

[99] A. Tam, J. Geiger, A. Hung, C.J Groten, and N. Magoski. Persistent Ca^{2+} current contributes to a prolonged depolarization in *Aplysia* bag cell neurons. *Journal of neurophysiology*, 102(6):3753–3765, 2009.

[100] F. Varela, JP Lachaux, E. Rodriguez, and J. Martinerie. The brainweb: phase synchronization and large-scale integration. *Nature reviews neuroscience*, 2(4):229–239, 2001.

[101] E. Vigmond and B. Bardakjian. Spikelets and electrical coupling in hippocampal neurons. In *Engineering in Medicine and Biology Society, 1996. Bridging Disciplines for Biomedicine. Proceedings of the 18th Annual International Conference of the IEEE*, volume 4, pages 1566–1567. IEEE, 1996.

[102] N. Wayne, Y. Kim, and R. Yong-Montenegro. Seasonal fluctuations in the secretory response of neuroendocrine cells of *Aplysia californica* to inhibitors of protein kinase a and protein kinase c. *General and comparative endocrinology*, 109(3):356–365, 1998.

[103] B. White and L. Kaczmarek. Identification of a vesicular pool of calcium channels in the bag cell neurons of *Aplysia californica*. *The Journal of Neuroscience*, 17(5):1582–1595, 1997.

[104] S. White and N. Magoski. Acetylcholine-evoked afterdischarge in *Aplysia* bag cell neurons. *Journal of Neurophysiology*, 107(10):2672–2685, 2012.

[105] A. Willms, D. Baro, R. Harris-Warrick, and J. Guckenheimer. An improved parameter estimation method for Hodgkin-Huxley models. *Journal of Computational Neuroscience*, 6(2):145–168, 1999.

[106] G. Wilson and L. Kaczmarek. Mode-switching of a voltage-gated cation channel is mediated by a protein kinase A-regulated tyrosine phosphatase. *Nature*, 366:433–438, dec 1993.

[107] G. Wilson, F. Richardson, T. Fisher, B. Olivera, and L. Kaczmarek. Identification and characterization of a Ca^{2+}-sensitive nonspecific cation channel underlying prolonged repetitive firing in *Aplysia* neurons. *The Journal of Neuroscience*, 16(11):3661–3671, 1996.

[108] T. Womelsdorf, JM Schoffelen, R. Oostenveld, W. Singer, R. Desimone, A. Engel, and P. Fries. Modulation of neuronal interactions through neuronal synchronization. *science*, 316(5831):1609–1612, 2007.

[109] W. Yamada, C. Koch, and P. Adams. Multiple channels and calcium dynamics. *Methods in Neuronal Modeling: From synapses to networks*, pages 97–133, 1989.

[110] X. Yu, J. Byrne, and D. Baxter. Modeling interactions between electrical activity and second-messenger cascades in aplysia neuron r15. *Journal of neurophysiology*, 91(5):2297–2311, 2004.

[111] Y. Zhang and O. Hamill. On the discrepancy between whole-cell and membrane patch mechanosensitivity in xenopus oocytes. *The Journal of Physiology*, 523(1):101–115, 2000.

[112] Y. Zhang, J. Helm, A. Senatore, J. Spafford, L. Kaczmarek, and E. Jonas. Pkc-induced intracellular trafficking of cav2 precedes its rapid recruitment to the plasma membrane. *The Journal of Neuroscience*, 28(10):2601–2612, 2008.

[113] Y. Zhang, W. Joiner, A. Bhattacharjee, F. Rassendren, N. Magoski, and L.K Kaczmarek. The appearance of a protein kinase A-regulated splice isoform of slo is associated with the maturation of neurons that control reproductive behavior. *Journal of Biological Chemistry*, 279(50):52324–52330, 2004.

[114] Y. Zhang and L. Kaczmarek. Bag cell neurons. *Scholarpedia*, 3(7):4095, 2008.

[115] Y. Zhang, N. Magoski, and L. Kaczmarek. Prolonged activation of Ca^{2+}-activated K+ current contributes to the long-lasting refractory period of *Aplysia* bag cell neurons. *The Journal of Neuroscience*, 22(23):10134–10141, 2002.

[116] Y. Zhang, N. Magoski, and L. Kaczmarek. Prolonged activation of ca2+-activated k+ current contributes to the long-lasting refractory period ofaplysia bag cell neurons. *Journal of Neuroscience*, 22(23):10134–10141, 2002.

[117] Y. Zhang, S. McKay, B. Bewley, and L. Kaczmarek. Repetitive firing triggers clustering of kv2. 1 potassium channels in aplysia neurons. *Journal of Biological Chemistry*, 283(16):10632–10641, 2008.

[118] E. Zuckerkandl and L. Pauling. Evolutionary divergence and convergence in proteins. *Evolving genes and proteins*, 97:97–166, 1965.

APPENDICES

Appendix A

Full Model and Parameters

A.1 Model

$$\frac{dV}{dt} = \frac{1}{C}\left[I - I_{Ca} - I_K - I_{CATvi} - I_{CATvd} - I_L\right] \tag{A.1}$$

$$\frac{dm}{dt} = \frac{m_{ss}(V) - m}{\tau_m(V)} \tag{A.2}$$

$$\frac{dh}{dt} = \frac{h_{ss}(V) - h}{\tau_h(V)} \tag{A.3}$$

$$\frac{ds}{dt} = \frac{(1 - P_b)(I_{Ca} + I_{CATvi} + I_{CATvd})}{-2Fv} - D(s - s_0) \tag{A.4}$$

$$\frac{dn}{dt} = \frac{n_{ss}(V) - n}{\tau_n(V)} \tag{A.5}$$

$$\frac{dq}{dt} = \frac{q_{ss}(V) - q}{\tau_q(V)} \tag{A.6}$$

$$\frac{dr}{dt} = \frac{s - r}{\tau_r} \tag{A.7}$$

$$\frac{d\phi}{dt} = \frac{\phi_{ss}(r) - \phi}{\tau_\phi} \tag{A.8}$$

$$\frac{d\theta}{dt} = \frac{\theta_{ss}(r) - \theta}{\tau_\theta} \tag{A.9}$$

$$\frac{d\eta}{dt} = \frac{\eta_{ss}(r) - \eta}{\tau_\eta}, \tag{A.10}$$

where

$$I_{Ca} = \frac{\bar{G}_{Ca} m h (V - V_{Ca})}{1 + Ks} \tag{A.11}$$

$$I_K = \bar{g}_K n^4 q (V - V_K) \tag{A.12}$$

$$I_{CATvi} = \bar{g}_{CATvi} \phi \theta (V - V_{CATvi}) \tag{A.13}$$

$$I_{CATvd} = \bar{g}_{CATvd} \eta (V - V_{CATvd}) \tag{A.14}$$

$$I_L = g_L (V - V_L) \tag{A.15}$$

$$G = g_{Ca} \left(1 + M \frac{1}{2} (1 + \tanh \frac{r - Ca_1}{Ca_2}) \right) \tag{A.16}$$

$$P_b = \frac{B_t}{B_t + kA} \tag{A.17}$$

$$Bt = \frac{kAB_{tot}}{s + kA}, \tag{A.18}$$

and

$$m = \frac{1}{2} \left(1 + \tanh \frac{V - V_1}{V_2} \right) \tag{A.19}$$

$$\tau_m = \tau_{m0} \frac{1}{2} \left(1 + \tanh \frac{V - V_3}{V_4} \right) \tag{A.20}$$

$$h = \frac{1}{2} \left(1 + \tanh \frac{V - V_5}{V_6} \right) \tag{A.21}$$

$$\tau_h = \tau_{h0} \frac{1}{2} \left(1 + \tanh \frac{V - V_7}{V_8} \right) \tag{A.22}$$

$$n = \frac{1}{2} \left(1 + \tanh \frac{V - V_9}{V_{10}} \right) \tag{A.23}$$

$$\tau_n = \tau_{n0} \frac{1}{2} \left(1 + \tanh \frac{V - V_{11}}{V_{12}} \right) \tag{A.24}$$

$$q = \frac{1}{2} \left(1 + \tanh \frac{V - V_{13}}{V_{14}} \right) \tag{A.25}$$

$$\tau_q = \tau_{q0} \tag{A.26}$$

$$\theta_{ss} = \frac{1}{2} \left(1 + \tanh \frac{r - Ca_3}{Ca_4} \right) \tag{A.27}$$

$$\tau_\theta = \tau_{\theta 0} \tag{A.28}$$

$$\phi_{ss} = \frac{1}{2} \left(1 + \tanh \frac{r - Ca_5}{Ca_6} \right) \tag{A.29}$$

$$\tau_\phi = \tau_{\phi 0} \tag{A.30}$$

$$\eta_{ss} = \frac{1}{2}\left(1 + \tanh\frac{V - V_{15}(r)}{V_{16}(r)}\right) \tag{A.31}$$

$$V_{15} = V_{i1} + V_{i2}\frac{1}{2}\left(1 + \tanh\frac{r - Ca_7}{Ca_8}\right) \tag{A.32}$$

$$V_{16} = V_{j1} + V_{j2}\frac{1}{2}\left(1 + \tanh\frac{r - Ca_9}{Ca_{10}}\right) \tag{A.33}$$

$$\tau_\eta = \tau_{m0} \tag{A.34}$$

A.2 Parameters

Parameter		**Global Values**	Eq.
Capacitance	C [pF]	1360	A.1
Ca^{2+} conductance	$\bar{g}_{Ca}$ [μS]	93.5	A.16
K^{+} conductance	$\bar{g}_{k}$ [μS]	31.9	A.12
V-independent conductance	$\bar{g}_{CATvi}$ [μS]	0.05	A.13
V-dependent conductance	$\bar{g}_{CATvd}$ [μS]	0.2	A.14
Leak conductance	$\bar{g}_{L}$ [μS]	4.04e-02	A.15
Parameter		**Reversal Potentials**	Eq.
Ca reversal	V_{Ca} [mV]	60	A.11
K reversal	V_{K} [mV]	-80	A.12
V-independent reversal	V_{CATvi} [mV]	-45	A.13
V-dependent reversal	V_{CATvd} [mV]	10	A.14
Leak reversal	V_{L} [mV]	-60	A.15
Variable		**Initial Conditions**	Eq.
membrane potential	V_i [mV]	-54.8	N/A
Ca activation	m_i	1.00e-03	N/A
Ca inactivation	h_i	0.86	N/A
Ca concentration	s_i [M]	7.14e-02	N/A
K activation	n_i	6.07e-02	N/A
K inactivation	q_i	1.0	N/A
Ca delay	r_i [M]	7.14e-02	N/A
V-dependent activation	ϕ_i	0.0	N/A
V-dependent inactivation	θ_i	1.0	N/A
V-independent activation	η_i	3.70e-03	N/A

Table A.1: Initial Conditions, Global Values, and channel Reversal Potentials for the *Aplysia* bag cell model

Parameter		**Ca activation**	Eq.
activation shift	V_1 [mV]	-5.0	A.19
activation slope	V_2 [mV]	14.4	A.19
time constant shift	V_3 [mV]	-40.	A.20
time constant slope	V_4 [mV]	9.25	A.20
time constant max	τ_{m0} [s]	6.60e-03	A.20
Parameter		**Ca inactivation**	Eq.
inactivation shift	V_5 [mV]	-18	A.21
inactivation slope	V_6 [mV]	40	A.21
time constant shift	V_7 [mV]	-55	A.22
time constant slope	V_8 [mV]	15	A.22
time constant max	τ_{h0} [s]	1.5	A.22
Parameter		**Use Dependence**	Eq.
Ca diffusion	D [s^{-1}]	6.50	A.4
volume of microdomain	v [μM^3]	1.70e-05	A.4
Faraday's constant	F [C/M]	9.65e+04	A.4
internal calcium concentration	s_0 [M]	0.07	A.4
rate constant ratio	K [M^{-1}]	2.00e+03	A.11
buffering rate constant ratio	kA [M]	1.00e-04	A.17-18
Concentration of buffer	B_{tot} [M]	1.00e-04	A.18
Parameter		**Calcium Enhancement**	Eq.
enhancement shift	Ca_1 [M]	0.07	A.16
enhancement slope	Ca_2 [M]	0.01	A.16
enhancement multiplier	M	3.0	A.16

Table A.2: Calcium kinetics. Parameters V_1 and V_2 are the shift and slope of the activation function, V_3 and V_4 are the shift and slope of the time constant function, and τ_{n0} is the time constant maximum. Parameters V_9 through V_{12} and τ_{h0} are analogous for the inactivaiton.

Parameter		**K activation**	Eq.
activation shift	$V_9[mV]$	0	A.23
activation slope	V_{10} [mV]	40	A.23
time constant shift	V_{11} [mV]	-5	A.24
time constant slope	V_{12} [mV]	35.4	A.24
time constant max	τ_{n0} [s]	1.8e-02	A.24
Parameter		**K inactivation**	Eq.
inactivation shift	V_{13} [mV]	0	A.25
inactivation slope	V_{14} [mV]	10	A.25
inactivation time constant	τ_q [s]	0.1	A.25

Table A.3: Potassium kinetics

Parameters		**Voltage-independent**	Eq.
Ca delay constant	τ_r [s]	5.0	A.7
shift modulation shift	Ca_3 [M]	0.08	A.27
shift modulation slope	Ca_4 [M]	1.00e-04	A.27
activation time constant	τ_θ [s]	20	A.28
slope modulation shift	Ca_5 [M]	0.1	A.29
slope modulation slope	Ca_6 [M]	1.00e-03	A.29
inactivation time constant	τ_ϕ [s]	120	A.30
Parameters		**Voltage-dependent**	Eq.
V_{15} lower bound	V_{i1} [mV]	80	A.32
V_{15} additive	V_{i2} [mV]	44.8	A.32
V_{16} lower bound	V_{j1} [mV]	51	A.33
V_{16} additive	V_{j2} [mV]	28	A.33
enhancement shift	Ca_7 [M]	0.21	A.32
enhancement slope	Ca_8 [M]	0.5	A.32
enhancement shift	Ca_9 [M]	0.09	A.33
enhancement slope	Ca_{10} [M]	1.80e-02	A.33
time constant max	τ_{m0} [s]	6.60e-03	A.34

Table A.4: Nonselective cation channel kinetics